

**MODELING, CONFIGURATION AND CONTROL OPTIMIZATION OF
POWER-SPLIT HYBRID VEHICLES**

by

Jinming Liu

A dissertation submitted in partial fulfillment
of the requirements for the degree of
Doctor of Philosophy
(Mechanical Engineering)
in The University of Michigan
2007

Doctoral Committee:

Professor Huei Peng, Chair
Professor Jeffery L. Stein
Professor A. Galip Ulsoy
Associate Professor Jing Sun

© Jinming Liu 2007
All Rights Reserved

ACKNOWLEDGMENTS

I would like to express my earnest gratitude to my advisor, Professor Huei Peng. His guidance, assistance, patience, and encouragement have been of enormous importance to my research and the completion of the dissertation. I would also like to thank my other committee members, Professor Jeffery Stein, Professor Galip Ulsoy, and Professor Jing Sun, for their helpful advice and comments.

I am indebted to the Automotive Research Center at the University of Michigan for the financial support for my graduate study. Especially thank Professor Zoran Filipi and Doctor Hosam Fathy for their helps from the research center.

It has been a great pleasure working in the Vehicle Dynamics Lab as a doctoral student. Many thanks to my fellow graduate students for their help, discussion, and all the good times we have had in the office: Chen-Chiao Lin, Kangwon (Wayne) Lee, Hyungpil Moon, Daekyun Kim, Minjoong Kim, Jing Zhou, Ashish Deshpande, Konstantinos Varsos, Yi-Hsuan Hung, Yong-Song Chen, Cheng-Huei Han, Youseok Kou, Jeong-Seok Kim, Dongsuk Kum, Sehyun Chang, Sean Yang, Satyanarayanan Raghavan, Chiao-Ting Li, Dongsoo Kang, Youngjae Kim, and Jonathan Hagen.

Finally, my deepest thanks to my parents for all the love and support they have given me. I would also like to thank my fiancée, Qiang Li, for her encouragement and companionship during these years.

TABLE OF CONTENTS

ACKNOWLEDGMENTS	ii
LIST OF FIGURES	v
LIST OF TABLES	ix
LIST OF APPENDICES	x
CHAPTER 1	1
INTRODUCTION.....	1
1.1. Motivation.....	1
1.2. Background.....	4
1.3. Literature Review.....	15
1.4. Contributions.....	23
1.5. Outline of the Dissertation.....	25
CHAPTER 2.....	26
DYNAMIC MODELING OF POWER-SPLIT HYBRID VEHICLES.....	26
2.1. Overall Architecture.....	27
2.2. Sub-Systems/Components Modeling.....	28
2.3. The Powertrain Modeling.....	37
2.4. Validation of the Powertrain Dynamic Model.....	48
CHAPTER 3.....	52
AUTOMATED MODELING OF POWER-SPLIT HYBRID VEHICLES.....	52
3.1. The Universal Format of the Model Matrix.....	53
3.2. Automated Modeling Process.....	56
3.3. Automated Modeling Demonstration.....	58
CHAPTER 4.....	70
CONFIGURATION SCREENING OF POWER-SPLIT HYBRID VEHICLES.....	70
4.1. Physically Feasible Powertrain Configuration.....	72
4.2. Drivability and Power Source Component Sizing.....	77
4.3. Mode Shifting and ECVT Efficiency.....	82
CHAPTER 5.....	87

COMBINED CONFIGURATION DESIGN, COMPONENT SIZING, AND CONTROL OPTIMIZATION OF THE POWER-SPLIT HYBRID VEHICLES.....	87
5.1. Dynamic Program	88
5.2. Configuration Optimization	96
CHAPTER 6.....	104
IMPLEMENTABLE OPTIMAL CONTROL DESIGN OF THE POWER-SPLIT HYBRID VEHICLES.....	104
6.1. Power-Split and Engine Optimization	105
6.2. SDP for Power-Split Hybrid Vehicles	109
6.3. ECMS for Power-Split Hybrid Vehicles.....	115
6.4. Result and Discussion	120
CHAPTER 7.....	125
CONCLUSION AND FUTURE WORK.....	125
7.1. Conclusion	125
7.2. Future Work.....	127
APPENDICES.....	129
BIBLIOGRAPHY.....	153

LIST OF FIGURES

Figure 1.1: World crude oil price have increased over 400% since 1998 (DOE, 2007)	3
Figure 1.2: United States petroleum production and consumption (ORNL, 2006).....	3
Figure 1.3: EPA NO _x and particular matter regulation trends (DieselNet, 2007).	4
Figure 1.4: Parallel HEV configuration.	8
Figure 1.5: BSFC fuel map for a Saturn 1.9L (95 kW) DOHC SI engine.....	9
Figure 1.6: Series HEV configuration.	10
Figure 1.7: Power-split HEV configuration.....	12
Figure 1.8: Powertrain configuration of a single-mode hybrid system.	14
Figure 1.9: Powertrain configuration of a dual-mode hybrid system.	15
Figure 1.10: Hierarchical control architecture of a power-split hybrid electric vehicle... ..	20
Figure 1.11: Combined configuration design and control optimization procedure.....	25
Figure 2.1: The overall architecture of a power-split HEV in Matlab/Simulink.....	28
Figure 2.2: Composition of the planetary gear set.....	29
Figure 2.3: Force analysis on a planetary gear set.....	30
Figure 2.4: Planetary gear set and lever diagram.....	31
Figure 2.5: THS engine look-up table.....	32
Figure 2.6: THS engine BSFC map.....	32
Figure 2.7: Efficiency map of the MG 1 (15 kW).	34
Figure 2.8: Efficiency map of the MG 2 (35 kW).	34
Figure 2.9: Internal R battery model.....	35
Figure 2.10: THS battery lookup tables (R and V_{oc} against SOC).....	36
Figure 2.11: Driver Simulink model.....	37
Figure 2.12: Free body diagram of the THS powertrain.....	38
Figure 2.13: Free body diagram of the dual-mode powertrain.	41

Figure 2.14: The synchronized mode shifting of the dual-mode power-split powertrain (The engine speed is assumed constant)	46
Figure 2.15: Simulink model for a dual-mode power-split powertrain.	47
Figure 2.16: Power distribution of the Toyota Hybrid System (Hermance, 1999).....	49
Figure 2.17: THS Engine simulation results compared with published experiment results (Duoba et al., 2001) under the same driving cycle.	50
Figure 2.18: AHS powertrain simulation results (a) compared with published patent results (b) (Holmes et al., 2003).....	51
Figure 3.1: The powertrain of a double planetary gear system.....	59
Figure 3.2: GUI for the model rapid generation, which shows speeds of the engine and electric machines as functions of vehicle speed.	61
Figure 3.3: The powertrain of the triple planetary gear system in (Schmidt, 1999).....	63
Figure 3.4: Composition of the compound planetary gear set.	66
Figure 3.5: The powertrain of the compound PG system in (Hermance and Abe, 2006). 68	
Figure 4.1: The powertrain configuration identified by the example D matrix in (4.1) ..	73
Figure 4.2: An unfeasible configuration that has the engine connected to the vehicle shaft.	76
Figure 4.3: Torque values for a 30 kW MG2 in the THS configuration.	79
Figure 4.4: Torque values for a 90 kW MG2 in the THS configuration.	80
Figure 4.5: Torque values for a 30 kW MG2 in the 2-PG AHS configuration.....	80
Figure 4.6: Vehicle launching at constant power (100 kW).	82
Figure 4.7: Two possible dual-mode systems correspond to (4.13) and (4.14): (a) represented by matrix D and D_{mode21} ; (b) represented by matrix D and D_{mode22}	85
Figure 5.1: Formulation of the DP problem on a power-split system.	92
Figure 5.2: Example vehicle control performance results by DDP.	94
Figure 5.3: SOC under the same driving-cycle with different initial values.	98
Figure 5.4: Relationship between fuel consumption and change in battery SOC.	98
Figure 5.5: Electric power circulation under a launching maneuver (PT2, MG1=20kW and MG2=40kW).	99
Figure 5.6: Fuel economy contour plot for DDP results with different gear sizing (PT2, MG1=20kW and MG2=40kW).	101

Figure 5.7: MG2 efficiencies of two different design cases (High fuel efficiency case: $K_1=1.6$ and $K_2=2.2$, and low fuel efficiency case: $K_1=1.6$ and $K_2=1.6$).....	101
Figure 5.8: MG2 speeds and torques of two different design cases (High fuel efficiency case: $K_1=1.6$ and $K_2=2.2$, and low fuel efficiency case: $K_1=1.6$ and $K_2=1.6$).....	102
Figure 5.9: Vehicle speeds and battery SOC of two different design cases (High fuel efficiency case: $K_1=1.6$ and $K_2=2.2$, and low fuel efficiency case: $K_1=1.6$ and $K_2=1.6$).....	102
Figure 5.10: In the PT2 configuration, increasing K_2 results in higher speed of MG2 at the same vehicle speed.....	103
Figure 5.11: Potential fuel economy comparison between different configurations.....	103
Figure 6.1: Two-step control of the power-split powertrain showing system optimization and engine optimization.....	107
Figure 6.2: Feed-forward and feed-back controller for the MG1 torque control.....	108
Figure 6.3: The stochastic dynamic programming design process on a parallel hybrid vehicle.....	109
Figure 6.4: The stochastic dynamic programming design process on a power-split hybrid vehicle.....	110
Figure 6.5: Example of power demand probability map.....	111
Figure 6.6: Example of optimized engine power map from SDP.....	113
Figure 6.7: Calculated driving power (a) and vehicle speed (b) in the Markov chain model.....	114
Figure 6.8: SOC weighting factor $f(soc)$ for the ECMS algorithm (Paganali et al. 2002).	117
Figure 6.9: Speed constraint calculation in THS.....	117
Figure 6.10: Optimal solution searching process for the ECMS algorithm.....	119
Figure 6.11: Example optimized engine power map from ECMS.....	120
Figure 6.12: The engine operating point densities for both SDP and ECMS approaches in FTP75 cycle. (Sampling: 1Hz).	122
Figure 6.13: Engine power by DDP, SDP and ECMS algorithms during a vehicle launch.	124
Figure B.1: General power-split ECVT lever diagram.....	133

Figure B.2: Relative speed, torque, and power of the MG1 in input-split system.....	136
Figure B.3: Relative speed, torque, and power of the MG2 in input-split system.....	136
Figure B.4: Relative speed, torque, and power of the MG1 in compound-split system.	138
Figure B.5: Relative speed, torque, and power of the MG2 in compound-split system.	138
Figure D.1: Engine-in-the-loop setup for studies of the parallel hybrid electric propulsion.	146
Figure D.2: The beginning part of the FTP75 reference driving schedule compared with simulation and experiment results.	147
Figure D.3: Comparison of engine throttle commands between (a) the initial control design and (b) the refined control design (right).	149
Figure D.4: Comparison of (a) engine speed and (b) engine torque results between simulation and experiment with an initial control design.	149
Figure D.5: Comparison of control maps between (a) the initial control design and (b) the refined control design (right).	150
Figure D.6: Comparison of (a) engine speed and (b) engine torque results between simulation and experiment with a more accurate and smoother control design.	150
Figure D.7: Comparison of transient soot concentration profiles during a 185s-205 sec interval of the FTP75 driving schedule. Refined SDP power management strategy (light blue) eliminates the transient spikes of soot emission seen with the initial strategy (dark red).	152
Figure D.8: Final fuel economy and soot emission comparison between the conventional vehicle and different control designs.	152

LIST OF TABLES

Table 1.1: Hybrid electric vehicles on the horizon (Fueleconomy.gov, 2007).....	6
Table 2.1: Rule-based THS powertrain control strategy.	49
Table 3.1: Matrix D for the popular power-split powertrain designs.	69
Table 4.1: Specifications for the super-size power-split hybrid HMMWV.....	72
Table 4.2: Comparison of attributes and cost of three type of traction motors (Cuenca et al., 1999).	78
Table 5.1: States and inputs in different types of vehicles (Assume the objective is to analyze the control of the powertrain power flow at the system level)	91
Table 5.2: The selected grid points in DDP.....	92
Table 5.3: Vectorization approach effect on simulation time.....	96
Table 6.1: Fuel economy comparison between different control algorithms.	121
Table C.1: DDP results for different gear dimensions and MG sizing on PT1.	141
Table C.2: DDP results for different gear dimensions and MG sizing on PT2.	142

LIST OF APPENDICES

Appendix A: NOMENCLATURE.....	130
Appendix B: POWER-SPLIT SYSTEM EFFICIENCY ANALYSIS	132
Appendix C: DESIGN EVALUATION RESULTS.....	141
Appendix D: ENGINE-IN-THE-LOOP STUDY ON MAP ACCURACY EFFECT OF SDP	145

CHAPTER 1

INTRODUCTION

1.1. Motivation

Studies on new fuel-saving technologies have been popular in recent years because of decreasing global crude oil supplies and growing environmental concerns. The price of crude oil, according to the Department of Energy (2007), is over 400% higher than ten years ago (Figure 1.1) and is likely to continue to surge in the future because of shrinking oil supplies. To reduce oil consumption by ground vehicles, the Corporate Average Fuel Economy (CAFE) was enacted by the US Congress in 1975. The CAFE legislation is overseen by the National Highway Traffic Safety Administration (NHTSA), which sets fuel economy standards for cars and light trucks (trucks, vans, and sport utility vehicles) sold in the US. While the CAFE standards have remained relatively constant for the last twenty years, the discussion of increasing it is significant in the past fifteen years regarding shrinking oil supplies and increasing oil demands (Figure 1.2).

Concurrent with the implementation of increasingly stringent fuel-economy regulations is the adoption of the ever-tightening emission standards. These emission standards were set by the Environmental Protection Agency (EPA), which was formed in 1970 to develop and enforce regulations to protect the environment (EPA 2007). These standards focus on limiting the production of harmful tailpipe pollutants. The Tier 1

standards for example (DieselNet, 2007), published as a final rule in 1991 and phased-in progressively between 1994 to 1997, limited the allowable emission levels of THC, CO, and NO_x for all light-duty vehicles. The Tier 2 standards, adopted in 1999, is almost an order of magnitude more stringent compared to Tier 1 (Figure 1.3).

In light of the impending increases in CAFE regulations and the implementation of Tier 2 emissions standards, the automotive industry faces substantial challenges to improve fuel economy while reducing emissions. Various engine-based technologies—such as variable valve timing, turbocharger application, and cylinder deactivation—have only limited impact on fuel economy (Energy and Environmental Analysis, Inc., 2005). Continuously variable transmission is promising, but its in-field performance has not been satisfactory (Setlur et al., 2003). Diesel-fueled vehicles have been offered in the US with limited success. Recent availability of low-sulfur (15ppm) diesel fuel paves the way for more light-duty diesel vehicles, which might jump-start the sales of light diesel vehicles in the US. Currently, however, with only a handful of models from Mercedes, Volkswagen, and Jeep on the market, it is unlikely the sales volume of diesel vehicles will take off quickly in the near future. Fuel-cell vehicles, with hydrogen gas as a power source replacing the conventional engine, draw numerous interests because they have the potential to significantly reduce fuel consumption and emissions. However, there are still many unsolved challenges and the high-volume production of fuel cell vehicles is still decades away. Among all the technologies that are currently under development, the hybrid electric propulsion seems to be one of the most promising short-term solutions.

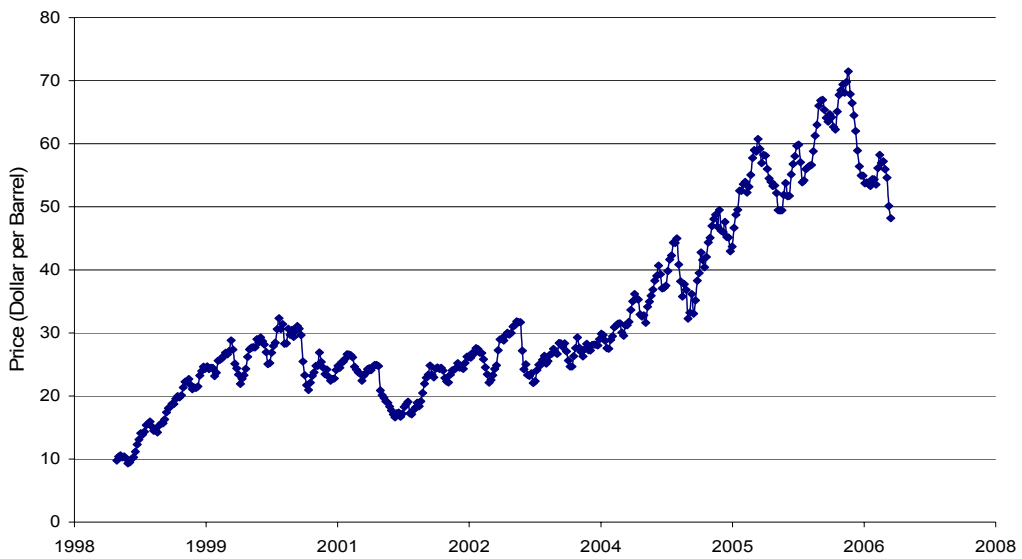


Figure 1.1: World crude oil price have increased over 400% since 1998 (DOE, 2007)

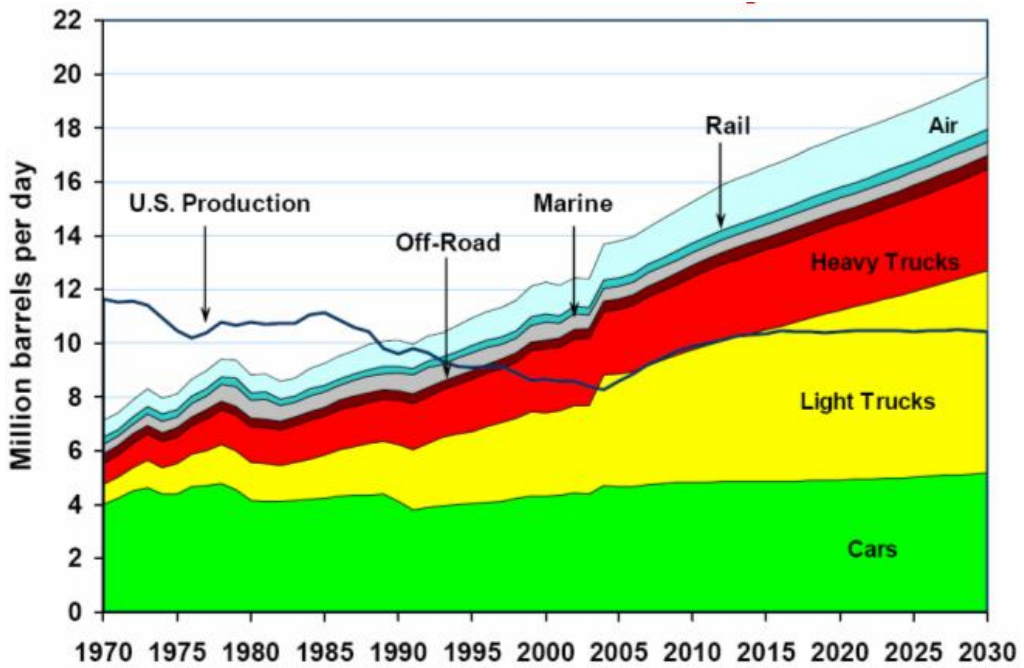


Figure 1.2: United States petroleum production and consumption (ORNL, 2006).

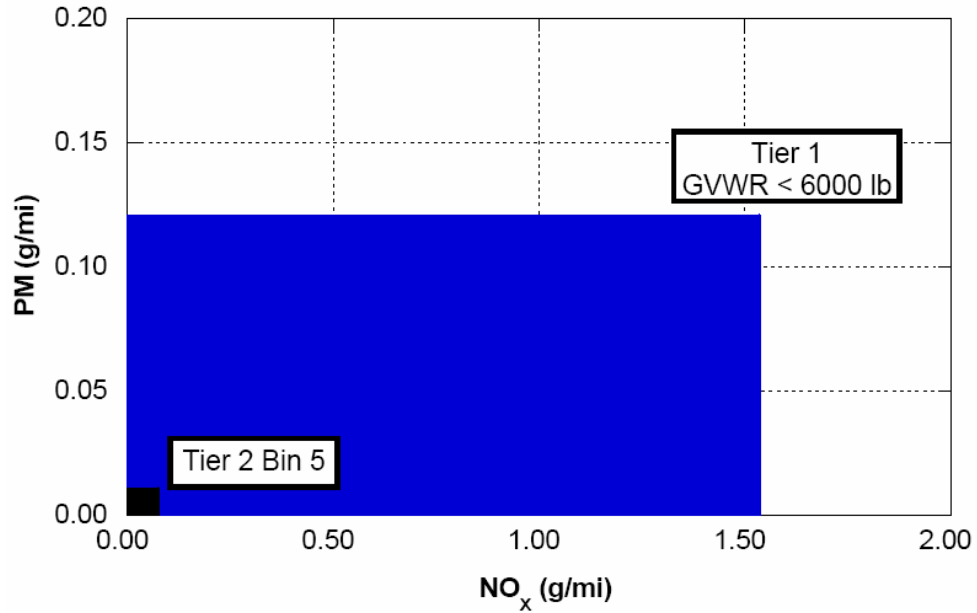


Figure 1.3: EPA NO_x and particulate matter regulation trends (DieselNet, 2007).

1.2. Background

A hybrid electric vehicle (HEV) adds an electric power path to the conventional powertrain, which helps to improve fuel economy by engine right-sizing, load leveling, and re-generative braking. A right-sized engine has better fuel efficiency, lower heat loss, and reduced peak power. The reduced power is compensated by an electric machine (or machines) during surged power demand. Compared with internal combustion engines, electric machines provide torque more quickly, especially at low speed. Therefore, launching performance can be improved, even with reduced overall rated power. Load leveling can also be achieved by the electrical path. With the electric drive assistance, the engine can be controlled to operate in an optimal region regardless of the road load. Finally, when the vehicle is decelerating, the electric machine can capture part of the vehicle's kinetic energy and recharge the battery.

Due to their significant potential in reducing fuel consumption and emissions, HEVs are now actively developed by many car companies. In late 1997, Toyota Motor Corp. released the first-generation Prius, which features the Toyota hybrid system (THS). It came to the US market in MY2000. Four years later, the MY2004 Prius model was released. It featured an improved powertrain, the THS-II, with significantly improved vehicle performance, interior volume, and fuel economy. The new Prius is the most successful hybrid to date: Toyota has sold more than 350,000 Prius models in North America; Monthly sales averaged about 15,000 units in 2006. With this success, a scaled-up and more sophisticated version of THS (a.k.a. Toyota Synergy Drive) was developed, and two hybrid SUVs (Highlander and Lexus RX 400H) were offered in 2006. The Toyota hybrid family is getting bigger with the introductions of the Camry Hybrid and the Lexus GS 450h in 2007.

Honda, another pioneer in the field of commercial HEV, introduced its first commercial hybrid vehicle, Insight, to the US in 1999. It earned the highest combined EPA rating for fuel economy in a passenger car at 60/66 mpg (city/highway). In 2002, Honda released the Civic Hybrid as a competitor to the Prius and remains at the forefront.

American automotive manufacturers started to realize the impact of the hybrid electric vehicles entering the 21st century and initiated catch-up efforts in recent years. Ford, the first US automaker offering hybrids, released the Ford Escape hybrid SUV in late 2004. A more upscale version, the Mercury Mariner, was introduced at the same time. General Motors, DaimlerChrysler, and BMW launched a joint effort to explore hybrid technologies and compete in the market with a new Hybrid Development Center

formed in 2006. Many new HEV models are expected to be released in the US in the near future (as shown in Table 1.1).

Table 1.1: Hybrid electric vehicles on the horizon (Fueleconomy.gov, 2007).

Manufacturer	Model	Type	Estimated Date Available
Chevrolet	Equinox	SUV	2007
Chevrolet	Malibu	Mid-size Car	2007
Chevrolet	Tahoe	SUV	2007
GMC	Yukon Hybrid	SUV	2007
Mazda	Tribute Hybrid	SUV	2007
Chevrolet	Silverado Hybrid	Full-size Pickup	2008
Ford	Fusion	Mid-size Car	2008
GMC	Sierra Hybrid	Full-size Pickup	2008
Mercury	Milan Hybrid	Mid-size Car	2008

As the HEV development getting more and more attentions, various designs and technologies emerge and apply to the production vehicles. These designs can be categorized by their degrees of hybridization or their powertrain configurations.

Based on the degree of hybridization, the HEVs can be divided into several categories: mild hybrid, power-assist hybrid, full hybrid, and plug-in hybrid. A mild hybrid is a conventional vehicle with an oversized starter motor, allowing the engine to be turned off whenever the car is coasting, braking, or stopped, yet restarted quickly. A power-assist hybrid uses the engine for primary power, with a torque-boosting electric motor connected to a largely conventional powertrain. The electric motor, typically

mounted between the engine and transmission, operates not only when the engine is off, but also when the driver “steps on the gas” and requires extra power. A full hybrid, sometimes called a strong hybrid, is a vehicle that can run on just the engine, just the battery, or a combination of both. A large, high-capacity battery pack is needed for the battery-only operation. A plug-in hybrid is a full hybrid, able to run in electric-only mode, with even larger batteries and the ability to recharge from the electric power station. They are also called gas-optional, or griddable hybrids. Their main benefit is that they can be gasoline-independent for daily commuting, but also have the extended range of a hybrid for long trips.

Based on the powertrain system design, the HEV models can be divided into three categories: parallel hybrid, series hybrid, and power-split hybrid. The definition and characteristics of each type are described in the following sections. My work mainly focuses on the power-split type of HEVs.

1.2.1. Parallel Hybrid Electric Vehicle

The parallel configuration, as shown in Figure 1.4, includes two separate power paths. In addition to a conventional engine transmission powertrain, a power assist device, often a motor/generator (MG) supplied by a battery or ultra-capacitor, is built in as the alternative propulsion system. When the secondary power source (i.e., the MG) is relatively small (mild hybrids or power-assist hybrid), it can not fully drive the vehicle without engine power. When the secondary power source is relatively large (full hybrids), the engine and MG can drive the vehicle individually or simultaneously.

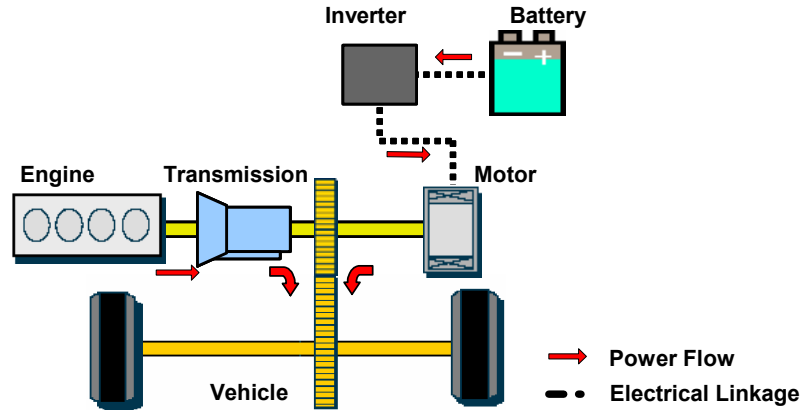


Figure 1.4: Parallel HEV configuration.

The role of the MG is to assist the engine to operate efficiently and to capture regenerative braking energy. The BSFC fuel map of the Saturn 1.9L (95kW) DOHC SI engine is shown in Figure 1.5 as an example representing a typical engine. The most efficient spot is located at the middle of its operating range (between the two dotted lines). Outside of this region, the fuel efficiency decreases. For the area pointed by arrow A, the MG is driven to supply the power demand to avoid using the engine inefficiently. On the other end as pointed by arrow B, the power that the engine can produce approaches its limit and becomes inefficient. The MG turns on to supplement the engine power.

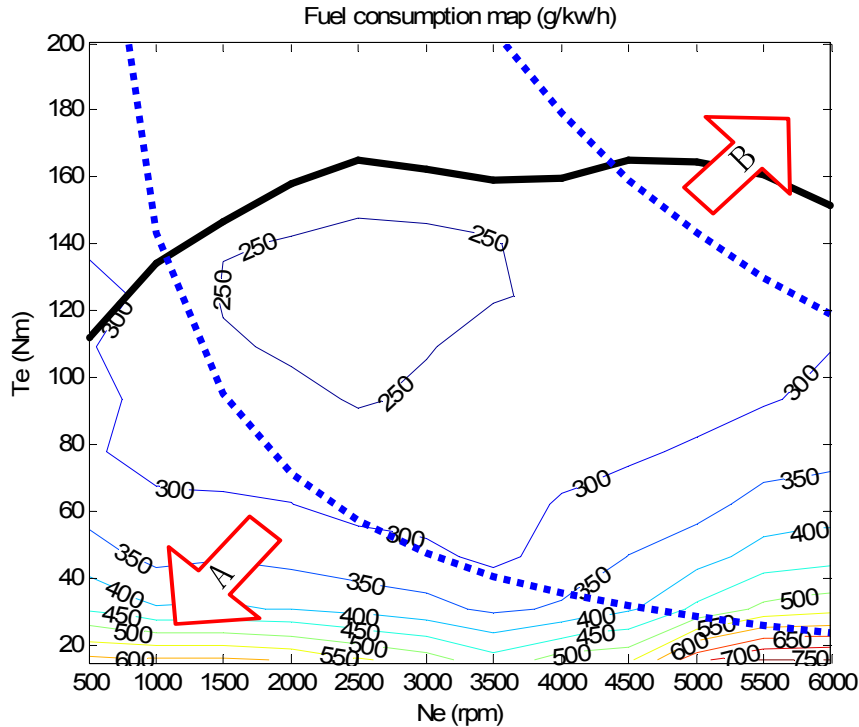


Figure 1.5: BSFC fuel map for a Saturn 1.9L (95 kW) DOHC SI engine

Depending on the connection between the transmission, MG, and the engine, the parallel configuration may have many different formats (Rahman et al., 2000). However, the power-flow analysis remains the same and relatively straightforward. For a mild parallel hybrid, the power management control becomes much simpler, as the two power sources do not work simultaneously. While for a full parallel hybrid, the control algorithm can be a lot more elaborative (Nedungadi and Dardalis, 1999; Lin et al., 2003; Delprat et al., 2004; Sciarretta et al., 2004). Honda's hybrid Civic with the integrated motor assist system (IMA) (Ogawa et al., 2003) clearly belongs to the parallel type.

Because the MG cannot be used to both charge the battery and assist the engine simultaneously, the power assistance has to be constrained to avoid draining the battery. This situation mostly occurs during city driving, where frequent stop-and-go demands

force the engine to produce power in its low-efficiency range. This is why most parallel HEVs do not have impressive city fuel efficiency if compared to other types of hybrid vehicle with a similar size.

1.2.2. Series Hybrid Electric Vehicle

The series configuration only has the motor (sometimes motors) driving the wheels—the engine is not directly connected to the wheels (as shown in Figure 1.6). The motor power is supplied by either a power-storage device (such as a battery), or a generator (transforming the mechanical power from engine into electric power), or the combination of both with a split ratio determined by the power management controller. Since the engine operation is independent of the vehicle speed and road condition, it is controlled to operate near its optimal condition most of the time. In addition, because the mechanical power transition path is eliminated, the energy loss due to the torque converter and the transmission is avoided.

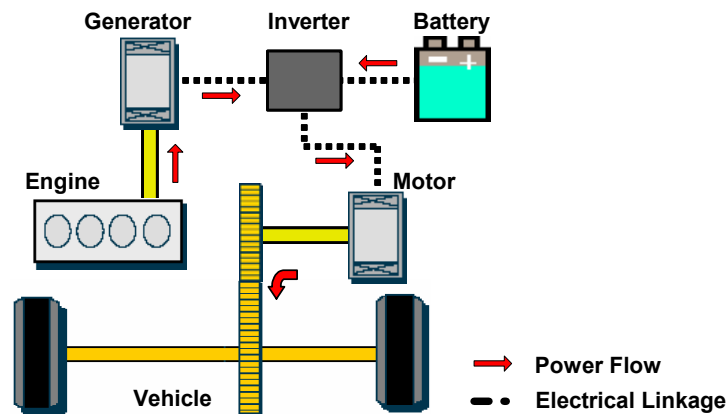


Figure 1.6: Series HEV configuration.

The control strategy of the series configuration is relatively simple (Waltermann, 1996; Jalil et al., 1997; Michelena et al., 2001), because the power-flow analysis for

series HEV is straightforward and the engine is controlled separately from the vehicle operation. Many prototype hybrid buses and trucks use the series hybrid configuration (Brahma et al., 2000).

A disadvantage of the series configuration, however, is that the efficiency of the electric machine(s) reduces the overall performance. The power flow through an electrical path has a lower efficiency than that through a mechanical path because the additional magnetic electric field transformation and the heat lost of the electric accessories. Since the driving power of a series hybrid vehicle flows through the electrical path all the time, it becomes relatively inefficient when the vehicle reaches the driving range that could be more efficiently driven by engine directly. This is true especially when the vehicle is running on the highway.

1.2.3. Power-Split Hybrid Electric Vehicle

This research focuses on the power-split type of HEVs. The powertrain configuration of the power-split hybrid system, also known as parallel/series hybrid or combined hybrid, is interesting because with proper control strategy it can be designed to take advantage of both parallel and series types and avoid their drawbacks.

As shown in Figure 1.7, the power-split configuration combines the parallel and series powertrains. On one hand, similar to the parallel configuration, it has the separate engine power-flow path and battery-motor power-flow path. Instead of transmission, it implements a power-split planetary gear set, to link the engine with the final drive. On the other hand, similar to the series configuration, it has the engine-generator power-flow path. The engine drives a generator to either charge the battery or supply power to the motor. With such a configuration, a power-split hybrid can operate like a series hybrid

when driving at low speed to avoid the drawback of parallel hybrid and can switch to the parallel hybrid when running at high speed to avoid the drawback of series hybrid. Because it has more energy flow paths and operating modes compared to other configurations, the power management control becomes more complicated.

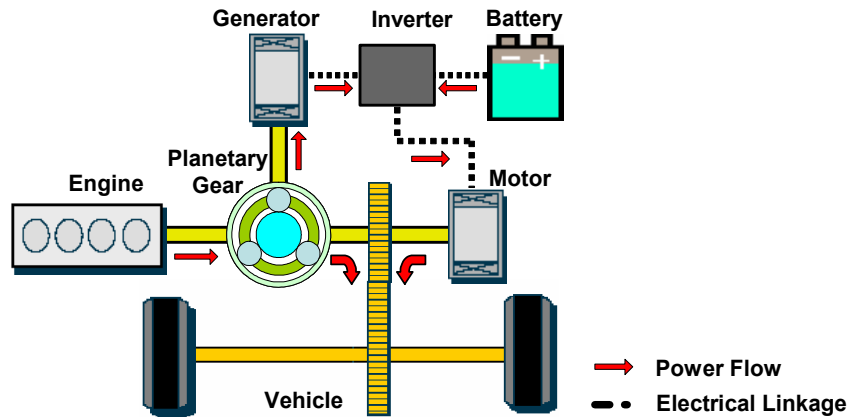


Figure 1.7: Power-split HEV configuration.

Development of the power-split mechanisms can be tracked back to the late 1960s (Livezey, 1969) and early 1970s (Gelb et al., 1971). The earliest of such devices appeared in the hydrostatic power-split transmission commonly used on lawn tractors. Considered as an electric continuously variable transmission (ECVT), operating at different speeds without actuating a clutch, it became useful for power transfer. As reviewed by Miller and Everett (2003), the flywheel-transmission-internal-combustion hybrid vehicle (Beachley and Frank, 1980; Besel and Hou, 1980; Cornell et al., 1980) and planetary gear train with CVT mechanism (Wohl et al., 1993) were designed and studied as early power-split devices. But this power-split concept was not applied to passenger vehicles until the late 1990s. The first production power-split passenger vehicle, the Toyota Hybrid System (THS), was introduced by Abe, (1997), Sasaki (1998), and Hermance (1999). This

system, often known as a single-mode system, is the major framework of the vastly popular Prius and the rest of the hybrid fleet from Toyota. New technologies of the hybrid electronic control unit (Nagasaka et al., 1998), variable-voltage power circuit including a DC/DC boost converter (Muta et al., 2004; Kawahashi, 2004), front-and-rear-motor drive (Kimura et al., 2005), motor speed-reduction device (Kamichi et al., 2006), and modification of the planetary gear train (Hermance and Abe, 2006) kept this system as a front-runner on the market. Another major design for power-split HEV on the market is the Allison Hybrid System (Holmes et al., 2003), also known as AHSII. This system, invented by GM as a dual-mode power-split system, is applied to several mid-sized SUV and pickup trucks and has become a major competitor in recent years.

Figure 1.8 shows a powertrain design example of the single-mode power-split hybrid system. A single planetary gear set serves as a power-split device that transfers the engine power to the vehicle through two paths: a mechanical path and an electrical path. The engine power through the mechanical path goes directly to the final drive of the vehicle. The rest of the engine power goes to the motor/generator 1 (MG1), where it is transformed into electricity. This power is then either stored in the battery or send to the motor/generator 2 (MG2) by a controlled power bus. The design of the planetary gear allows the engine speed to run at a continuously variable ratio in respect of the vehicle speed, which benefits the fuel efficiency. This CVT type of operation is controlled by maneuvering the electric motors, an operation often referred as ECVT (Miller 2005). Obviously, the engine power going through the electrical path is less efficient than the mechanical path from an instantaneous viewpoint. However, the energy stored in the

battery may be used more efficiently later, which helps to improve the overall vehicle fuel economy.

In this powertrain design, the carrier gear connected to the engine is the input node. The ring gear connected to the final drive is the output node. One of the electric machines is also connected to the output node, with the other MG connected to the third node of the planetary gear set. This setup is called an input-split system because the engine torque is split into two paths from the input node (More detailed definition of different split modes is given in Chapter 4). The split power then goes to the output node without any further split ratio. And since this is the only operating mode, it is called a single-mode system.

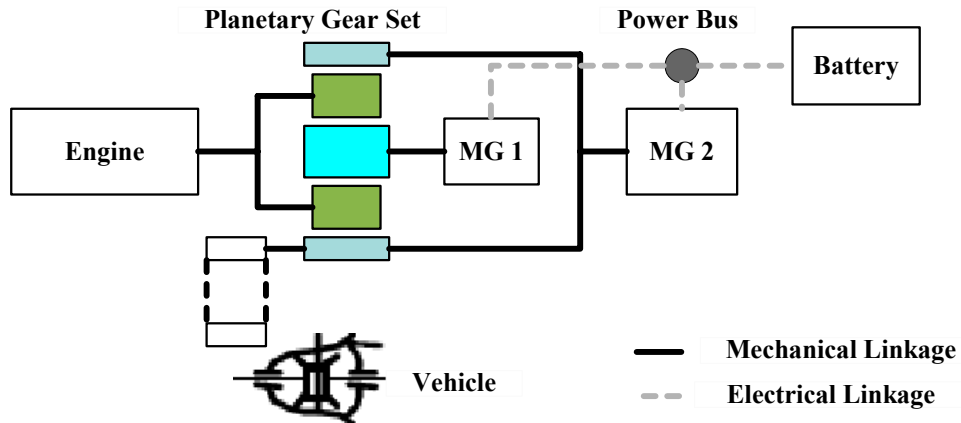


Figure 1.8: Powertrain configuration of a single-mode hybrid system.

Figure 1.9 shows a powertrain design example of the dual-mode power-split hybrid system. Compared to the single-mode system, this dual-mode system has one more planetary gear set and two clutches. Similar to the single-mode system, the engine power flows into the gear trains and is split into a mechanical power path and an electric power path. The dual-mode is named as such because it consists of two different power-split modes and can be switched from one to another by coordinately locking and

unlocking the two clutches. The powertrain shown in Figure 1.9 can be operated as an input-split system, which is the same as introduced in the last section, and can be operated as an compound-split system, in which after the engine torque input is split, these torques go through two different paths to the final drive with another split ratio (This concept will be explained in details in the Chapter 4). Although the system appears more complex, such dual-split modes prove to provide higher flexibility (Conlon, 2005; Grewe et al., 2007).

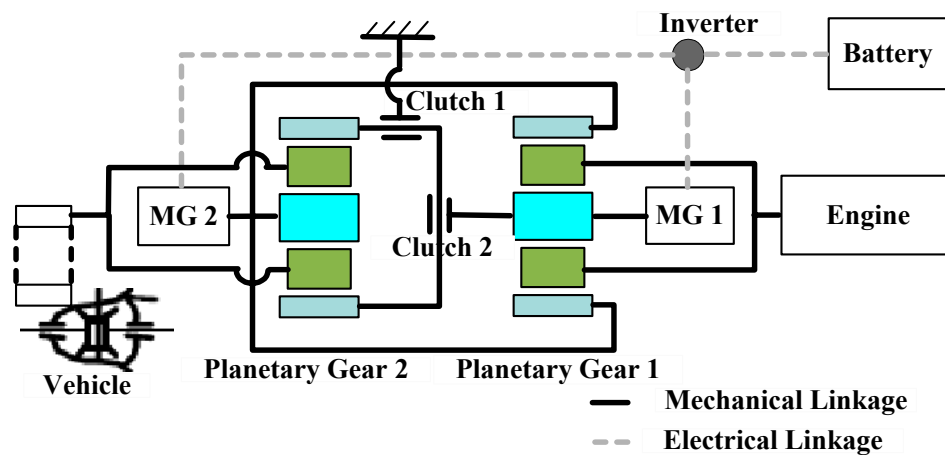


Figure 1.9: Powertrain configuration of a dual-mode hybrid system.

The two examples described above are just two possible configurations of the numerous power-split powertrain designs. Besides these two, there are many different power-split configurations under development. Detailed review is addressed in the next section.

1.3. Literature Review

1.3.1. Modeling of Power-Split HEVs

Having a proper modeling and simulation tool is very important in the early design and analysis stage. This is even more critical for the power-split HEVs since there could be numerous possible configurations/components and various control strategies. One of the most popular HEV simulation model packages is the ADvanced VehIcle SimulatOR (ADVISOR), developed by the National Renewable Energy Laboratory (2007). ADVISOR is an empirical, map-based simulation tool that combines the vehicle dynamics model with the efficiency map of each component to predict system performance. It calculates the powertrain operation backward from a given driving schedule, based on a quasi-static assumption that inverts the physical causality (Guzzella and Amstutz, 1999; Wipke et al., 1999; Markel et al., 2002; Wang, 2002).

Another popular HEV simulation model is the PNGV System Analysis Toolkit (PSAT) which was developed by the Argonne National Laboratory (ANL) (Rousseau et al., 2001a). Research with hardware testing on power-split HEVs has been under development in ANL for years (Duoba et al., 2000; Duoba et al., 2001; Ng et al., 2001). The experiment data is applied to validate and improve the simulation model (Rousseau et al., 2001b). In contrast to ADVISOR, PSAT is a forward-looking model that calculates the powertrain states, based on driver input. It is suitable for investigating the dynamic response of individual components as well as designing the control strategy for hybrid vehicles, although forward models are computationally more intensive than backward models. Besides these two highly refined software, Rizzoni et al. (1999) used high-level, unified power flow concepts, defined a general structure for each sub-system, and parameterized the structure's characteristics to allow for design study; Lin et al. (2000) developed a vehicle simulation model in Matlab/Simulink, which was applied to a power

management optimization study. But these models have not been applied to power-split configurations.

As attention was drawn towards power-split HEVs, studies on their powertrain systems modeling became popular. Zhang et al. (2001) derived a dynamic model to evaluate the transmission performance. This model focused on a particular dual-mode powertrain design. Rizoulis et al. (2001) presented a mathematical model of a vehicle with a power-split device based on the steady-state performance. A split-type hybrid vehicle model was developed by Zhang et al. (2004) to apply sequential quadratic programming to achieve the optimal control algorithm. Miller (2005) summarized the models of current power-split HEV architectures. A comparative analysis of the system efficiency among different power-split configurations was done by Conlon (2006), who used a mathematical model to present the gear split ratios regardless of the powertrain designs. Despite these early efforts, to our knowledge a complete power-split HEV forward-looking dynamic model that is suitable for both configuration design and control-algorithm development does not yet exist in the literature. Such simulation model needs to be complex enough to accurately describe the powertrain dynamics, and yet simple enough to be used in iterative optimizations. It is also important for this model to be flexible enough to cover a wide variety of different designs.

1.3.2. Configuration Design of Power-Split HEVs

The configurations of power-split HEVs can be varied with different engine-to-gear connections, motor-to-gear connections, or clutch-to-gear connections. Besides serving the purpose of power transferring, these different gear train linkages allow different kinematic relations between the power source components and provide different

powertrain operating options. As mentioned before, the Toyota Hybrid System is a single-mode power-split design (Koide et al., 1999). It has been modified with different gear linkage to achieve motor torque multiplication for heavier vehicles in recent years (Hermance and Abe, 2006). Schmidt (1996a) from GM introduced the concept of multi-modes on a power-split system based on the conventional transmission design knowledge. Although the planetary gear with electric machines provides CVT type of operation, having multi-gear modes on different driving scenario can be beneficial for overall transmission efficiency and relax the constraints on power source components. Investigation on this direction was continued and numerous designs with gear train variations can be found in the literature (Schmidt, 1996b; 1996c; Holmes and Schmidt, 2002; Schmidt, et al., 2006, etc.) Some of these designs consist of two planetary gears (Holmes et al. 2003; Ai and Mohr, 2005) and some of these designs consist of three or more planetary gears (Schmidt, 1999; Raghavan et al., 2007). For a single planetary gear, there are three gear nodes that can be used to link to other gears or power sources. More planetary gears provide more flexibility in gear gains and gear shifting options. With this large number of configuration possibilities, there can be thousands of design options for a power-split vehicle. This provides great freedom for the hybrid vehicle design, but the tasks of exploring various designs and finding the optimal solution with the best control execution become challenging.

To design a power-split hybrid vehicle, the engineer typically first selects one, among many different configurations, to focus on. The design parameters (e.g., motor size, battery size, planetary gear sizes, etc.) and control strategy then need to be determined. Obviously, to achieve near-optimal overall performance, an iterative process

needs to be executed. However, the problem for this approach is that even with the optimal performance, how one can claim the selected configuration offers the best solution among all possible configurations. To achieve this goal, the exact same process from selecting another configuration and iteratively approaching the optimal performance has to be repeated. Moreover, only when the optimal performance is gained for each configuration, then the comparison between them is a sensible exercise. With the numerous options for the configuration design variations, such an iterative process only can be achieved with a systematic method with many underlying techniques, which including automated model generation and simulation with optimal design and optimal control techniques.

Computer-aided method for gear design is not a new concept (Achtenova and Svoboda, 2003). In fact, many systematic ways to search among different designs have been proposed for transmission designs (Freudenstein and Yang, 1972; Kaharaman et al., 2004). The studies on power-flow analysis of planetary gear trains were mostly performed as a part of efficiency formulations. Pennestri and Freudenstein (1993a; 1993b) and Hsieh and Tsai (1998) showed good examples of such investigations. Pennestri and Freudenstein (1993a) used the same fundamental circuits proposed earlier (Freudenstein and Yang, 1972) for a complete static force analysis. Hsieh and Tsai (1998) applied a similar formulation in conjunction with their earlier kinematics study (1996) to determine the most efficient kinematic configurations. The work by Castillo (2002) further generalized the efficiency formulations of gear trains formed by single- or double-planet arrangements. In this dissertation, a computer-aided method to study the power-flow on planetary gear trains in a power-split HEV is introduced. It opens a door

for investigating massive number of designs and approaches the optimal solution systematically.

1.3.3. Control of power-split HEVs

In the control of power-split hybrid vehicles, two-level hierarchical control architecture is commonly used (Figure 1.10). On the lower level, every sub-system (e.g., engine, motor, battery, etc.) is equipped with sensors, actuators, and a control system to regulate its behavior. On the higher level, a supervisory control system represents a vehicle-level controller that coordinates the sub-systems to satisfy certain performance targets (e.g., fuel economy). It must determine the desired output to be generated by the sub-systems and send these output signals to the corresponding sub-systems.

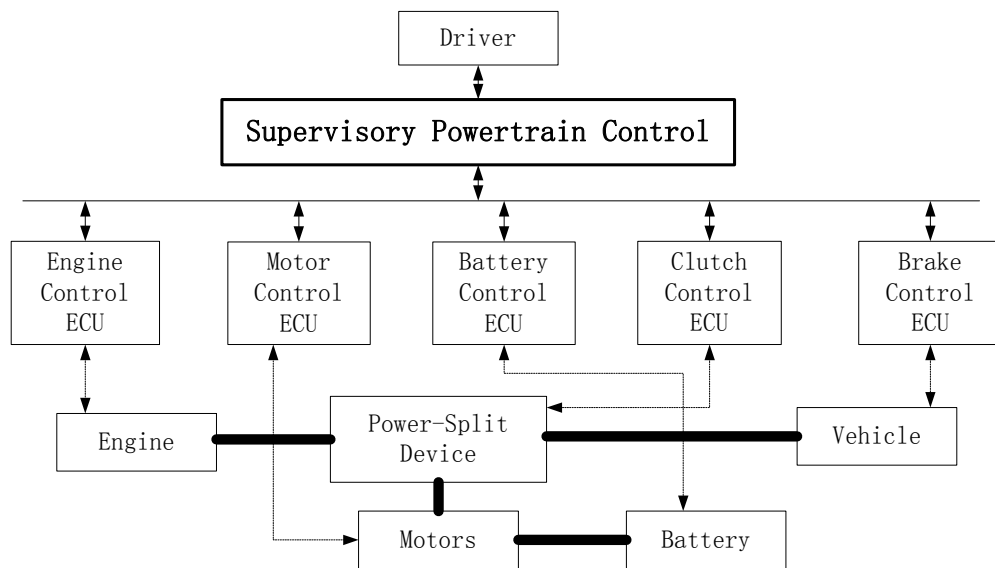


Figure 1.10: Hierarchical control architecture of a power-split hybrid electric vehicle.

In general, the supervisory control strategies of hybrid vehicles in the existing literature can be classified into three categories. The first type employs heuristic control

techniques such as control rules/fuzzy logic for control algorithm development. This approach is based on the concept of load-leveling, which attempts to operate the internal combustion engine in an efficient region and uses the reversible energy storage device (e.g., battery or ultracapacitor) as a load-leveling device to provide the rest of the power demand (Jalil et al., 1997; Rahman et al., 2000; Jeon et al., 2002). A popular strategy is to adopt a rule-based structure in the control logic by defining a set of thresholds through an optimization process (Piccolo et al., 2001; Wipke et al., 2001). There has been much other research on the implementation of load-leveling and charge-sustaining strategy by using a fuzzy logic technique (Farrall et al., 1993; Lee and Sul, 1998; Schouten et al., 2002). The second approach is based on instantaneous optimization methods that decide at any moment the proper split between the energy sources by minimizing a cost function. Equivalent consumption minimization strategy (ECMS) is a typical example of the instantaneous optimization. In this strategy, electric power is translated into an equivalent (steady-state) fuel rate to calculate the overall fuel cost (Kim et al., 1999; Paganelli et al., 2000; Paganelli and Ercole et al., 2001; Paganelli and Tateno et al., 2001; Won et al., 2005). A recently developed method, the adaptive-ECMS technique (Pisu et al., 2004; Musardo et al., 2005), periodically refreshes the converting factor according to the current road load to sustain the battery SOC. The third approach is based on optimization methods that optimize a cost function over a time horizon. A popular method used is dynamic programming (DP), which calculates the optimal control signals over a given driving schedule (Lin et al., 2001; Lin, Peng, Grizzle, Liu et al., 2003; Lin, Peng, Grizzle, and Kang, 2003; Zhang et al., 2004). Another method, developed by Delprat et al. (2001; 2004), applied optimal control theory by (Lewis and Syrmos, 1995)

to achieve global optimal strategy. The solutions from all these approaches are optimized with respect to a specific driving cycle and might be neither optimal nor charge-sustaining under other cycles. To solve this problem, Lin et al. (2004) proposed a stochastic dynamic programming (SDP) method, in which the vehicle model is deterministic but the driver power demand is stochastic. This reflects the fact that the optimization is not for any specified driving cycle but rather for general driving conditions with known power demand probabilities. This approach is also computationally extensive and to avoid such a problem, Kim and Peng (2006) suggested a parameterizable, near-optimal controller inspired by SDP, and Tate (2006) quantized the state space and solved a shortest path SDP by using a combination of linear programming and barycentric interpolation.

Despite these efforts of the supervisory control development, the development of the control strategies for the power-split hybrid vehicle systems is still worth of investigating. Firstly, the power-split system offers more control inputs and more flexible operating options than other vehicle systems. As a result, the optimal control development that involves with intensive computation (e.g., DP) faces more challenges that never occur before. Secondly, the powertrain configuration of a power-split HEV compromises extra kinematic constraints between different power sources which imply modifications in the existing control strategies. Thirdly, to our knowledge there has not been any comparison between different optimal control strategies on the power-split HEV systems. This dissertation will address our work on these areas.

1.4. Contributions

This dissertation focuses on the process of power-split HEV modeling, design, and control optimization. A dynamic power-split hybrid vehicle simulation model is derived with a universal format created to present different powertrain configurations. Using this model, a combined configuration design and control optimization strategy is proposed for power-split HEVs. As shown in Figure 1.11, the iteration between the configuration design evaluation and automated model generation will provide an optimal solution for a power-split HEV with its benchmark performance. Different control optimization strategies are then applied to approach this benchmark. The main contributions of the dissertation include the following:

- A forward-looking dynamic model is created for power-split hybrid electric powertrain systems. The supervisory powertrain controller, driver model, and sub-system models (e.g., engine, power-split device, motor/generator, battery, and vehicle dynamics) are integrated to perform a closed-loop simulation. This simulation tool can be used to analyze the interaction between sub-systems and evaluate vehicle performance using measures such as fuel economy and drivability.
- A math-based universal model format is created that presents different designs of power-split powertrains. This universal model format presents the powertrain dynamics regardless of the various connections of engine-to-gear, motor-to-gear, and clutch-to-gear. With such a model format, a technique to quickly and automatically generate dynamic models for power-split hybrid powertrains is developed. This technique automates the process from powertrain design to dynamic model, and makes it possible to explore and evaluate many different configurations systematically.

- With the help of the automatically-generated dynamic power-split models, possible configuration designs can be systematically explored and screened. A design screening process is developed based on various design requirements including feasibility, drivability, power source component sizing, transmission efficiency, and possible mode shifting.
- A optimal control design procedure based on deterministic dynamic programming (DDP) is adopted in the power-split HEV fuel efficiency optimization study. DDP is employed to find the optimal operation of the power-split system and achieve the benchmarks for different powertrain configurations. The results are then applied to compare and evaluate different designs. This approach provides design engineers with fast, quantitative analysis of the power-split hybrid powertrain systems.
- With the DDP suggesting the potential performance benchmark of the selected powertrain configuration, two implementable control strategies are developed to apply to the power-split hybrid vehicles. The first design is based on the stochastic dynamic programming (SDP), which solves the power management problem based on a stochastically generated driver model. The second control design is developed from the equivalent consumption minimization strategy (ECMS), an instantaneous optimization concept. The configuration of the power-split system enforces more constraints to both of the control strategies. Both algorithms provide state-feedback controllers that can be used for real-time implementation.

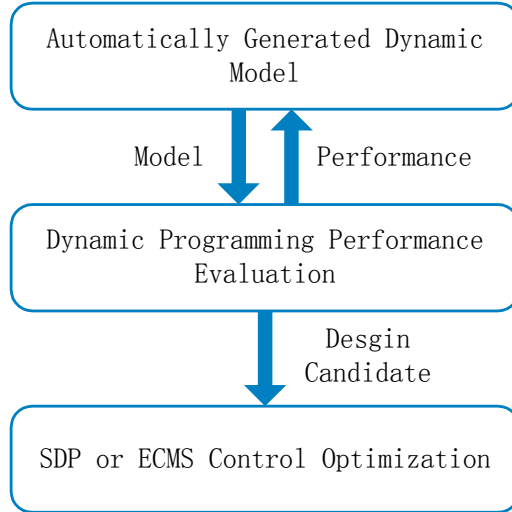


Figure 1.11: Combined configuration design and control optimization procedure.

1.5. Outline of the Dissertation

The organization of this dissertation is as follows. After the introduction in Chapter 1, the development of an integrated model for power-split hybrid electric vehicles is presented in Chapter 2. This model is further generalized to a universal format in Chapter 3. Based on this format, a method of automatically generating power-split powertrain models is proposed. This method allows us to systematically explore possible design candidates and approach optimal design and control solutions. Chapter 4 presents the configuration screening process and Chapter 5 presents the design and control optimization process. The optimal control in Chapter 5 benchmarks the potential performance in the optimal design. Two implementable control strategies by SDP and ECMS are developed in Chapter 6, which can be applied in real-time and approach the performance benchmark. Finally, a summary of this dissertation and suggested future work are presented in Chapter 7.

CHAPTER 2

DYNAMIC MODELING OF POWER-SPLIT HYBRID VEHICLES

In this chapter, a forward-looking simulation model is developed for power-split hybrid vehicles. This simulation model is applied to construct two virtual vehicles. The first one is the Toyota Prius. Most of the component parameters came from the ADVISOR software (National Renewable Energy Laboratory, 2005) and the published vehicle specifications (Toyota Motor Corporation, 2007). In year 2004, The THS is redesigned as THS-II, which provides significant vehicle performance improvement. Muta et al. (2004) compared the THS with the THS-II. The enhancement from the first generation to the second generation includes bigger component sizing, higher efficiency, and increased generator operating range. It appears that the power-split gear set remains as a single-mode system—i.e., the basic dynamic equations governing the vehicle remain unchanged. Due to the fact that much more information was available about THS (Duoba et al., 2000, 2001; Ng et al., 2001; Rousseau et al., 2001), compared with THS-II (Kawahashi 2004), a dynamic model based on THS is developed.

The second vehicle is a super-sized High Mobility Multi-purpose Wheeled Vehicle (HMMWV) with a dual-mode power-split Allison Hybrid System. The HMMWV is heavier than a stock version with additional armor and weapon on-board (Filipi et al., 2006). A suite of vehicle models developed in the Automotive Research Center (ARC) at the University of Michigan provided a foundation for this modeling

work. Various subsystem models have been integrated in Simulink as a common simulation environment to produce a tool for conventional vehicle simulation dubbed Vehicle Engine SIMulation - VESIM (Assanis et al., 2000). This platform has subsequently been expanded and utilized for investigating a number of research issues related to hybrid truck propulsion (Lin et al., 2001; Wu et al., 2004, Filipi et al., 2004, 2006; Liu et al., 2007). This model is updated with the dual-mode power-split powertrain and served as the platform to apply the combined design optimization and control optimization described in Chapter 4 and Chapter 5.

2.1. Overall Architecture

The simulation model is implemented in the Matlab/Simulink environment, as shown in Figure 2.1. A virtual driver is designed to follow a prescribed driving cycle, i.e., a speed trajectory specified over time. This modeled driver compares the reference vehicle speed and the actual vehicle speed to make driving/braking decisions. The decision commands are sent to the power management controller, which determines proper actions of power powertrain sub-systems. The rest of the modules represent the mechanical and electrical dynamics of the power-split HEV powertrain, which includes the power flows between the engine, motor/generators, and battery. The sub-system blocks shown in Figure 2.1 are described in the following section.

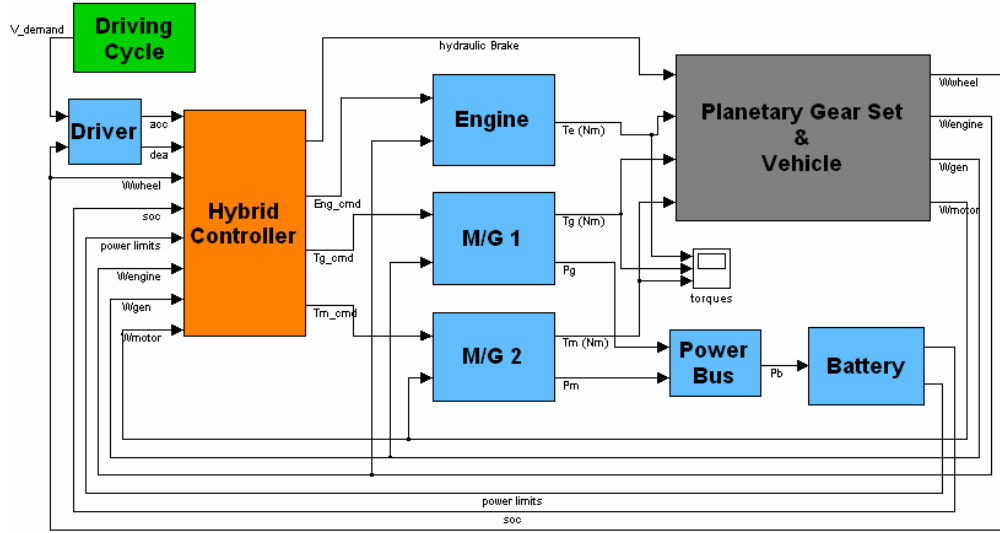


Figure 2.1: The overall architecture of a power-split HEV in Matlab/Simulink.

2.2. Sub-Systems/Components Modeling

2.2.1. Planetary Gear Set

The planetary gear, which mechanically connects the power from all three power sources, is the key device in a power-split HEV powertrain. It consists of three rotating axes, or nodes: the sun gear, the carrier gear, and the ring gear (as shown in Figure 2.2). These nodes are linked by a few small pinion gears. As a result of the mechanical connection through gear teeth meshing, the rotational speeds of the ring gear ω_r , sun gear ω_s , and the carrier gear ω_c satisfy the following relationship at all times

$$\omega_s S + \omega_r R = \omega_c (R + S) \quad (2.1)$$

where R , and S are the radii (or number of teeth) of the ring gear and the sun gear, respectively. Because of this speed constraint, a planetary gear only has two degrees of freedom, despite the fact that it has three nodes.

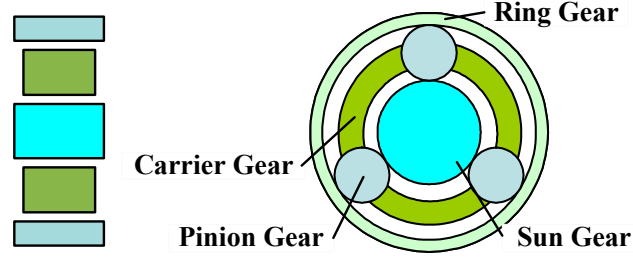


Figure 2.2: Composition of the planetary gear set.

Figure 2.3 shows the free body diagram of the planetary gear set. The mass of the pinion gears is assumed to be small and the pinion gears simply serve as an ideal force transfer mechanism. The dynamics of the gear nodes are then obtained as

$$\dot{\omega}_r I_r = F \cdot R - T_r \quad (2.2)$$

$$\dot{\omega}_c I_c = T_c - F \cdot R - F \cdot S \quad (2.3)$$

$$\dot{\omega}_s I_s = F \cdot S - T_s \quad (2.4)$$

where T_r , T_s , and T_c are the torques on the ring gear shaft, the sun gear shaft, and the carrier shaft, respectively, and I_r , I_s , and I_c are the corresponding inertia. F represents the internal force between the pinion gears and other gears.

If we further ignore the inertia of ring, carrier, and sun gears, from (2.2), (2.3), and (2.4), the torque signals on each node satisfy

$$T_s + T_r + T_c = 0 \quad (2.5)$$

And the power conservation of the whole gear system leads to

$$T_s \omega_s + T_r \omega_r + T_c \omega_c = 0 \quad (2.6)$$

Base on Equations (2.1), (2.5), and (2.6), we have

$$T_r = -\frac{R}{R+S}T_c \quad (2.7)$$

$$T_s = -\frac{S}{R+S}T_c$$

Equation (2.7) indicates that the torque input to the carrier gear is split by a fixed ratio to the ring gear and the sun gear. This ratio is determined by the design of the planetary gear set.

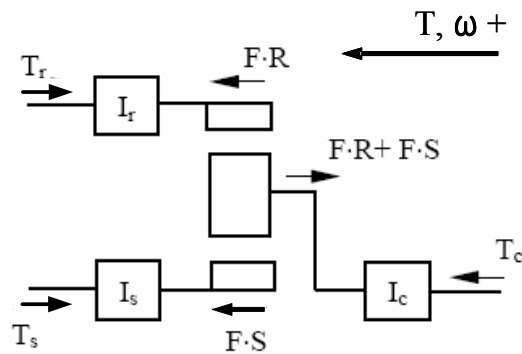


Figure 2.3: Force analysis on a planetary gear set.

A planetary gear can be used not only as a power-split device as explained above, but also as a power-ratio device if any of the three gear nodes is locked to the ground. If the ring gear node is locked, i.e., the ring gear speed is zero, then equation (2.1) now becomes

$$\omega_s S = \omega_c (R + S) \quad (2.8)$$

Since there is no power flow through the ring gear, the power conservation between carrier gear and sun gear leads to

$$\frac{\omega_s}{\omega_c} = \frac{T_c}{T_s} \quad (2.9)$$

The planetary gear is nothing but a power gear ratio.

The lever diagram representation is applied in this study for the gear linkage analysis. It was first introduced by Benford and Leising (1981) to present the speed constraint and simplify the torque analysis for the planetary gear set. As shown in Figure 2.4, the three gear nodes can be presented with vector length presenting the rotational speeds. Equation (2.1) then guarantees that the three gear nodes form a straight line. Note that positive speed is defined as clockwise when facing the gear sets, and as pointing to the right in the lever diagram.

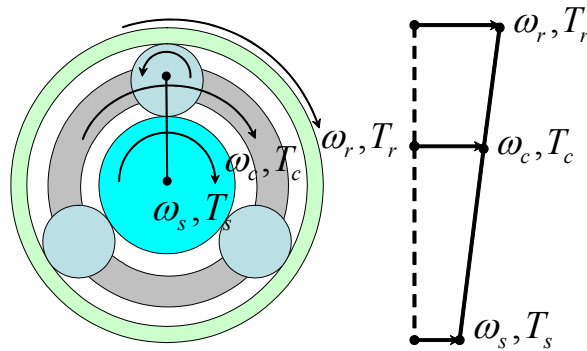


Figure 2.4: Planetary gear set and lever diagram.

2.2.2. Engine

The engine model is a look-up table that provides brake torque as a function of instantaneous engine speed and normalized fuel-injection rate. The engine transient response due to fuel injection and spark-timing control is ignored, and the working condition assumes constant average level. A BSFC map is implemented to calculate the fuel consumption. Figure 2.5 and Figure 2.6 show the Toyota Hybrid System engine torque look-up table and the BSFC map, respectively.

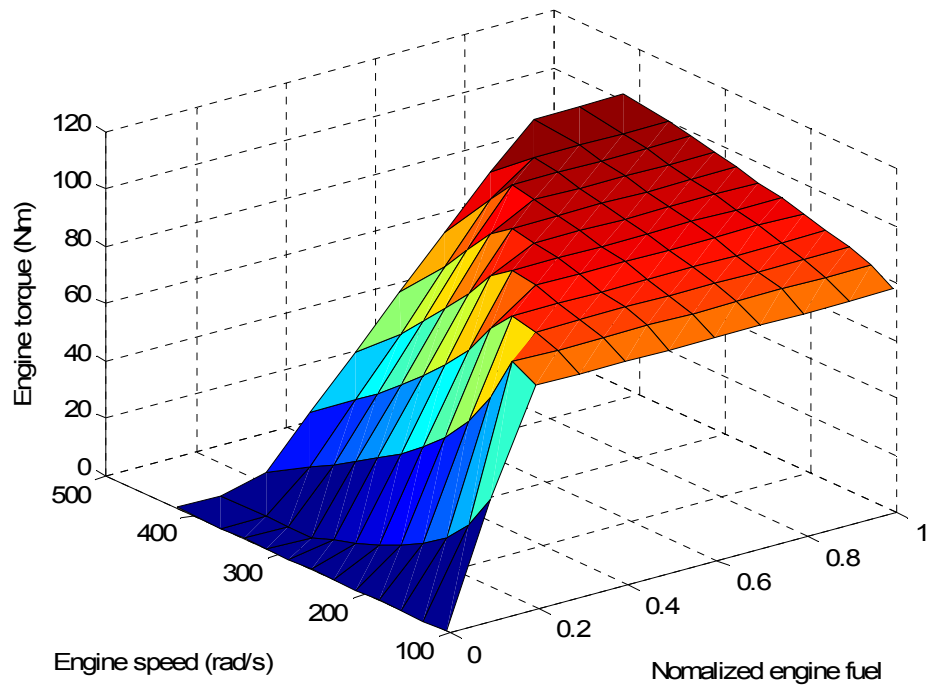


Figure 2.5: THS engine look-up table.

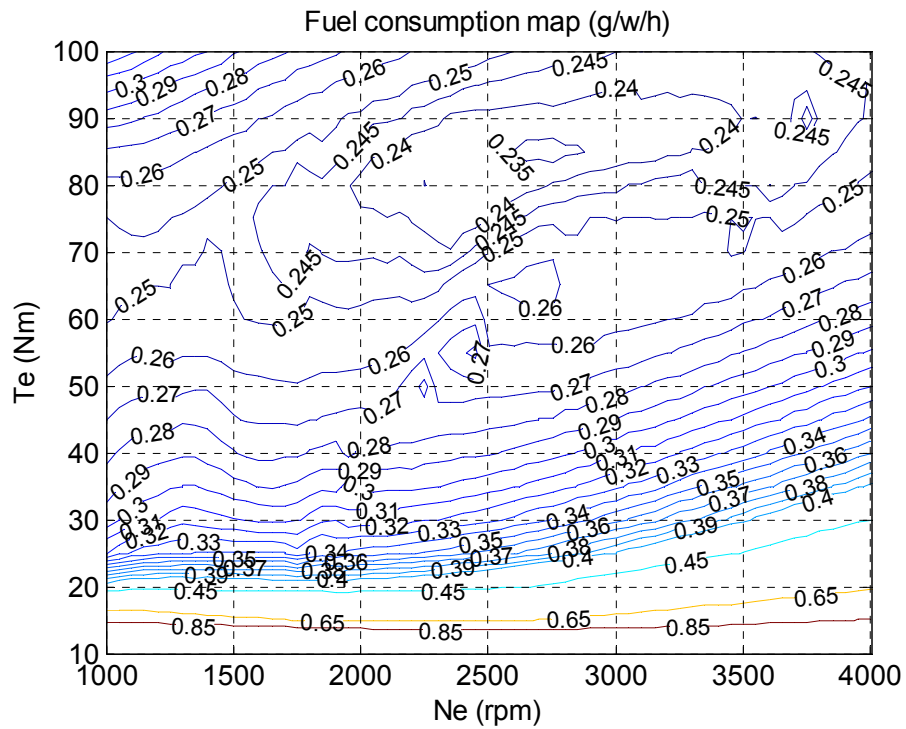


Figure 2.6: THS engine BSFC map.

2.2.3. Motor/Generator

The two permanent magnet AC motor/generators (MG), one at 15 KW (MG1) and the other at 35 KW (MG2) for THS vehicle, are both modeled using the motor equations published in the ADVISOR software. Simple electrical dynamics are used because they are much faster than the mechanical dynamics. The MG is assumed to be controlled to reach its demand torque with a small time delay. This delay is approximated by a first-order lag function. The power supplied to the MG is represented by

$$P_{MG} = T_{MG} \omega_{MG} \eta_{MG}^k \quad (2.10)$$

where T_{MG} and ω_{MG} are the torque and rotational speed, respectively. If the velocity and torque of the MG are of the same signs (i.e., both positive or both negative), the power is positive, which means the motor is consuming energy. Similarly, if the signs of velocity and torque are different (i.e., one positive, the other negative), the MG is generating energy. k is the sign of the power flow direction. When the MG is consuming energy, $k=-1$ and the power flows in from the battery to the MG. When the MG is generating energy, $k=1$ and the power flows out from the MG to the battery. The efficiency η_{MG} accounts for the energy lost from both the MG and other accessories, including the power converter and controller, which are not modeled. The efficiency is a function of motor torque and motor speed shown in Figure 2.7 and Figure 2.8 (ADVISOR 2002).

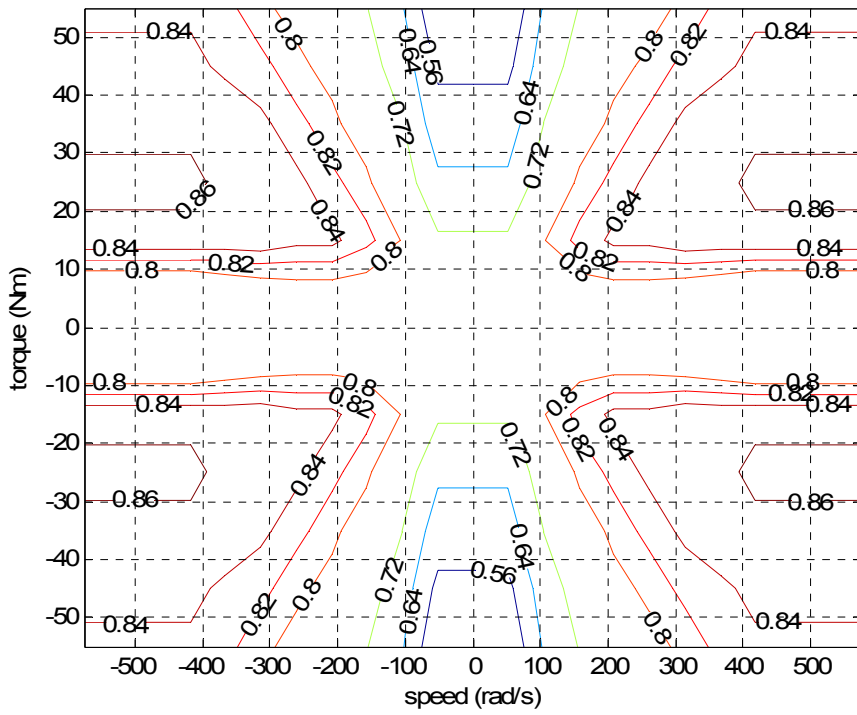


Figure 2.7: Efficiency map of the MG 1 (15 kW).

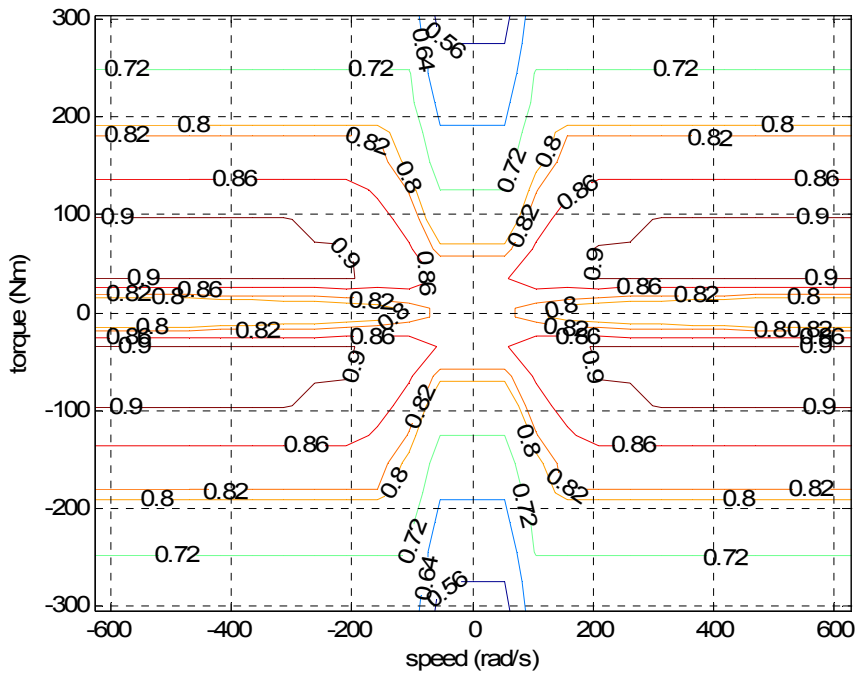


Figure 2.8: Efficiency map of the MG 2 (35 kW).

2.2.4. Power Storage Device (Battery)

The power requirements from the two MGs are supplied by the power storage device (battery) as

$$P_{batt} = (T_{MG1}\omega_{MG1}\eta_{MG1}^k \eta_{c1}^k + T_{MG2}\omega_{MG2}\eta_{MG2}^k \eta_{c2}^k) \quad (2.11)$$

As mentioned before, k is the sign of the power flow direction as explained in section 2.2.3. When the battery is discharged, $k=-1$ and the power flows away from the battery. When the battery is charged, $k=1$ and the power flows to the battery. η_c represents the efficiency of the power converter.

The battery model is an equivalent circuit with an internal resistance R , as shown in Figure 2.9. The open circuit voltage V_{oc} and R are both state-dependent parameters. They are lumped representations of complex chemical process, and are known to be functions of the battery's state of charge (SOC) and temperature. The battery temperature is assumed to be constant (20 °C) and the temperature effect is ignored. The dependency on SOC is modeled as lookup tables (Figure 2.10).

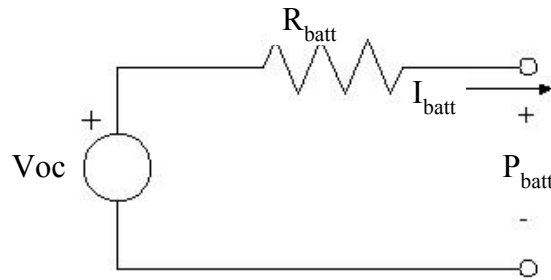


Figure 2.9: Internal R battery model.

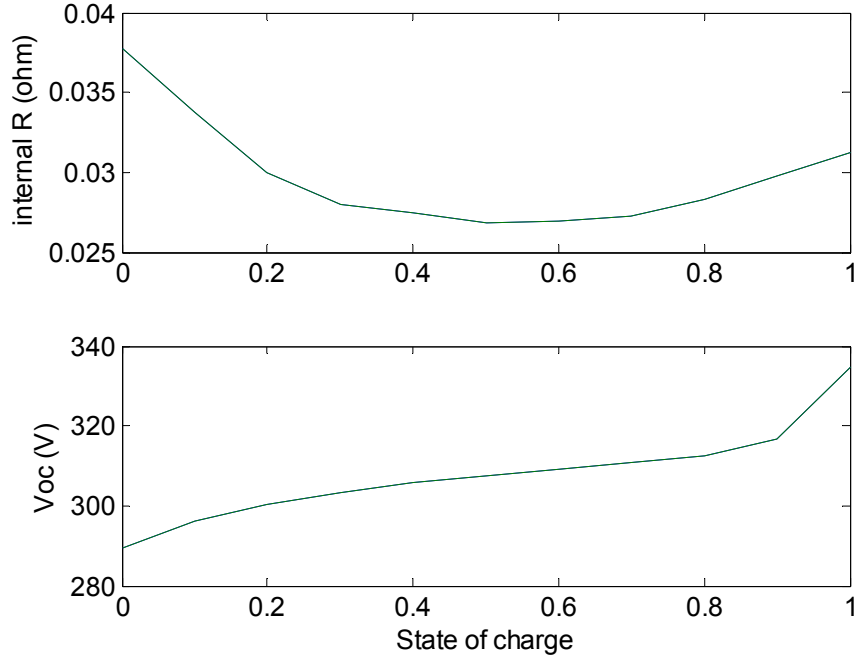


Figure 2.10: THS battery lookup tables (R and V_{oc} against SOC).

The SOC represents the electrical status of the battery and depends on the equivalent battery capacity Q_{max} and the current flowing through I_{batt} :

$$\dot{SOC} = -\frac{I_{batt}}{Q_{max}} \quad (2.12)$$

where Q_{max} is a function of temperature, and hence is approximated as a constant in this model. Battery current I_{batt} is a function of V_{oc} , R and it relates to the battery power output according to the relationship

$$P_{batt} = V_{oc} I_{batt} - I_{batt}^2 R_{batt} \quad (2.13)$$

From the quadratic equation (2.13), we have

$$I_{batt} = \sqrt{V_{oc}^2 - 4(P_{batt} R_{batt})} \quad (2.14)$$

2.2.5. Driver

A driver model is designed to follow the driving cycle, which is a speed trajectory specified over time. The driver is modeled as a PI feedback controller, as shown in Figure 2.11. The speed error between the actual vehicle speed and the desired speed is calculated and normalized before it is sent to the PI controller. In order to avoid saturation of the integral part, an anti-windup scheme is applied. Like a human driver, the driver model generates gas pedal command or braking pedal command (normalized between -1 and 1). The pedal command is then sent to the supervisory power management controller.

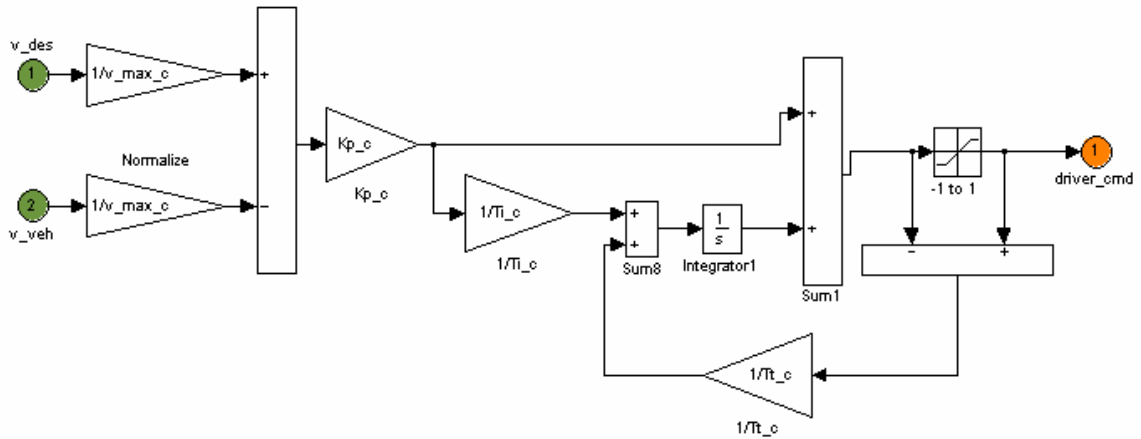


Figure 2.11: Driver Simulink model.

2.3. The Powertrain Modeling

A power-split HEV is different from other hybrid powertrains in terms of how to connect the power sources and the drive axle with the power-split device. Modeling of two specific drive trains, a single-mode and a dual-mode system, for the two virtual vehicles (THS and HMMWV) are introduced in this section. These models will be further simplified with a unified matrix format introduced in the next chapter.

2.3.1. Model of a Single-Mode Powertrain (Toyota Hybrid System)

The THS adopts a single-mode system as introduced in section 1.2.3. Figure 2.12 shows the free body diagram of the THS powertrain, with the rotational degrees of freedom shown in (conceptually) translational motions. The planetary gear system is represented by one lever diagram, which shows the internal torques between the gears defined before.

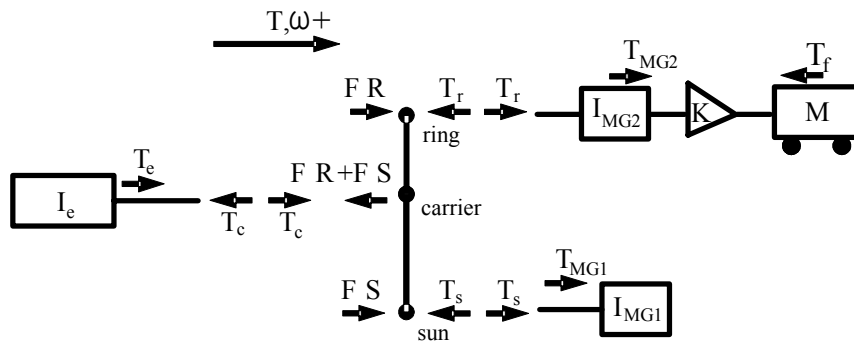


Figure 2.12: Free body diagram of the THS powertrain.

Outside of the planetary gear, the three power sources each exerts a torque to their respective gears to affect the vehicle's motion. Positive engine torque and motor torque (to the right) result in vehicle acceleration. For the MG1 rotational dynamics at the sun gear node, the governing equation is

$$\dot{\omega}_{MG1} I_{MG1} = T_s + T_{MG1} \quad (2.15)$$

where T_{MG1} , ω_{MG1} , and I_{MG1} are the MG torque, speed, and inertia, respectively. From Equations (2.4) and (2.15), we have

$$\dot{\omega}_{MG1} (I_{MG1} + I_s) = F \cdot S + T_{MG1} \quad (2.16)$$

Similarly, at the carrier gear node, the engine speed is governed by the equation

$$\dot{\omega}_e I_e = T_e - T_c \quad (2.17)$$

where T_e , ω_e , and I_e are the engine torque, speed, and inertia, respectively. From Equations (2.3) and (2.17), we have

$$\dot{\omega}_e (I_e + I_c) = T_e - F \cdot R - F \cdot S \quad (2.18)$$

The equation for the ring gear includes the dynamics of the vehicle because the final wheel shaft is connected to the ring gear node. Since the vehicle longitudinal dynamics is the dominating factor for fuel consumption, dynamics in other degrees of freedom are ignored. Furthermore, to simplify the equation we assume there is neither tire slip nor efficiency loss in the driveline. However, these assumptions might result in slightly higher fuel economy predictions. The governing equation for the ring gear shaft then becomes

$$\dot{\omega}_r \left(\frac{R_{tire}^2}{K^2} m + I_{MG2} \right) = (T_r + T_{MG2}) - \frac{1}{K} \left[T_f + mgf_r R_{tire} + 0.5 \rho A C_d \left(\frac{\omega_r}{K} \right)^2 R_{tire}^3 \right] \quad (2.19)$$

where $0.5 \rho A C_d$ presents the aerodynamic drag resistance, f_r is the rolling resistance coefficient, I_{MG2} is the inertia of the motor, K is the final drive ratio, m is the vehicle mass, R_{tire} is the tire radius, T_f is the brake torque applied by the friction brake system, and T_{MG2} is the motor torque. From Equations (2.2) and (2.19), we have

$$\dot{\omega}_r \left(\frac{R_{tire}^2}{K^2} m + I_{MG2} + I_r \right) = (T_{MG2} + F \cdot R) - \frac{1}{K} \left[T_f + mgf_r R_{tire} + 0.5 \rho A C_d \left(\frac{\omega_r}{K} \right)^2 R_{tire}^3 \right] \quad (2.20)$$

Equations (2.16), (2.18), and (2.20) represent the governing equations of the rotational motions of the MG1, engine, and MG2 (proportional to the vehicle), respectively. These equations can be combined with Equation (2.1) in a matrix form as

$$\begin{bmatrix} I_e + I_c & 0 & 0 & R + S \\ 0 & \frac{R_{tire}^2}{K^2} m + I_{MG2} + I_r & 0 & -R \\ 0 & 0 & I_{MG1} + I_s & -S \\ R + S & R & S & 0 \end{bmatrix} \begin{bmatrix} \dot{\omega}_e \\ \dot{\omega}_r \\ \dot{\omega}_{MG1} \\ F \end{bmatrix} = \begin{bmatrix} T_e \\ T_{MG2} - \frac{1}{K} \left[T_{fb} + mgf_r R_{tire} + 0.5 \rho A C_d \left(\frac{\omega_r}{K} \right)^2 R_{tire}^3 \right] \\ T_{MG1} \\ 0 \end{bmatrix} \quad (2.21)$$

Equation (2.21) relates the torques and forces with the angular accelerations of the three power sources. Differential equations can then be obtained by inverting the matrix. Although there are four equations, one of them shows the speed relations and one tracks the internal force F which can be eliminated. Therefore, there are only two state variables for the mechanical path.

On the electrical path, the dynamics can be represented by the SOC of the battery. Based on Equations (2.11), (2.12), and (2.14), we have

$$\dot{SOC} = - \frac{V_{oc} - \sqrt{V_{oc}^2 - 4(T_{MG1} \omega_{MG1} \eta_{MG1}^k \eta_{c1}^k + T_{MG2} \omega_{MG2} \eta_{MG2}^k \eta_{c2}^k) R_{batt}}}{2R_{batt} Q_{max}} \quad (2.22)$$

which, together with Equation (2.21), provides a three-state model of the THS powertrain.

2.3.2. Model of a Dual-Mode Power-Split Powertrain (Allison Hybrid System)

In the modeling perspective, the difference of a dual-mode power-split system involves additional planetary gears and clutches compared to a single-mode system. The linkages between planetary gear sets provide different kinematic relationship between the

gear nodes. The gear shifting with clutches change these linkages into different modes. As an example, a dual-mode system with two planetary gears and two clutches (Holmes et al., 2003) are modeled in this section. Two different sets of dynamic equations are derived to represent the model in the two modes. Gear shifting between the two modes is modeled as switching between the two models.

Figure 2.13 shows the free body diagram of this dual-mode powertrain system mechanical path. The planetary gear (PG) sets are represented by two levers in the middle of the diagram. R_1, S_1 and R_2, S_2 represent the ring gear and sun gear radii of the PG1 and PG2, respectively. F_1 and F_2 represent the internal forces between the pinion gears and the sun gears or ring gears. There are two clutches (CL) in the system, shifting between the two modes is achieved by switching the engagement of the two clutches. The dynamic models of these two modes are derived separately in the following.

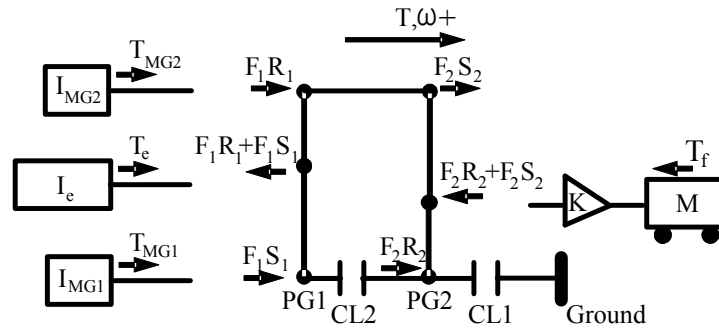


Figure 2.13: Free body diagram of the dual-mode powertrain.

In the input-split mode, CL1 is engaged and CL2 is released. The ring gear of PG2 is thus grounded. The speed constraint on PG2 then becomes

$$\omega_{e2}(R_2 + S_2) = \omega_{r2}R_2 \quad (2.23)$$

where ω_{c2} and ω_{r2} are the rotational speeds of the carrier gear and the ring gear of PG2.

PG1 satisfies the speed constraint

$$\omega_{c1}(R_1 + S_1) = \omega_{r1}R_1 + \omega_{s1}S_1 \quad (2.24)$$

where ω_{c1} , ω_{r1} , and ω_{s1} are the rotational speeds of the carrier gear, ring gear, and sun gear of PG1. By applying the Euler's Law for the ring gear node of PG1, carrier gear node of PG1, sun gear node of PG1, and carrier gear of PG2, respectively, we have

$$\dot{\omega}_{MG2}(I_{MG2} + I_{r1} + I_{s2}) = T_{MG2} + F_1 \cdot R_1 + F_2 \cdot S_2 \quad (2.25)$$

$$\dot{\omega}_e(I_e + I_{c1}) = T_e - F_1 \cdot (R_1 + S_1) \quad (2.26)$$

$$\dot{\omega}_{MG1}(I_{MG1} + I_{s1}) = T_{MG1} + F_1 \cdot R_1 \quad (2.27)$$

$$\dot{\omega}_{out}\left(\frac{R_{tire}^2}{K^2}m + I_{c2}\right) = -(F_2R_2 + F_2S_2) - \frac{1}{K}\left[T_{fb} - mgf_rR_{tire} - 0.5\rho AC_d\left(\frac{\omega_{out}}{K}\right)^2R_{tire}^3\right] \quad (2.28)$$

Here, similar to (2.19), Equation (2.28) includes only the longitudinal dynamics.

Combine (2.23)-(2.28) into a matrix form, we have

$$\begin{bmatrix}
I_e + I_{c1} & 0 & 0 & 0 & R_1 + S_1 & 0 \\
0 & \frac{R_{tire}^2}{K^2} m + I_{c2} & 0 & 0 & 0 & R_2 + S_2 \\
0 & 0 & I_{MG1} + I_{s1} & 0 & -S_1 & 0 \\
0 & 0 & 0 & I_{MG2} + I_{r1} + I_{s2} & -R_1 & -S_2 \\
R_1 + S_1 & 0 & -S_1 & -R_1 & 0 & 0 \\
0 & R_2 + S_2 & 0 & -S_2 & 0 & 0
\end{bmatrix}
\begin{bmatrix}
\dot{\omega}_e \\
\dot{\omega}_{out} \\
\dot{\omega}_{MG1} \\
\dot{\omega}_{MG2} \\
F_1 \\
F_2
\end{bmatrix}
=
\begin{bmatrix}
T_e \\
-\frac{1}{K} \left[T_{fb} + mgf_r R_{tire} + 0.5 \rho A C_d \left(\frac{\omega_{c2}}{K} \right)^2 R_{tire}^3 \right] \\
T_{MG1} \\
T_{MG2} \\
0 \\
0
\end{bmatrix}
\quad (2.29)$$

where the first four rows are from Equations (2.25) to (2.28) and the last two rows represent the speed constraints of the two planetary gears. The dynamics of the engine ω_e , electric machines ω_{MG1} and ω_{MG2} , and output carrier gear speed ω_{out} (which is proportional to the vehicle speed ω_{wh} by a factor of final drive ratio K) can be governed by

$$\begin{bmatrix}
\dot{\omega}_e \\
\dot{\omega}_{out} \\
\dot{\omega}_{MG1} \\
\dot{\omega}_{MG2} \\
F_1 \\
F_2
\end{bmatrix}
=
\begin{bmatrix}
I_e + I_{c1} & 0 & 0 & 0 & R_1 + S_1 & 0 \\
0 & \frac{R_{tire}^2}{K^2} m + I_{c2} & 0 & 0 & 0 & R_2 + S_2 \\
0 & 0 & I_{MG1} + I_{s1} & 0 & -S_1 & 0 \\
0 & 0 & 0 & I_{MG2} + I_{r1} + I_{s2} & -R_1 & -S_2 \\
R_1 + S_1 & 0 & -S_1 & -R_1 & 0 & 0 \\
0 & R_2 + S_2 & 0 & -S_2 & 0 & 0
\end{bmatrix}^{-1}
\begin{bmatrix}
T_e \\
-\frac{1}{K} \left[T_{fb} + mgf_r R_{tire} + 0.5 \rho A C_d \left(\frac{\omega_{c2}}{K} \right)^2 R_{tire}^3 \right] \\
T_{MG1} \\
T_{MG2} \\
0 \\
0
\end{bmatrix}
\quad (2.30)$$

In the compound-split mode, the clutch CL2 is locked and CL1 is released. The ring gear of PG2 rotates at the same speed as the sun gear of PG1. Follow a similar procedure the governing equations can be derived and the matrix equation is

$$\begin{bmatrix} \dot{\omega}_e \\ \dot{\omega}_{out} \\ \dot{\omega}_{MG1} \\ \dot{\omega}_{MG2} \\ F_1 \\ F_2 \end{bmatrix} = \begin{bmatrix} I_e + I_{c1} & 0 & 0 & 0 & R_1 + S_1 & 0 \\ 0 & \frac{R_{tire}^2}{K^2} m + I_{c2} & 0 & 0 & 0 & R_2 + S_2 \\ 0 & 0 & I_{MG1} + I_{s1} + I_{r2} & 0 & -S_1 & -R_2 \\ 0 & 0 & 0 & I_{MG2} + I_{r1} + I_{s2} & -R_1 & -S_2 \\ R_1 + S_1 & 0 & -S_1 & -R_1 & 0 & 0 \\ 0 & R_2 + S_2 & -R_2 & -S_2 & 0 & 0 \end{bmatrix}^{-1} \quad (2.31)$$

$$\begin{bmatrix} T_e \\ -\frac{1}{K} \left[T_{fb} + mgf_r R_{tire} + 0.5 \rho A C_d \left(\frac{\omega_{c2}}{K} \right)^2 R_{tire}^3 \right] \\ T_{MG1} \\ T_{MG2} \\ 0 \\ 0 \end{bmatrix}$$

Equation (2.30) and (2.31) present the powertrain system dynamics of the two operating modes. These two operating modes can be switched between one to another by a controlled synchronizing clutch shifting (Holmes et al., 2003). The synchronizing or “stepless” clutch shifting operation is possible by controlling the speeds of the electric machines. This mode shifting process is demonstrated in Figure 2.14. The planetary gear connections are displayed on the left hand side and the speeds of the other components are highlighted on the right hand side. At low speeds (Case a-c in Figure 2.14), the powertrain is in one operating mode, CL1 is locked to the ground. The speed of MG2 is thus proportional to the output vehicle speed. By controlling the speed of MG1, the engine speed remains close to the optimal point (assume constant in this demonstration). As the vehicle speed goes up and reaches a threshold, the sun gear of PG1 along with MG1 slows down to zero speed (Case c-d in Figure 2.14). At this point, CL2 can be

engaged and CL1 can be released simultaneously. This leads to the second operating speed mode. Since the mechanical linkage of the gear sets are changed, the new speed constraints allow MG1 to operate at the same speed range but with the vehicle speed at a higher level (Case d-f in Figure 2.14). The engine speed is controlled to maintain a constant speed through out this process despite the fact the vehicle speed increases from zero to a much higher speed.

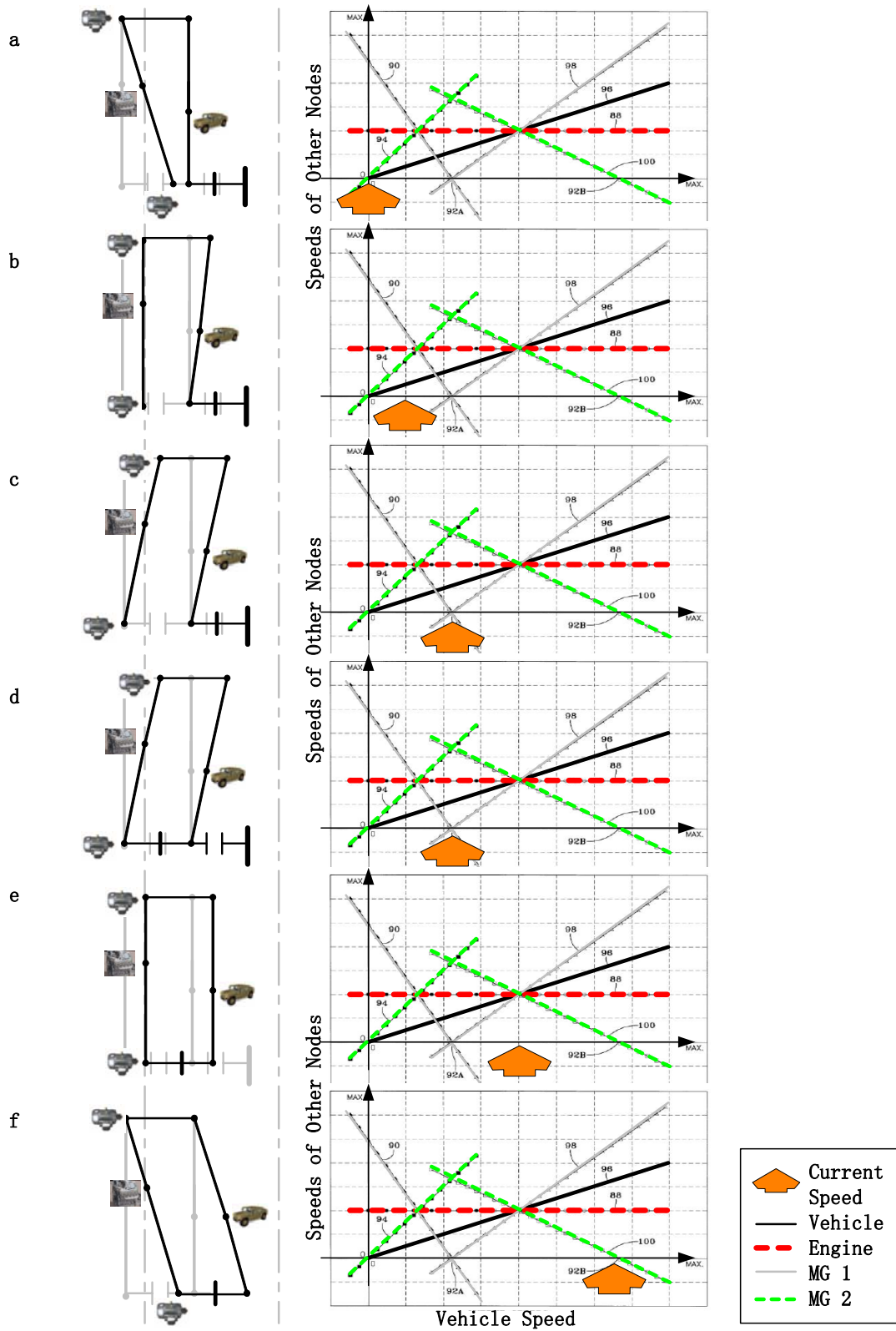


Figure 2.14: The synchronized mode shifting of the dual-mode power-split powertrain (The engine speed is assumed constant).

Based on this mode-shifting process, if we ignore the dynamics during gear shifts, up-shift and down-shift are treated as nothing but switching between the two models. As shown in Figure 2.15, when the controller commands to switch modes, simulation outputs are switched from one model block to the other.

Although the mechanical path of this dual-mode powertrain is very different from the single-mode system, the battery dynamics stay the same. As a result, Equation (2.22) still applies to this dual-mode powertrain system. This fact simplifies the design searches introduced in the later chapters.

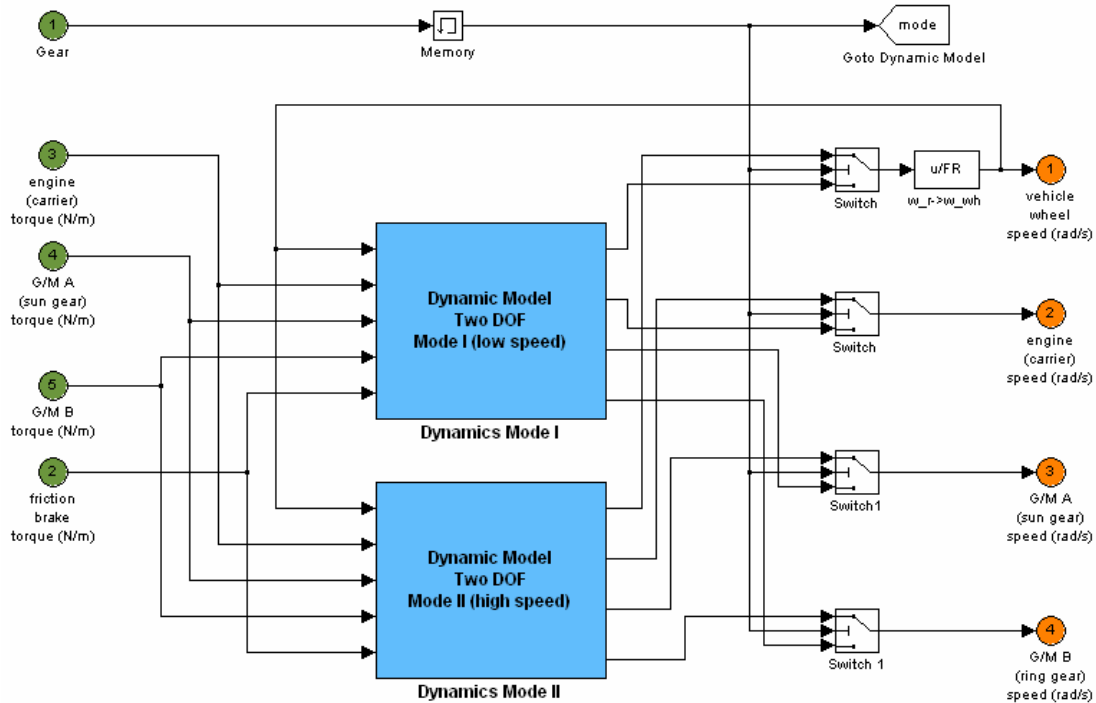


Figure 2.15: Simulink model for a dual-mode power-split powertrain.

2.4. Validation of the Powertrain Dynamic Model

The experimental results found in the literature are used to validate the vehicle systems constructed in this chapter. To achieve this validation, the same control logic from the real vehicle needs to be considered and implemented in the simulation. Hermance (1999) presented the basic idea of the rule-based control logic of the THS system. The next paragraphs describe a rule-based control strategy following these references to approximate the control law used in the THS.

As shown in Figure 2.16, the driving forces can be provided by MG2 and/or the engine. When the power demand is low, the vehicle speed is low, and battery SOC is sufficiently high, MG2 works alone to drive the vehicle. When the power demand is high, or the battery SOC is too low, the engine will start to supply the power. MG1 cooperates with MG2 to help start the engine. Within the engine operating range, the engine power is split through the planetary gear system. Part of the power goes to the vehicle driving axle through the ring gear. The rest drives the MG1 to charge the battery and/or directly supply power to MG2. As the power demand keeps increasing, the engine might be forced to operate outside of its efficient range. In those cases, MG2 can provide assistant power so that the engine efficiency remains high (assuming adequate battery SOC).

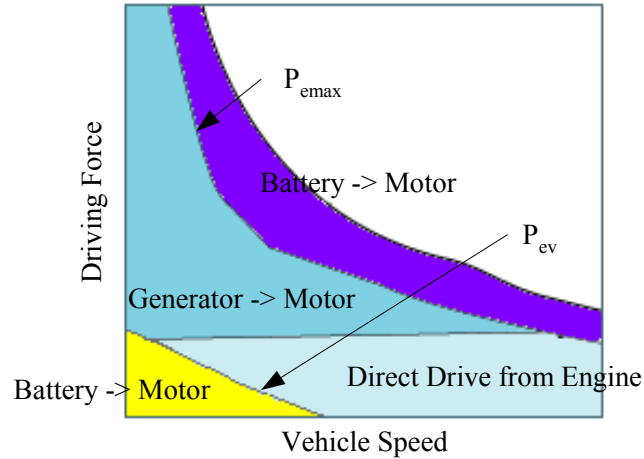


Figure 2.16: Power distribution of the Toyota Hybrid System (Hermance, 1999).

When the vehicle decelerates, the regenerative control system commands the MG2 to operate as a generator to recharge the battery. The friction brake is used whenever the requested braking power exceeds the capability of the MG2 or the battery. The engine and other components in the THS are set to free-rolling. Table 2.1 summarizes the ideas discussed above.

Table 2.1: Rule-based THS powertrain control strategy.

Conditions	Engine	MG2	MG1
$P_d < 0$ (braking)	0	$Max(P_d, P_{mmax})$	0
$P_d < P_{ev}$ w/o Charging	0	P_d	0
$P_{ev} < P_d < P_{emax}$ or Charging	$P_d(+P_{ch})$	P_g	$P_e - P_r$
$P_d > P_{emax}$	P_{emax}	$P_g + P_{batt}$	$P_e - P_r$

The power transfer efficiency is not shown in this table.

P_d = driver demand power, P_{mmax} = motor regenerative maximum power, $P_{ev} = 12$ kW, electric launching boundary power, P_{ch} = battery charging demand power, P_g = generated power, P_r = power transferred from

engine to the ring gear, P_e = engine output power, $P_{emax} = 40$ kW, maximum engine output power, P_{batt} = battery output power.

Figure 2.17 compares the simulation results with the experiment results from (Duoba et al., 2001). Considering the fact that we do not know precisely the control gains, and considering all the simplifying assumptions we made, the behavior of this model was found to agree with the actual system quite well.

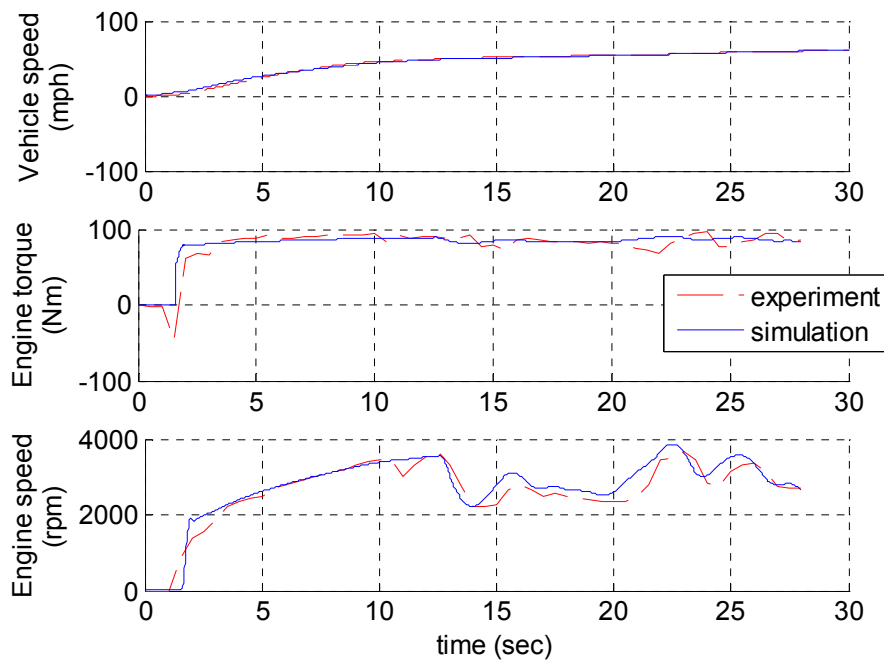
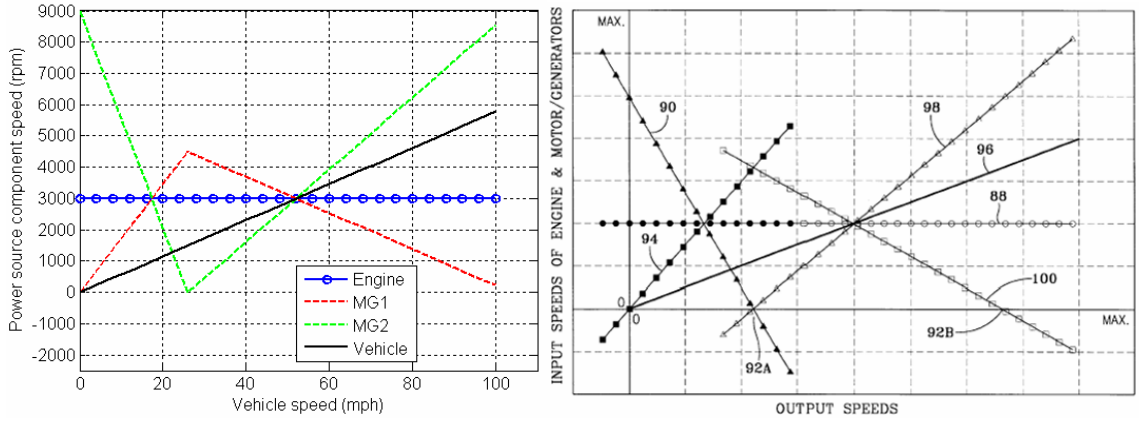


Figure 2.17: THS Engine simulation results compared with published experiment results (Duoba et al., 2001) under the same driving cycle.

There is no experimental data published on the dual-mode power-split Allison hybrid system in the literature. And the specifications for the GM hybrid vehicles are not yet available either. This makes it difficult for us to validate the dual-mode power-split powertrain model. Here we run the model in simulation to study the component speeds and compare the results to the conceptual plot from (Holmes et al., 2003). In this

simulation, the engine speed is kept constant under increased vehicle speed. The speeds of the two electric machines match the results from the reference (See Figure 2.18).



(a)

(b)

Figure 2.18: AHS powertrain simulation results (a) compared with published patent results (b) (Holmes et al., 2003).

CHAPTER 3

AUTOMATED MODELING OF POWER-SPLIT HYBRID VEHICLES

The powertrains described in Chapter 2 present just two examples of the many possible designs for power-split HEVs. Powertrain configurations with different gear-to-engine, gear-to-MG, and gear-to-clutch connections can be found in the literature (Schmidt, 1996; Holmes and Schmidt, 2002; Holmes et al., 2003; Ai and Mohr, 2005; Raghavan et al., 2007). The manual powertrain model development process, as presented in Chapter 2, can be applied to these powertrain designs. But to explore a large number of configurations, this process becomes tedious. Mistakes frequently happen in hand derivation process, especially wrong sign conventions or erroneous use of gear teeth numbers.

In this chapter, the powertrain model developed in Chapter 2 is further generalized and a universal format is introduced. Applying this new concept, derivation of dynamic models can be simplified and automated. This allows a large number of configuration designs to be analyzed and simulated. Furthermore, this math-based model can be used to systematically evaluate many vehicle performances (e.g., mode shifting, transmission efficiency, etc.) with the design requirements. Valuable design solutions can be then generated automatically. The detail process is explained in the next chapter.

3.1. The Universal Format of the Model Matrix

First, let's revisit Equation (2.29) from Chapter 2. The matrix constructed from the dynamic equations on the left relates the input torques to the rotational accelerations of gears and the power sources. This matrix is symmetric and can be divided into four sub-matrices as

$$\begin{bmatrix} I_e + I_{c1} & 0 & 0 & 0 & R_1 + S_1 & 0 \\ 0 & \frac{R_{tire}^2}{K^2} m + I_{c2} & 0 & 0 & 0 & R_2 + S_2 \\ 0 & 0 & I_{MG1} + I_{s1} & 0 & -S_1 & 0 \\ 0 & 0 & 0 & I_{MG2} + I_{r1} + I_{s2} & -R_1 & -S_2 \\ R_1 + S_1 & 0 & -S_1 & -R_1 & 0 & 0 \\ 0 & R_2 + S_2 & 0 & -S_2 & 0 & 0 \end{bmatrix} = \begin{bmatrix} J & D \\ D^T & 0 \end{bmatrix} \quad (3.1)$$

where J is a diagonal matrix that presents the inertia on each gear node; transpose matrices D and D^T show the gear train connections of the powertrain. Forced by these gear train connections, the geometric constraints affect both the torque and speed on each gear node. D relates the node torques and D^T relates the node speeds. Now (2.29) can be represented as

$$\begin{bmatrix} J & D \\ D^T & 0 \end{bmatrix} \begin{bmatrix} \dot{\Omega} \\ F \end{bmatrix} = \begin{bmatrix} T \\ 0 \end{bmatrix} \quad (3.2)$$

where Ω and T are the speed and torque vectors of the four nodes that connect to the engine, MG1, MG2, and vehicle. By introducing a matrix E calculated from J and D

$$E = J^{-1/2} D \quad (3.3)$$

The dynamic equation (2.30) can be derived as

$$\dot{\Omega} = J^{-1/2} \left(I - E(E^T E)^{-1} E^T \right) J^{-1/2} T \quad (3.4)$$

Equation (3.4) is the key dynamic equations with the universal format. The detailed derivation of it is explained as follows.

Equation (3.2) can be further simplified by eliminating the internal forces and obtaining an equation that shows the relationship only between the input torques T and the speeds Ω . First Equation (3.2) can be rewritten as

$$\begin{bmatrix} J^{-1/2} & 0 \\ 0 & I \end{bmatrix} \begin{bmatrix} J & D \\ D^T & 0 \end{bmatrix} \begin{bmatrix} J^{-1/2} & 0 \\ 0 & I \end{bmatrix} \begin{bmatrix} J^{1/2} & 0 \\ 0 & I \end{bmatrix} \begin{bmatrix} \dot{\Omega} \\ F \end{bmatrix} = \begin{bmatrix} J^{-1/2} & 0 \\ 0 & I \end{bmatrix} \begin{bmatrix} T \\ 0 \end{bmatrix} \quad (3.5)$$

which can be simplified to

$$\begin{bmatrix} I & J^{-1/2}D \\ (J^{-1/2}D)^T & 0 \end{bmatrix} \begin{bmatrix} J^{1/2}\dot{\Omega} \\ F \end{bmatrix} = \begin{bmatrix} J^{-1/2}T \\ 0 \end{bmatrix} \quad (3.6)$$

Define $E = J^{-1/2}D$, $\dot{\bar{\Omega}} = J^{1/2}\dot{\Omega}$, and $\bar{T} = J^{-1/2}T$, Equation (3.6) becomes

$$\begin{bmatrix} I & E \\ E^T & 0 \end{bmatrix} \begin{bmatrix} \dot{\bar{\Omega}} \\ F \end{bmatrix} = \begin{bmatrix} \bar{T} \\ 0 \end{bmatrix} \quad (3.7)$$

Denote the inverse matrix

$$\begin{bmatrix} I & E \\ E^T & 0 \end{bmatrix}^{-1} \equiv \begin{bmatrix} A & B \\ B^T & C \end{bmatrix} \quad (3.8)$$

Then the unknown sub-matrices can be solved from

$$\begin{bmatrix} A & B \\ B^T & C \end{bmatrix} \begin{bmatrix} I & E \\ E^T & 0 \end{bmatrix} = \begin{bmatrix} I & 0 \\ 0 & I \end{bmatrix} \quad (3.9)$$

Or equivalently, from the following four equations

$$AI + BE^T = I \quad (3.10)$$

$$AE = 0 \quad (3.11)$$

$$B^T I + CE^T = 0 \quad (3.12)$$

$$B^T E = I \quad (3.13)$$

From (3.12), $B^T = -CE^T$. Plug in to (3.13) we have

$$C = -(E^T E)^{-1} \quad (3.14)$$

where the non-singularity property of $E^T E$ is used. The sub-matrix C is then substituted into (3.12). From (3.10), (3.12), and (3.14), we obtain

$$A = I - E(E^T E)^{-1} E^T \quad (3.15)$$

Finally, factor the square root of J terms out from \bar{T} and $\dot{\bar{\Omega}}$. We obtain the relationship

$$\dot{\bar{\Omega}} = J^{-1/2} A J^{-1/2} T \quad (3.16)$$

which is equivalent to (3.4).

By introducing the universal model of the power-split powertrains, the modeling process now only requires the knowledge of kinematic connections (matrix D) and component inertia (matrix J). This enables an automated procedure to quickly translate the complex powertrain designs to dynamic models.

3.2. Automated Modeling Process

In this section, construction rules will be defined on how to generate matrix D and matrix J based on the powertrain design. The dynamic model obtained from this process makes the following assumptions. Only the vehicle longitudinal dynamics are considered; There is no energy lost between the gear force transmission; The clutch engagement dynamics (if a clutch exists in the system) are ignored and the synchronizing shifting operation between different mode is achieved by switching between different models (Holmes et al, 2003; Grewe et al., 2007); The studied powertrain configuration only consists of one engine, two MGs, and one vehicle output shaft.

Step 1: Determine the kinematic constraint matrix D

Matrix D contains the information of the kinematic constraints. Based on the powertrain system configuration, one can apply the following rules to obtain matrix D .

Rule 1: The number of columns of D is equal to the number of planetary gears.

Rule 2: The number of rows of D is equal to the number of columns of D plus two, each representing a node on the lever diagram.

It can be observed that for a single planetary gear (PG) in a power-split vehicle, three nodes are open to be connected. For a 2-PG set, although there are six gear nodes in total, a valid power-split design requires both PG to have two of their gear nodes connected. Here “connected” means a node is either connected to another node on the other PG, or to the ground. Therefore, the gear system has only two degrees of freedom (DOF). In other words, given any two speeds of any two nodes of the system, the speeds of all the other nodes are determined by the kinematic relations. This fact applies to three or more PG sets as well. Adding another PG increases one more node but the system still

has only two DOF. Since the row of the matrix D represents the nodes of the combined lever system, it is equal to the numbers of PGs plus two.

Rule 3: For the power source component(s) at each row, a “node coefficient” should be entered. The “node coefficient” is equal to: $-S_i$ if connected to the sun gear; $-R_i$ if connected to the ring gear; and R_i+S_i if connected to the carrier gear. Here the subscript i represents the corresponding planetary gear set.

Rule 4: Fill all other entries in matrix D with zeros.

Rule 5: For 3 or more PGs system, after the original matrix D is obtained. It needs to be further simplified to a 4×2 matrix to construct the dynamic model. This is done by using the kinematic relations derived from the free-rolling node(s) that is not connected to any power source or vehicle.

The process of rule 5 will be demonstrated in sections 3.3.2 and 3.3.3.

Step 2: Determine the inertia matrix J

Matrix J is a diagonal 4×4 square matrix. The entry of each diagonal term is equal to the inertia of each node. The node inertia is equal to the inertia of the power components. The inertias are I_e for the engine, I_{MG} for electric machines, and $\frac{mR_{tire}^2}{K^2}$ for the vehicle. Because the gear inertias are much smaller compared with the power sources and the vehicle, they can be ignored. Assume a convention that the first row of both matrix J and matrix D represents the engine node, the second row represents the output node connected to the vehicle, the third row represents the MG1 node, and the fourth row represents the MG2 node. The matrix J then has the format as in equation (3.17) for all configuration designs.

$$J = \begin{bmatrix} I_e & 0 & 0 & 0 \\ 0 & mR_{tire}^2 / K^2 & 0 & 0 \\ 0 & 0 & I_{MG1} & \\ 0 & 0 & 0 & I_{MG2} \end{bmatrix} \quad (3.17)$$

Step 3: Finalize the dynamic model

After the matrices D and J are determined, the dynamic model can be constructed by using (3.3) and (3.4). In (3.4), Ω consists of the speeds of engine ω_e , output shaft ω_{out} (proportional to the vehicle wheel speed ω_{wh} by a factor of final drive ratio $1/K$), and electric machine(s) ω_{MG} . T consists of the torques exerted at nodes corresponding to the respective Ω elements. For the output shaft, driving resistance torque from the vehicle $-\frac{1}{K} \left[T_{fb} + mgf_r R_{tire} + 0.5 \rho A C_d \left(\frac{\omega_{out}}{K} \right)^2 R_{tire}^3 \right]$ needs to be included. Finally, in addition to the mechanical path model, the electrical path model is generated using (2.22), while completes the dynamic model of the whole powertrain.

3.3. Automated Modeling Demonstration

Several examples are described in this section to demonstrate the automated modeling process. Some special cases are also studied to show the application of this modeling method.

3.3.1. A double planetary gear powertrain

A double-planetary power-split powertrain configuration (Ai and Anderson, 2005) is used as the first example to demonstrate the application of the automated-modeling process. This configuration, as shown in Figure 3.1, uses two planetary gear

sets. The engine is connected to the ring gear (R) of the PG1; the MG1 is connected to the sun gear (S) of the PG1; the MG2 is connected with the sun gear (S) of the PG2; the vehicle is connected with the carrier gear (C) of the PG2, which is also fixed with the carrier gear (C) of PG1. There are two clutches: CL1 is used for locking the ring gear of PG2 with the ground and CL2 is used for locking the ring gear of the PG2 and the sun gear of the PG1 together. Similar to the dual-mode powertrain we analyzed in the previous section, the powertrain system can operate in two different modes by switching between the two clutches.

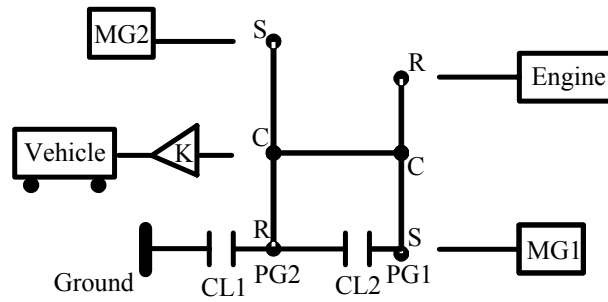


Figure 3.1: The powertrain of a double planetary gear system.

First, the mode with CL1 locked and CL2 released is modeled. Following the rules outlined in the previous section, because there are two planetary gears, the matrix D has two columns and four rows. The two columns represent the PG1 and PG2, respectively. As a convention, the nodes in Ω are the speeds of engine, vehicle, and then electric machine(s). Because the engine is connected to the ring gear of PG1, the element of the first row of the first column is $-R_1$. Because both PG1 and PG2 carrier gears are fixed together and connected to the output shaft to the vehicle wheel, R_1+S_1 is entered into the (2,1) element and R_2+S_2 is entered into the (2,2) element. Because MG1 is connected to the sun gear of PG1, $-S_1$ is entered into the (3,1) element of matrix D .

Because MG2 is connected to the sun gear of PG2, $-S_2$ is entered into the (4,2) element.

Finally, all the remaining matrix elements are filled with zeros. The D matrix is then

$$D_{mode1} = \begin{bmatrix} -R_1 & 0 \\ R_1 + S_1 & R_2 + S_2 \\ -S_1 & 0 \\ 0 & -S_2 \end{bmatrix}. \quad (3.18)$$

For the second mode, when CL1 is released and CL2 is locked, the only difference is that MG1 is connected to both the sun gear of PG1 and the ring gear of PG2. In this case, because the ring gear of PG2 is the new node to be connected with MG1, the element at the third row (the row has MG1) and the second column (the column represents the PG2) is a $-R_2$ instead of zero.

$$D_{mode2} = \begin{bmatrix} -R_1 & 0 \\ R_1 + S_1 & R_2 + S_2 \\ -S_1 & -R_2 \\ 0 & -S_2 \end{bmatrix}. \quad (3.19)$$

If given the assumption that the planetary gear set have much smaller gear inertia compare to the power source components. The inertia of engine, vehicle, MG1, and MG2 will be the four elements in the diagonal matrix J in (3.20) for this powertrain system no matter what driving modes are.

$$J = \begin{bmatrix} I_e & 0 & 0 & 0 \\ 0 & mR_{tire}^2 / K^2 & 0 & 0 \\ 0 & 0 & I_{MG1} & 0 \\ 0 & 0 & 0 & I_{MG2} \end{bmatrix} \quad (3.20)$$

Figure 3.2 demonstrates how this model generation process can be done with a graphic user interface in Matlab. On the left hand side, the design of the powertrain system can be specified by defining the connections between the gear node and power source components, and by defining the planetary gear gains. On the right hand side, a speed analysis figure can be generated immediately based on the automated model. As shown in this figure, assuming the engine speed is kept constant, the speeds of the two electric machines are functions of the vehicle speed. The same speed profiles were shown by Ai and Anderson (2005).

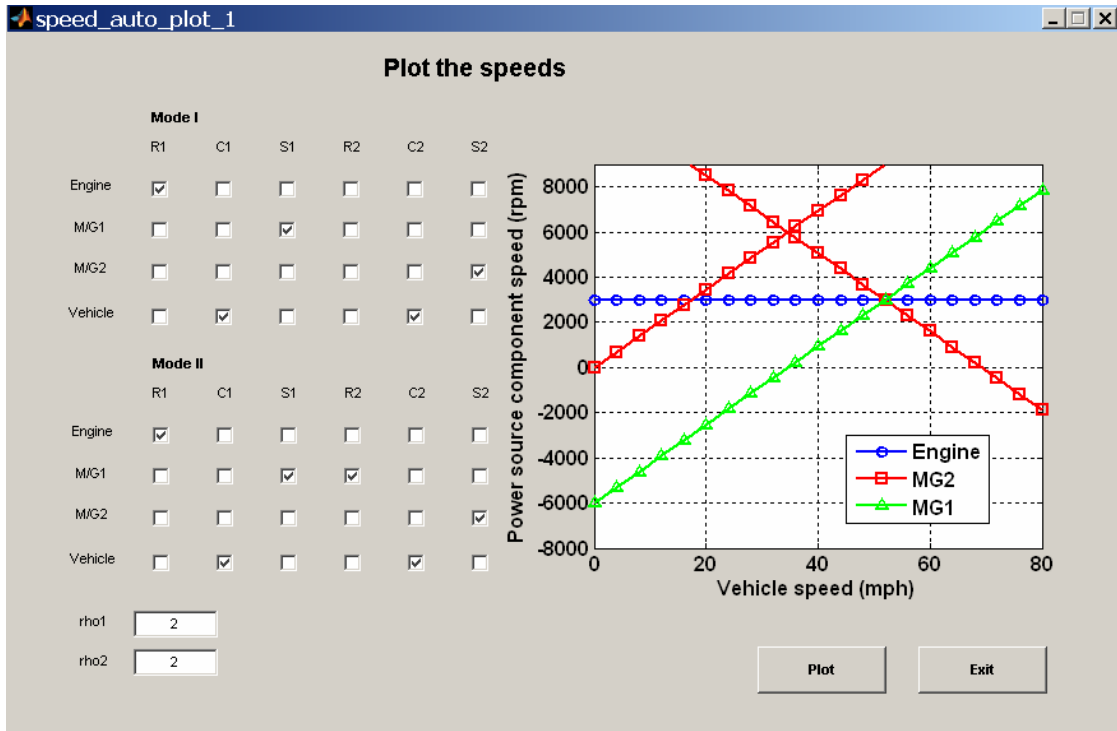


Figure 3.2: GUI for the model rapid generation, which shows speeds of the engine and electric machines as functions of vehicle speed.

3.3.2. A triple planetary gear powertrain

In this example, a three planetary gear (PG) powertrain (Schmidt, 1999) is selected to study the case with a free-rolling node. The additional PG brings the powertrain system one more free node, therefore, the matrix D is now a 5×3 matrix with the five rows correspond to the five nodes and three columns correspond to the three PGs. Except the one node connected to the vehicle final drive, there are apparently four nodes left that can be hooked up with engine and MGs. Because there are two MGs and one engine to be selected as the power sources, there is one node left without connecting to anything. This node is a free-rolling node. As a convention, the first row of matrix D is the node with engine, the second is the node with vehicle, the third and fourth are nodes with MGs, and the fifth row is the free-rolling node.

Figure 3.3 shows the powertrain design of this 3-PG powertrain system. In the low speed mode, the CL1 is locked and CL2 is released. The engine is connected to the ring gear of the PG1, therefore, a node coefficient $-R_1$ is entered into element (1,1). The vehicle final drive is connected to the carrier gear of the PG3, therefore, R_3+S_3 is entered into element (2,3). MG1 is connected to both ring gear of the PG2 and sun gear of the PG1, therefore, $-S_1$ is entered into element (3,1) and $-R_2$ is entered into element (3,2). MG2 is connected to both sun gears of the PG2 and PG3, therefore, $-S_2$ is entered into element (4,2) and $-S_3$ is entered into element (4,3).

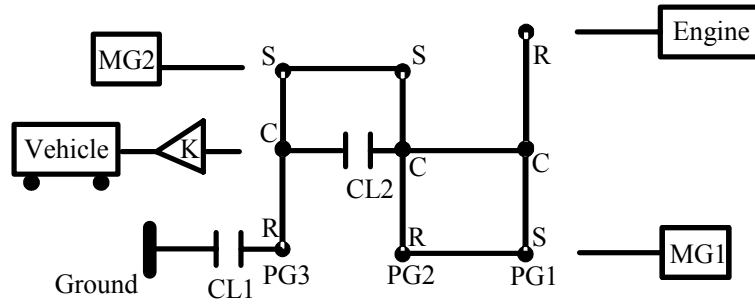


Figure 3.3: The powertrain of the triple planetary gear system in (Schmidt, 1999).

The fifth row of matrix D corresponds to the node/shaft of both carrier gears of the PG1 and PG2 where there is no power source connected. The corresponding node coefficients, in this case, R_1+S_1 is entered into element (5,1) and R_2+S_2 is entered into element (5,2). After filling the rest of the entries with zeros, the matrix D is generated as

$$D_{model} = \begin{bmatrix} -R_1 & 0 & 0 \\ 0 & 0 & R_3 + S_3 \\ -S_1 & -R_2 & 0 \\ 0 & -S_2 & -S_3 \\ R_1 + S_1 & R_2 + S_2 & 0 \end{bmatrix} \quad (3.21)$$

Following rule 5, this originally derived matrix D can be further simplified to a 4×2 matrix D to construct the dynamic model. In (3.21), the fifth row corresponds to the free-rolling node that is not connected to any power sources. Because the gear inertia on this node is ignored, the dynamics are

$$(R_1 + S_1)F_1 + (R_2 + S_2)F_2 = 0 \quad (3.22)$$

From (3.22),

$$F_2 = -\frac{(R_1 + S_1)}{(R_2 + S_2)}F_1 \quad (3.23)$$

Because in matrix D_{model} , the first and second columns consist of the node coefficients that multiply with F_1 and F_2 , respectively, relationship between these two forces in (3.23) can then be substituted to simplify the matrix D_{model} as

$$\bar{D}_{model} = \begin{bmatrix} -R_1 & 0 \\ 0 & R_3 + S_3 \\ -S_1 + \frac{R_1 + S_1}{R_2 + S_2} R_2 & 0 \\ \frac{R_1 + S_1}{R_2 + S_2} S_2 & -S_3 \end{bmatrix} \quad (3.24)$$

In the high speed mode, CL2 is locked and CL1 is released. Because of the change in gear linkage, the previous free-rolling carrier gear node is now connected to the vehicle final drive. The ring gear of the PG3, previously grounded by the CL1, becomes the free-rolling node. This means, now the fifth row of matrix D represents this node with $-R_3$ entered into column 3, row 5.

$$D_{mode2} = \begin{bmatrix} -R_1 & 0 & 0 \\ R_1 + S_1 & R_2 + S_2 & R_3 + S_3 \\ -S_1 & -R_2 & 0 \\ 0 & -S_2 & -S_3 \\ 0 & 0 & -R_3 \end{bmatrix} \quad (3.25)$$

Similarly as before, from the dynamics of the fifth row,

$$-R_3 F_3 = 0 \quad (3.26)$$

Therefore, $F_3=0$. The matrix D is then

$$\bar{D}_{mode2} = \begin{bmatrix} -R_1 & 0 \\ R_1 + S_1 & R_2 + S_2 \\ -S_1 & -R_2 \\ 0 & -S_2 \end{bmatrix} \quad (3.27)$$

In both modes, the matrix J represents the power source inertia on each node and has the same format as (3.17). This example demonstrates the process of modeling a 3-PG powertrain system. The extra free-rolling node is used to calculate the relationship between the internal forces and the derived relationship simplifies the matrix D to a 4×2 matrix.

3.3.3. A compound planetary gear powertrain

In this third and last example, a powertrain with a compound planetary gear (CPG) set is analyzed. A compound planetary gear set, also known as a Ravigneaux planetary gear, was invented by Ravigneaux (1953). Like a regular planetary gear set, it is commonly used in automatic transmissions to achieve different gear ratios. Some of the power-split HEV designs also implement such device for torque multiplication (Hermance and Abe, 2006).

As shown in Figure 3.4, the CPG consists of two tightly integrated planetary gear sets. The CPG set has two sun gears, a front sun and a rear sun, and a single carrier gear with two independent planetary gear wheels connected to it, an inner planet (short pinion gears) and an outer planet (long pinion gears). The carrier is one wheel but has two radii to couple with the inner and outer planets, respectively. The two planet gear sets rotate independently of the carrier but corotate with a fixed gear ratio with respect to each other. The inner planet couples with the front sun gear and corotates at a fixed gear ratio with

respect to it. The outer planet couples with the rear sun gear and corotates at a fixed gear ratio with respect to it. Finally, the ring gear also couples and corotates with the outer planet at a fixed gear ratio with respect to it. The CPG can be viewed as double PGs sharing the same carrier and ring gears. The kinematic constraints, therefore, can be presented by the following equations (Klages et al., 1997)

$$\omega_r R + \omega_{sr} S_r = \omega_c (R + S_r) \quad (3.28)$$

$$\omega_r R + \omega_{sf} (-S_f) = \omega_c [R + (-S_f)] \quad (3.29)$$

where S_r and S_f represent the rear sun gear and front sun gear radius, respectively. These two speed equations have similar format as a normal planetary gear in (2.1) except S_f has a minus sign due to the different gear linkage of the CPG. The automated modeling process can also be applied with $+S_f$ treated as the sun gear node coefficient of the front planetary gear set.

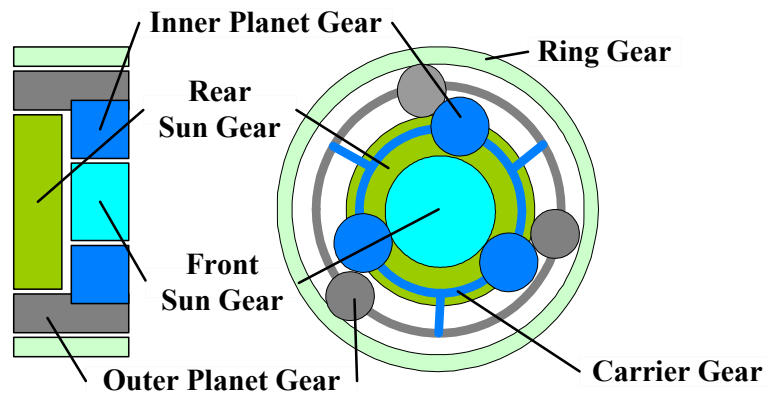


Figure 3.4: Composition of the compound planetary gear set.

The example powertrain with a CPG is chosen from the literature, which is designed for the Toyota Hybrid System for the Lexus GS450. The CPG is used to achieve different torque multiplication ratios for the motor by engaging grounding clutches

(Hermance and Abe, 2006). The lever diagram representation of the powertrain is shown in Figure 3.5. By considering the CPG as a double-PG with same ring and carrier, this powertrain system then becomes a 3-PG system. Similarly to example 2, when CL1 is locked and CL2 is released, the kinematic matrix D is

$$D_{model} = \begin{bmatrix} R_1 + S_1 & 0 & 0 \\ -R_1 & R_2 - S_f & R_2 + S_r \\ -S_1 & 0 & 0 \\ 0 & 0 & -S_r \\ 0 & +S_f & 0 \end{bmatrix} \quad (3.30)$$

where the first column of D represent the single PG connected with the engine and MG1, the second and third columns of D represent the double-PG of the CPG system. As the kinematic constraint in (3.29) differs from a regular PG with a negative sign on the sun gear radius, the corresponding node coefficient for S_f has an opposite sign (+) to regular case (-). Finally, as the front sun gear is the free-rolling node in this mode, following rule 5, the fifth row of matrix D is used to find

$$+S_f F_f = 0 \quad (3.31)$$

where F_f represents the internal force on the front sun gear. $F_f=0$. This is because of the assumption that we ignored the inertia of the front sun gear. The internal force on the front sun gear is hence small and can be omitted. The matrix D becomes

$$\bar{D}_{model} = \begin{bmatrix} R_1 + S_1 & 0 \\ -R_1 & R_2 + S_r \\ -S_1 & 0 \\ 0 & -S_r \end{bmatrix} \quad (3.32)$$

Similarly, when CL2 is locked and CL1 is released, the matrix D is generated as

$$D_{mode2} = \begin{bmatrix} R_1 + S_1 & 0 & 0 \\ -R_1 & R_2 - S_f & R_2 + S_r \\ -S_1 & 0 & 0 \\ 0 & 0 & -S_r \\ 0 & -R_2 & -R_2 \end{bmatrix} \quad (3.33)$$

From the fifth row (free-rolling node),

$$-R_2 F_f - R_2 F_r = 0 \quad (3.34)$$

therefore, $F_f = -F_r$. And the matrix D can be simplified as

$$\bar{D}_{mode2} = \begin{bmatrix} R_1 + S_1 & 0 \\ -R_1 & S_f + S_r \\ -S_1 & 0 \\ 0 & -S_r \end{bmatrix} \quad (3.35)$$

In both modes, matrix J is the same as (3.17). This example shows that the proposed modeling process can be extended to a system with compound planetary gear set(s) with some minor adjustment on the node coefficient.

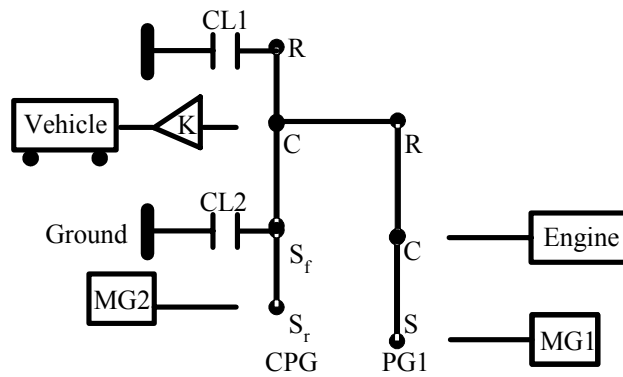








Figure 3.5: The powertrain of the compound PG system in (Hermance and Abe, 2006).

To conclude this Chapter, Table 3.1 summarized 6 popular power-split powertrain designs available in the literature. Their corresponding automated modeling matrix D are

also shown. This modeling process can be easily applied to possible configurations and allow us to systematically explore different designs.

Table 3.1: Matrix D for the popular power-split powertrain designs.

Vehicle	Design	Modeling Matrix D	
Toyota Hybrid System for Prius (Hermance, 1999)		$\begin{bmatrix} R_1 + S_1 \\ -R_1 \\ -S_1 \end{bmatrix}$	
Toyota Hybrid System for Highlander (Hermance and Abe, 2006)		$\begin{bmatrix} R_1 + S_1 & 0 \\ -R_1 & -R_2 \\ -S_1 & 0 \\ 0 & -S_2 \end{bmatrix}$	
Toyota Hybrid System for Lexus GS450 (Hermance and Abe, 2006)		$\begin{bmatrix} R_1 + S_1 & 0 \\ -R_1 & R_2 + S_r \\ -S_1 & 0 \\ 0 & -S_r \end{bmatrix}$	$\begin{bmatrix} R_1 + S_1 & 0 \\ -R_1 & S_f + S_r \\ -S_1 & 0 \\ 0 & -S_r \end{bmatrix}$
GM 2-PG Hybrid System (Holmes et al. 2003)		$\begin{bmatrix} R_1 + S_1 & 0 \\ 0 & R_2 + S_2 \\ -S_1 & 0 \\ -R_1 & -S_2 \end{bmatrix}$	$\begin{bmatrix} R_1 + S_1 & 0 \\ 0 & R_2 + S_2 \\ -S_1 & -R_2 \\ -R_1 & -S_2 \end{bmatrix}$
Timken Two Mode Hybrid System (Ai and Mohr, 2004)		$\begin{bmatrix} -R_1 & 0 \\ R_1 + S_1 & R_2 + S_2 \\ -S_1 & 0 \\ 0 & -S_2 \end{bmatrix}$	$\begin{bmatrix} -R_1 & 0 \\ R_1 + S_1 & R_2 + S_2 \\ -S_1 & -R_2 \\ 0 & -S_2 \end{bmatrix}$
GM 3-PG Hybrid System (Schmidt, 1999)		$\begin{bmatrix} -R_1 & 0 \\ 0 & R_3 + S_3 \\ -S_1 + \frac{R_1 + S_1}{R_2 + S_2} R_2 & 0 \\ \frac{R_1 + S_1}{R_2 + S_2} S_2 & -S_3 \end{bmatrix}$	$\begin{bmatrix} -R_1 & 0 \\ R_1 + S_1 & R_2 + S_2 \\ -S_1 & -R_2 \\ 0 & -S_2 \end{bmatrix}$

CHAPTER 4

CONFIGURATION SCREENING OF POWER-SPLIT HYBRID VEHICLES

The modeling process proposed in Chapter 3 helps the powertrain designers to quickly explore different configurations. Because each generated model represents a specific configuration, the automated modeling process can be used to systematically search possible design candidates and evaluate their performance. This enables the powertrain designers to study all possible designs and to quickly focus on a few high-potential candidates. In this chapter, a configuration screening process is suggested for the power-split powertrain design.

Before introducing the configuration screening process, it is important to first define what the design objectives are. These design objectives will be used in the screening process to eliminate invalid designs as well as to rank valid candidates. For example, drivability, engine efficiency, fuel consumption, emission, noise, electric machine efficiency, battery efficiency, battery life, etc. can be selected as design objectives. Another possibility is to impose vehicle performance objectives as inequality constraints while solving an optimization problem to minimize vehicle cost. The vehicle cost can include the cost of components, accessories, maintenance, etc. It is very difficult to tackle all these issues simultaneously because the model will have to be very comprehensive to predict all these factors accurately. Therefore, typically only a small set of performances and/or cost factors are considered. The design objectives to be

considered in this dissertation include feasible gear connection, sizing of power sources, vehicle drivability, feasible transmission configuration, and transmission efficiency. They are all major issues of power-split hybrid vehicle performance.

The transmission studied in this chapter is limited to have 2 planetary gears (PG). This is because on one hand, design with a single planetary gear does not provide a large number of configurations to make the study interesting. On the other hand, designs with 3 or more planetary gears become excessively complex and the number of possible configurations is very large.

In Chapter 2, we developed the dynamic model for a dual-mode super-sized HMMWV with a specific 2-PG powertrain. But the question of whether the specified configuration is optimal for the vehicle is not yet answered. In this Chapter, The configuration screening of the 2-PG dual-mode system is to be processed for the super-size HMMWV as a case study. The proposed design process is under the following assumptions. Firstly, the vehicle is assumed to be partially designed with the engine, vehicle body, and final drive already given (Table 4.1). Secondly, the two electric machines are limited to have a total power of 60 kW and the battery is assumed to be sized to take the maximum power to/from the electric machines. This electric power limit is selected to make sure only a handful of configurations provide feasible solutions. They also represent, very crudely, cost and packaging constraints. Finally, because the screening process suggested in this chapter focuses on the effect of different powertrain configurations, the design parameters on each configuration are assumed to be typical values. These parameters include: MG1 and MG2 both are sized as 30 kW; all planetary

gear gains (defined as the ring gear radius divided by the sun gear radius) are equal to 2. A more completed parametric design optimization is developed in the next chapter.

Table 4.1: Specifications for the super-size power-split hybrid HMMWV.

Parameters	Values
Air drag coefficient	0.3
Final drive ratio	3.9
Frontal area	3.58 m ²
Max engine power	180 kW
Rolling resistance coefficient	0.008
Total electric machines power	60 kW
Vehicle mass*	5112 kg
Wheel radius	0.287 m

* Vehicle mass excludes that of the electric machines and battery.

4.1. Physically Feasible Powertrain Configuration

There are three steps in the suggested configuration screening process, in which it checks the powertrain physical feasibility, drivability, and efficiency, respectively. In the first step of the configuration screening process, the dynamic models are automatically generated for all possible configurations. Those configurations that are not physically feasible will be screened out.

The automated dynamic model provides a one-to-one correspondence between the powertrain configuration and the model matrix. On one hand, given a configuration design, the corresponding kinematic matrix D can be derived using the rules presented in

Chapter 3. On the other hand, given a matrix D , the corresponding configuration is uniquely defined. For example, for the D matrix given in (4.1), the corresponding powertrain configuration can be derived as follows. The R_1+S_1 at the (1,1) element indicates that the engine connects to the carrier gear of PG1; $-R_1$ and R_2+S_2 at the (2,1) and (2,2) elements indicate that the output shaft connects to both the ring gear of PG1 and the carrier gear of PG2; $-S_1$ at the (3,1) element indicates the connection between MG1 and the sun gear of PG1; and $-R_2$ at the (4,2) element indicates the connection between MG2 and the ring gear of PG2. The absence of $-S_2$ in the second column indicates that the sun gear of PG2 is grounded. As a result, the configuration identified by this matrix D can be drawn in Figure 4.1. The fact that there is a one-on-one relationship between the matrix D and the configuration design makes a configuration screening process possible.

$$D = \begin{bmatrix} R_1 + S_1 & 0 \\ -R_1 & R_2 + S_2 \\ -S_1 & 0 \\ 0 & -R_2 \end{bmatrix} \quad (4.1)$$

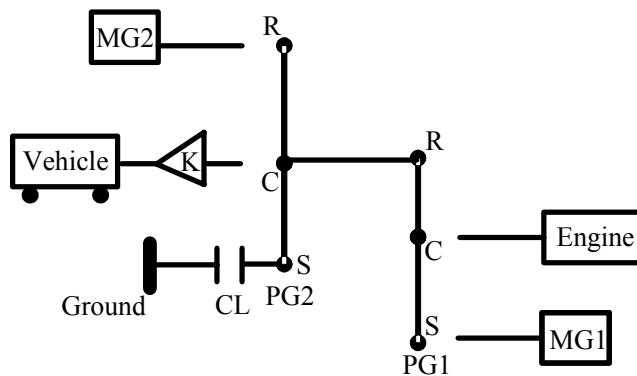


Figure 4.1: The powertrain configuration identified by the example D matrix in (4.1).

The task of constructing the dynamic model for a 2-PG powertrain system is equivalent to generating matrix J and matrix D . The matrix J of the powertrain is fixed as shown in equation (4.2) for all different configurations assuming the gear inertia can be ignored.

$$J = \begin{bmatrix} I_e & 0 & 0 & 0 \\ 0 & mR_{tire}^2 / K^2 & 0 & 0 \\ 0 & 0 & I_{MG1} & \\ 0 & 0 & 0 & I_{MG2} \end{bmatrix} \quad (4.2)$$

The matrix D of the desired 2-PG powertrain is a 4×2 matrix with the two columns representing the two PGs. In each column, a power-split PG (defined in section 2.2.1) has one zero and three node coefficients while a power-ratio PG (defined in section 2.2.1) has two zeros and any two of the three node coefficients. Therefore, for a single column in a matrix D , there could be 24 different combinations for a power-split PG,

$$P_4^4 = 4! = 24 \quad (4.3)$$

and there could be 36 different combinations for a power-ratio PG.

$$C_3^2 \cdot P_4^2 = 3 \times (4 \times 3) = 36 \quad (4.4)$$

A valid power-split configuration must consist of at least one power-split PG. And changing the order of the two columns in the matrix D does not change the configuration design. Therefore, the total design combinations can be calculated as

$$24 \times 24 / 2 + 24 \times 36 = 1152 \quad (4.5)$$

where the part before the plus sign calculates the number of combinations with two power-split PGs and the part after calculates the number of combinations with one

power-ratio PG and one power-split PG. There are 1152 different mathematical combinations in total for a two-PG power-split powertrain. This represents all mathematically possible designs of a 2-PG system.

Obviously, not all of these 1152 designs are physically feasible. The unfeasible configurations need to be screened out. The method of justifying the feasibility of the configuration is explained as follows. There are two types of configurations that are not feasible. The first type is when any row of the matrix D has two zeros, the power source/vehicle presented by that row is not connected to anything. Apparently this type of configuration is not feasible. The second type is when the configuration has the engine connected to the vehicle output directly (e.g., see Figure 4.2). There is no split power flowing to the vehicle through the electric machine. As a result, the design does not qualify as a power-split powertrain. Here note that in the automated modeling process, each node coefficient is entered only once if it appears. This guarantees that any two of the engine, MGs, and vehicle are not connected to the same gear node.

In both infeasible configuration types that described above, the powertrain system violates the fact that the power-split powertrain configuration need to have two degrees of freedom (DOF). In other words, given any two speeds of engine, vehicle, and the two MGs, the other two speeds can not be determined in an infeasible configuration. And obviously, if a powertrain configuration does not have two DOF, it can not be a feasible power-split system. Therefore, a configuration identified by matrix D is feasible for a power-split powertrain if and only if the gear system has two degrees of freedom (DOF).

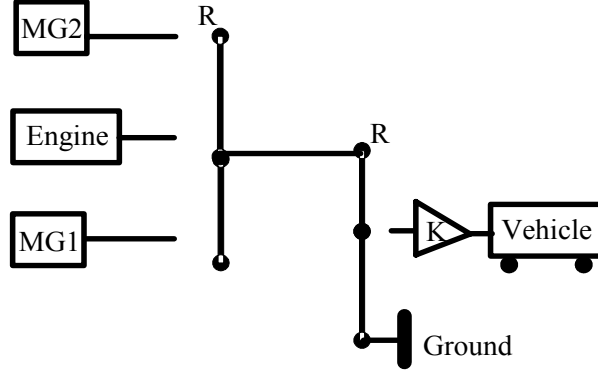


Figure 4.2: An unfeasible configuration that has the engine connected to the vehicle shaft.

Matrix D can be used to check if the powertrain configuration has two DOF and hence identify if the design is feasible or not. Recall in the matrix D , the first and second rows correspond to the speeds of the input and output nodes, respectively; while the third and fourth rows correspond to the speeds of the two MGs. Therefore, matrix D can be further divided into two sub-matrices

$$D = \begin{bmatrix} D_{11} & \dots \\ D_{21} & \dots \\ D_{31} & \dots \\ D_{41} & \dots \end{bmatrix} = \begin{bmatrix} D_{EV} \\ D_{MG} \end{bmatrix} \quad (4.6)$$

where D_{EV} is the first two rows and D_{MG} is the third and fourth rows. Substitute this new format of D into the original dynamic equation (3.2),

$$D^T \dot{\Omega} = D_{EV}^T \begin{bmatrix} \dot{\omega}_e \\ \dot{\omega}_{out} \end{bmatrix} + D_{MG}^T \begin{bmatrix} \dot{\omega}_{MG1} \\ \dot{\omega}_{MG2} \end{bmatrix} = 0 \quad (4.7)$$

which can be further derived to

$$\begin{bmatrix} \omega_{MG1} \\ \omega_{MG2} \end{bmatrix} = -D_{MG}^{-T} D_{EV}^T \begin{bmatrix} \omega_e \\ \omega_{out} \end{bmatrix} \quad (4.8)$$

or

$$\begin{bmatrix} \omega_e \\ \omega_{out} \end{bmatrix} = -D_{EV}^{-T} D_{MG}^T \begin{bmatrix} \omega_{MG1} \\ \omega_{MG2} \end{bmatrix} \quad (4.9)$$

From (4.8), the speeds of MGs can be calculated if and only if the sub-matrix D_{MG} has full rank. From (4.9), the speeds of engine and vehicle can be calculated if and only if the sub-matrix D_{EV} has full rank. Therefore, the matrices D_{EV} and D_{MG} must both have full ranks for the configuration to be feasible. After checking the ranks of D_{EV} and D_{MG} in the 1152 possible candidates, only 288 configurations remain for further consideration.

4.2. Drivability and Power Source Component Sizing

In the second step of the configuration screening process, the vehicle drivability and the electric machines sizing constraints are considered. The drivability is heavily dependent on the power and torque capabilities of the power sources. A typical design of a classical vehicle has the engine sized properly to meet drivability targets. The engine needs to supply enough power to accelerate the vehicle, reach a minimum speed on an uphill slope, or possess a minimum towing capability. For a power-split HEV, the drivability objective can be more easily achieved because the electric power sources and powertrain configuration provide additional power and/or design degree of freedom. But at the same time, the design problem becomes more complex because each component size needs to be optimized to coordinate seamlessly.

Compare to a conventional vehicle, the addition of electric machines brings extra cost, weight, volume, and accessories into the design problem. These factors result in additional design challenges, including cost, packaging, etc. According to the study

shown in Table 4.2, as the size (power) of the electric machines increases, additional cost, weight, and volume are incurred.

Table 4.2: Comparison of attributes and cost of three type of traction motors (Cuenca et al., 1999).

Attribute	AC-induction motor	DC-Series/Shunt motor	DC-brushless motor
Cost (\$/kW)	8.1	10.2	11.8
Mass (lb/kW)	1.7	2.7	1.65
Volume (in ³ /kW)	10.5	19.1	16.1

Different configurations of power-split HEVs affect the optimal sizes of the power sources. This is because different configurations result in different gear transmission ratios which affect the dynamics of each power sources. Therefore, an electric machine that works for one configuration may not work for another. Let's take a look at an example driving scenario in which the vehicle is running at the speed of 20 mph. If the driver demands 60 kW, the possible engine power and MG1 power can be searched and the MG2 torque input is then calculated to fulfill the power demand at every sampling time. The valid MG2 torque must satisfy

$$T_{MG2_min} \leq T_{MG2} \leq T_{MG2_max} \quad (4.10)$$

where T_{MG2_min} and T_{MG2_max} are the torque constraints. Figure 4.3 shows this searching result on a single-mode powertrain configuration (Toyota hybrid system), note the vehicle parameters are replaced by those of the HMMWV and the power sources are also changed accordingly. The MG2 size here is 30 kW and results show that all calculated

MG2 torques are outside of the constraints imposed by (4.10). This indicates the MG2 is too small to satisfy the drivability constraints. This problem can be solved by increasing the size of MG2 as shown in Figure 4.4. With a more powerful 90 kW electric machine (assume battery size is adjusted accordingly and it does not force constraints for the electric machine), the calculated MG2 torque, necessary to satisfy the drivability objective, falls within the constraints. If we change the configuration design to a 2-PG Allison hybrid system, because the gear ratio changes, for the same engine speed, the MG2 speed is lower than that of THS. Lower speed allows MG2 to produce higher torque. Therefore, even for a 30 kW MG, the calculated torque for MG2 could be feasible (See Figure 4.5).

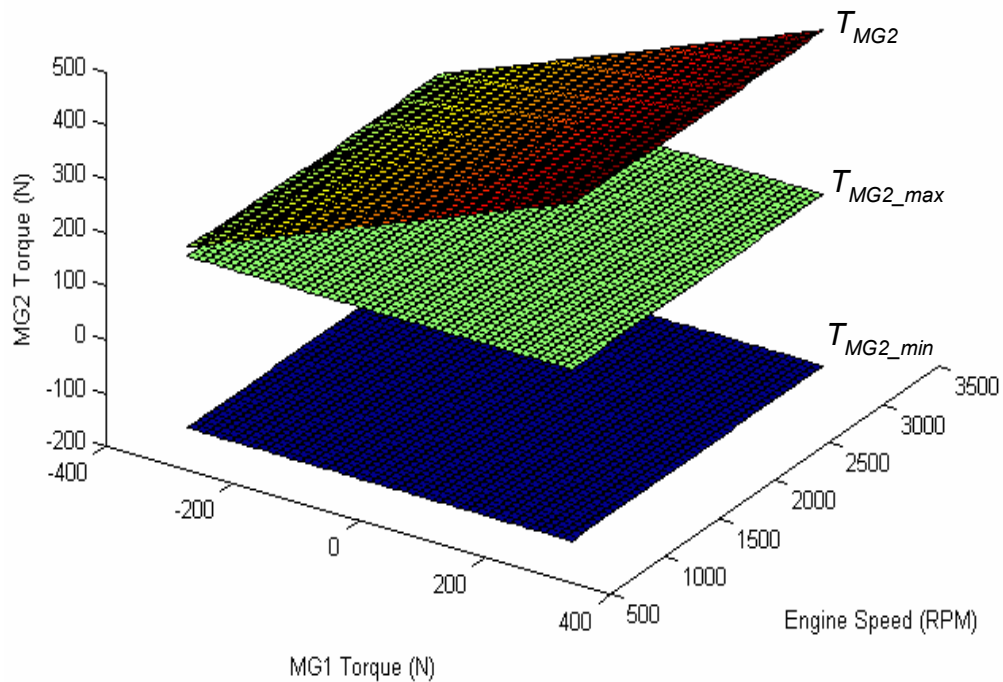


Figure 4.3: Torque values for a 30 kW MG2 in the THS configuration.

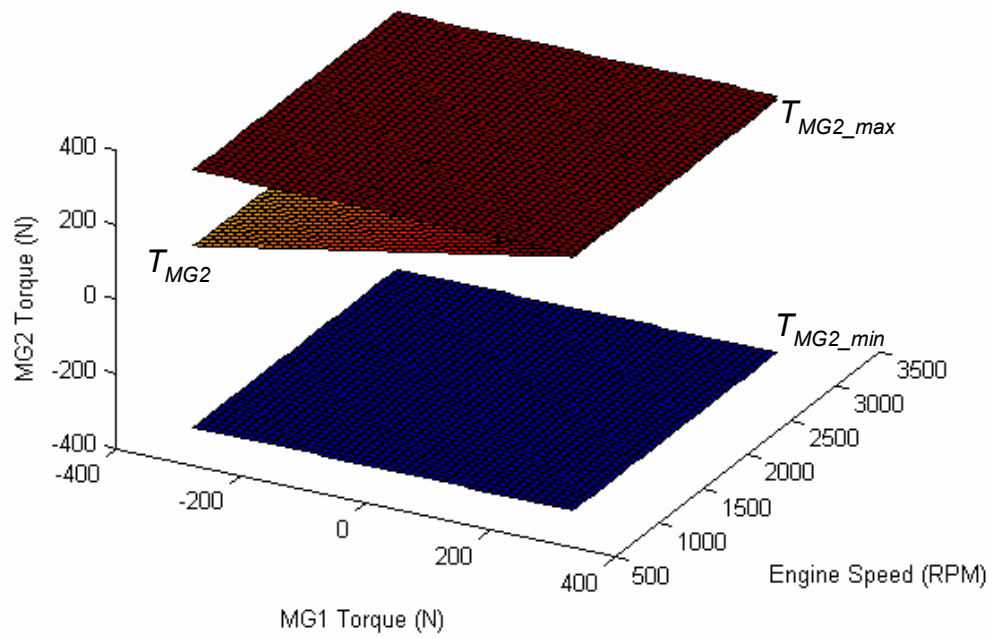


Figure 4.4: Torque values for a 90 kW MG2 in the THS configuration.

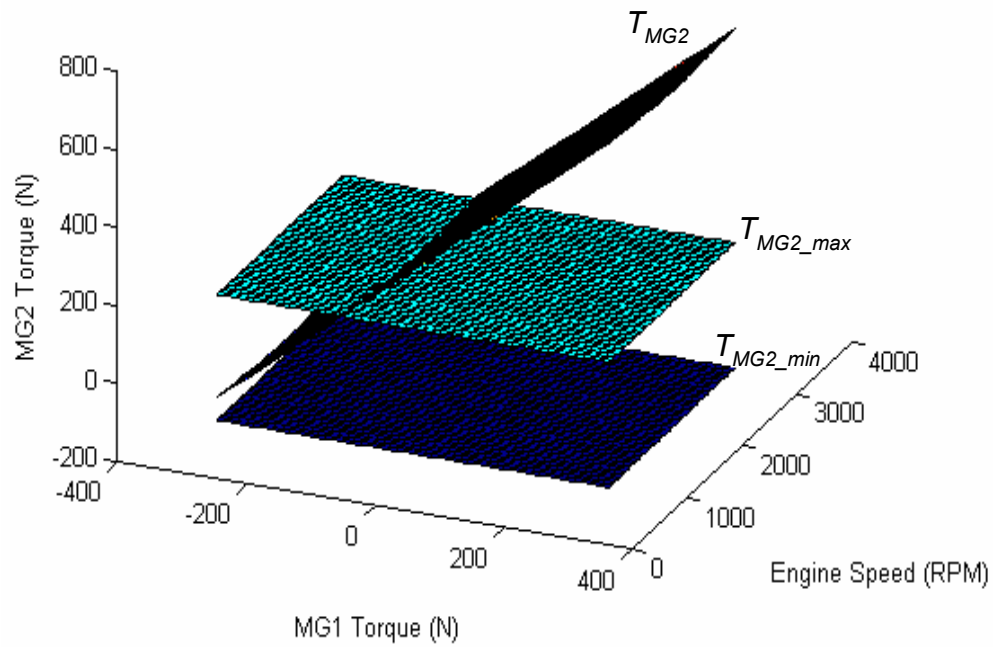


Figure 4.5: Torque values for a 30 kW MG2 in the 2-PG AHS configuration.

In this study, we assume that it is necessary to satisfy a drivability constraint: the powertrain needs to produce average power in excess of 100 kW to launch the vehicle from 0 to 50 mph in 15 seconds (Figure 4.6). At each sampling time, instead of using any control strategy to decide the power-split ratio, all possible power inputs from engine and electric machines are simulated and the following speed and torque constraints are checked.

$$\begin{aligned}
\omega_{e_min} &\leq \omega_e \leq \omega_{e_max} \\
\dot{\omega}_{e_min} &\leq \dot{\omega}_e \leq \dot{\omega}_{e_max} \\
\omega_{MG1_min} &\leq \omega_{MG1} \leq \omega_{MG1_max} \\
T_{MG1_min} &\leq T_{MG1} \leq T_{MG1_max} \\
\omega_{MG2_min} &\leq \omega_{MG2} \leq \omega_{MG2_max} \\
T_{MG2_min} &\leq T_{MG2} \leq T_{MG2_max}
\end{aligned} \tag{4.11}$$

If none of the input combinations in a powertrain configuration satisfies all these constraints, this configuration does not meet the power source drivability objective and is screened out. Notice that this step only provides necessary but not sufficient sizing limits for the powertrain system. It eliminates the designs that obviously violate the design objectives, but the remaining configuration candidates need to have further component sizing analysis, which will be explained in the next chapter. In the given example, after checking the drivability constraints, 17 configuration candidates are left, their matrices D are shown in (4.12).

$$\begin{aligned}
D_1 &= \begin{bmatrix} -R_1 & 0 \\ R_1+S_1 & R_2+S_2 \\ -S_1 & 0 \\ 0 & -R_2 \end{bmatrix} & D_2 &= \begin{bmatrix} -R_1 & 0 \\ 0 & R_2+S_2 \\ -S_1 & 0 \\ R_1+S_1 & -R_2 \end{bmatrix} & D_3 &= \begin{bmatrix} -R_1 & 0 \\ 0 & R_2+S_2 \\ R_1+S_1 & -S_2 \\ -S_1 & 0 \end{bmatrix} & D_4 &= \begin{bmatrix} -S_1 & 0 \\ R_1+S_1 & R_2+S_2 \\ 0 & -S_2 \\ -R_1 & 0 \end{bmatrix} & D_5 &= \begin{bmatrix} -S_1 & 0 \\ 0 & R_2+S_2 \\ R_1+S_1 & -S_2 \\ -R_1 & 0 \end{bmatrix} \\
D_6 &= \begin{bmatrix} R_1+S_1 & 0 \\ -R_1 & R_2+S_2 \\ -S_1 & 0 \\ 0 & -S_2 \end{bmatrix} & D_7 &= \begin{bmatrix} R_1+S_1 & 0 \\ 0 & R_2+S_2 \\ -R_1 & 0 \\ -S_1 & -S_2 \end{bmatrix} & D_8 &= \begin{bmatrix} R_1+S_1 & 0 \\ 0 & R_2+S_2 \\ -S_1 & 0 \\ -R_1 & -S_2 \end{bmatrix} & D_9 &= \begin{bmatrix} -R_1 & 0 \\ R_1+S_1 & R_2+S_2 \\ -S_1 & 0 \\ 0 & -S_2 \end{bmatrix} & D_{10} &= \begin{bmatrix} -R_1 & 0 \\ 0 & R_2+S_2 \\ -S_1 & 0 \\ R_1+S_1 & -S_2 \end{bmatrix} \\
D_{11} &= \begin{bmatrix} -S_1 & 0 \\ R_1+S_1 & R_2+S_2 \\ -R_1 & 0 \\ 0 & -S_2 \end{bmatrix} & D_{12} &= \begin{bmatrix} -S_1 & 0 \\ 0 & R_2+S_2 \\ R_1+S_1 & 0 \\ -R_1 & -S_2 \end{bmatrix} & D_{13} &= \begin{bmatrix} -S_1 & 0 \\ 0 & R_2+S_2 \\ -R_1 & 0 \\ R_1+S_1 & -S_2 \end{bmatrix} & D_{14} &= \begin{bmatrix} R_1+S_1 & 0 \\ 0 & R_2+S_2 \\ -S_1 & 0 \\ -R_1 & -S_2 \end{bmatrix} & D_{15} &= \begin{bmatrix} -R_1 & 0 \\ R_1+S_1 & -R_2 \\ -S_1 & 0 \\ 0 & -S_2 \end{bmatrix} \\
D_{16} &= \begin{bmatrix} -R_1 & 0 \\ 0 & -R_2 \\ -S_1 & 0 \\ R_1+S_1 & -S_2 \end{bmatrix} & D_{17} &= \begin{bmatrix} -S_1 & 0 \\ 0 & -R_2 \\ -R_1 & 0 \\ R_1+S_1 & -S_2 \end{bmatrix}
\end{aligned} \tag{4.12}$$

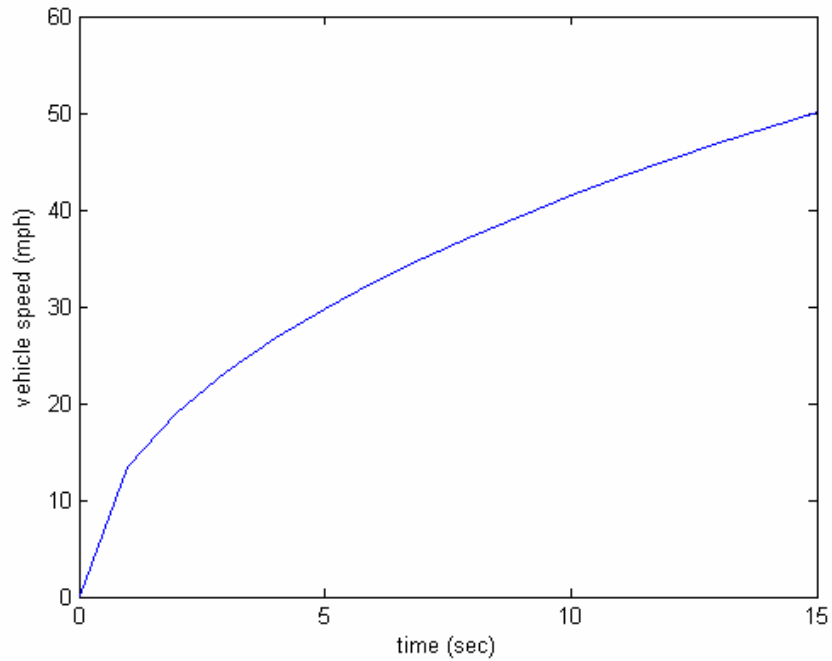


Figure 4.6: Vehicle launching at constant power (100 kW).

4.3. Mode Shifting and ECVT Efficiency

In the third step of the configuration screening process, the ECVT transmission efficiency and the feasibility of shifting mechanism are considered. Conlon (2005) and Grewe et al. (2007) provided comprehensive explanations of the ECVT design for a

power-split vehicle. The design of the mechanical point (MP) of the powertrain system and the combination of input-split and compound-split operating modes are known to be critical (See Appendix B). Grewe et al. (2007) concluded that a typical dual-mode system design requires one of the MPs to locate close to the low gear ratio in a conventional transmission (ranging from 1.5 to 4) to be beneficial for the launching drive, and one of the MPs to locate close to the high speed top gear ratio in a conventional transmission (ranging from 0.5 to 1) to be beneficial for the cruising drive. An acceptable powertrain configuration needs to have its MPs designed within these reasonable ranges.

The task of calculating MP of a configuration is equivalent to solving the input/output speed ratio when one of the MGs has zero speed. This can be easily done with the previously defined matrix D_{EV} and D_{MG} . In equation (4.8), let either ω_{MG1} or ω_{MG2} equal to zero, the input/output speed ratio, which is the corresponding mechanical point, can be calculated.

Besides the mechanical point, given the model matrix D , possible shifting mode can also be derived. For example, if an input-split system is designed and the matrix D is

$$D = \begin{bmatrix} -R_1 & 0 \\ R_1 + S_1 & R_2 + S_2 \\ -S_1 & 0 \\ 0 & -R_2 \end{bmatrix} \quad (4.13)$$

Now if it is desired that a compound-split system can be obtained by switching this system. The only two possibilities of new matrix D for the compound-split mode are

$$D_{mode21} = \begin{bmatrix} -R_1 & -S_2 \\ R_1 + S_1 & R_2 + S_2 \\ -S_1 & 0 \\ 0 & -R_2 \end{bmatrix} \text{ or } D_{mode22} = \begin{bmatrix} -R_1 & 0 \\ R_1 + S_1 & R_2 + S_2 \\ -S_1 & -S_2 \\ 0 & -R_2 \end{bmatrix} \quad (4.14)$$

where the node coefficient $-S_2$ replaces one of the two zeros in the second column of matrix D in (4.13). Only $-S_2$ can be used because other connections between the power sources and gear nodes are fixed with the existing node coefficients. These two possible gears identify two powertrain systems, shown in Figure 4.7.

Although the possible shifting modes can be identified by matrix D , whether the shifting is feasible or not also needs to be checked. Notice in configuration (a) in Figure 4.7, when it is switched from input-split mode to compound-split mode (lock CL2 and release CL1), because the node (sun gear of PG2) to be locked with engine node (ring gear of PG1) was grounded in input-split mode, the speed of engine must reduce to zero to make the synchronized shift. Based on today's engine technology, this type of shifting operation prevents the configuration (a) from practical. Configuration (b) does not have this limit since the shifting node is connected to MG1. As a result, for a practical shifting operation, the shifting node can not be connected to either engine or vehicle. What this reflexes on the matrix D is that when considering the possible new matrix D for the switching mode, the zero(s) at either the first row (engine node) or the second row (vehicle output node) can not be replaced with node coefficient. Now for the model in (4.13), only zero at element (3,2) can be replaced by $-S_1$ to form a possible compound-split model.

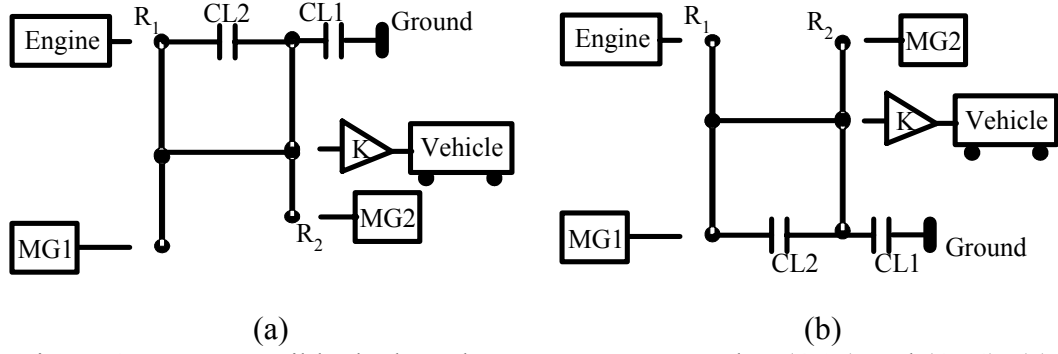


Figure 4.7: Two possible dual-mode systems correspond to (4.13) and (4.14): (a) represented by matrix D and D_{mode21} ; (b) represented by matrix D and D_{mode22} .

Following the procedure described above, given matrix D , all design candidates can be systematically examined. Configurations without proper MPs in either of the possible operating mode need to be screened out. As for the demonstrated design case, possible shifting mode of each remaining configuration candidate is first generated. The mechanical points can then be calculated from (4.8). Because the planetary gear gain is assumed to be equal to 2 in this screening process, we can set $R_i=2$ and $S_i=1$ to simplify the calculation. Now matrix D in (4.13) becomes

$$D_{model} = \begin{bmatrix} -2 & 0 \\ 3 & 3 \\ -1 & 0 \\ 0 & -2 \end{bmatrix} \quad (4.15)$$

and the only possible compound-split modes in (4.14) become

$$D_{mode2} = \begin{bmatrix} -2 & 0 \\ 3 & 3 \\ -1 & -1 \\ 0 & -2 \end{bmatrix} \quad (4.16)$$

From equation (4.8), the input-split mechanical point (MP) of D_{model} was found to be 1.5, and the possible compound-split MPs are 1.5 and 0. Since the desired input-split MP is

between 1.5 and 4 and the desired compound-split MP locates between 0.75 and 1, the possible configurations for compound-split mode fail to satisfy the design objective. Therefore, the configuration represented in (4.15) is eliminated.

This process was repeated for all the surviving design candidates from the previous steps. Only two configurations (D_8 and D_7 in (4.12)) were found to have the MPs within the desired range and are left for further consideration. For these three surviving candidates, the first one (PT1) is the design in (Holmes et al., 2003) and the second one (PT2) is the design in (Ai and Mohr, 2005). Their powertrain models are shown in Chapter 3 in details.

To summarize, in this chapter, a configuration screening process is suggested which systematically search through all possible configurations for a 2-PG dual-mode power-split design. Feasible design solutions based on specified design objectives are generated. As shown in the example, the initial 1152 mathematically possible design solutions are quickly narrowed down to 2. These 2 candidates will be further analyzed by the combined configuration and control optimization process suggested in the next chapter.

CHAPTER 5

COMBINED CONFIGURATION DESIGN, COMPONENT SIZING, AND CONTROL OPTIMIZATION OF THE POWER-SPLIT HYBRID VEHICLES

Comparison of different powertrain configurations can not be done without implementation of some kind of optimal control strategies. Control strategies based on engineering intuition frequently fail to explore the full potential of the power-split hybrid vehicles because the multi-power-source nature of the powertrain systems. Optimal control strategies, on the other hand, achieve the performance assessment of each configurations based on the best execution rather than an execution with unknown quality and refinement.

In this chapter, a procedure is proposed for designing an optimal power management strategy for split hybrids based on the deterministic dynamic programming (DDP) technique. The optimal power management solution on each of the design configuration is obtained by minimizing a defined cost function. The results are then used as the performance benchmarks and compared to reach the design optimization. This procedure is applied to the surviving candidates from Chapter 4 with study on power source component sizing and planetary gear gains.

5.1. Dynamic Program

Dynamic programming (DP) (Bellman, 1957; McCausland, 1969; Kirk, 1970; Gluss, 1972; Cooper and Cooper, 1981) is a multi-stage decision-making process involving a dynamic system, a cost function, and control and state grids. The optimal control signal is searched backwards along a horizon. This cost function is maximized or minimized within the boundary of the state grid. This algorithm guarantees global optimal solution up to the grid accuracy of the states for both linear and nonlinear systems. Furthermore, it is flexible in accommodating different definitions of cost functions or state and input constraints. However, a major limitation of the dynamic programming is the extreme computational load, known as the “curse of dimensionality”. As the number of states and inputs increases the computation time and the memory requirement increase exponentially. Therefore, only problems with small number of states and inputs are feasible of applying DP.

5.1.1. Concept

The DP technique is based on the principle of optimality, stated by Bellman (1957) as “An optimal policy has the property that, whatever the initial state and optimal first decision may be, the remaining decisions constitute an optimal policy with regard to the state resulting from the first decision”. This concept can be explained as follows.

For an optimization problem, choose $u(k)$ ($k=0,1,\dots,N-1$) to minimize or maximize the cost function

$$J = G_N(x(N)) + \sum_{k=0}^{N-1} L_k(x(k), u(k), w(k)) \quad (5.1)$$

where

$$x(k+1) = f(x(k), u(k), w(k)), \quad k = 0, 1, \dots, N-1 \quad (5.2)$$

subject to

$$x(k) \in X(k) \subset \mathfrak{R}^n, \quad u(k) \in U(x(k), k) \subset \mathfrak{R}^m \quad (5.3)$$

Here, $x(k)$ is the state vector at stage k in the space of $X(k)$, $u(k)$ is the control vector, $w(k)$ is a predetermined disturbance, f is the transition function that represents the system dynamics, L is the instantaneous transition cost and G_N is the cost at final stage N . Constraints g_i and h_j may be imposed on state variables and control variables, respectively.

$$g_i(x(k)) \leq 0, \quad i = 1, 2, \dots, q \quad (5.4)$$

$$h_j(u(k)) \leq 0, \quad j = 1, 2, \dots, p \quad (5.5)$$

The principle of optimality implies that if $U = \{u^0, u^1, u^2, \dots, u^{N-1}\}$, where u^k maps states $x(k)$ into control signals $u_{optimal}(k) = u^k(x(k))$, is the optimal control solution that minimizes (maximizes) the given cost function, then the truncated policy $\tilde{U} = \{u^r, u^{r+1}, u^{r+2}, \dots, u^{N-1}\}$ ($0 < r < N$) is the optimal control solution for the sub-problem of minimizing (maximizing) the cost function

$$\tilde{J} = G_N(x(N)) + \sum_{k=r}^{N-1} L_k(x(k), u(k), w(k)) \quad (5.6)$$

The optimal solution can be obtained if we first solve a one stage sub-problem involving only the last stage and then gradually extend to sub-problems involving the last two stages, last three stages ...etc. until the initial stage is reached. In this manner, the

overall optimization problem can be decomposed into a sequence of simpler minimization problems. Such as at the last step $N-1$

$$\tilde{J}^*(x(N-1)) = \min_{u(N-1)} \{G_N(x(N)) + L_{N-1}(x(N-1), u(N-1), w(N-1))\} \quad (5.7)$$

And at any other given step k , $0 < k < N-1$

$$\tilde{J}^*(x(k)) = \min_{u(k)} \{ \tilde{J}^*(x(k+1)) + L_k(x(k), u(k), w(k)) \} \quad (5.8)$$

where $\tilde{J}^*(x(k))$ is the optimal cost-to-go function or optimal value function at state $x(k)$ starting from time stage k . It represents the optimal cost if at stage k the system starts at state $x(k)$ and follows the optimal policy thereafter until the final stage.

When optimal control signals for all the state grids at all the stages are obtained the optimal control schedule of the whole problem is retrieved by starting at the initial state and following the optimal controls until reaching the final stage.

5.1.2. Dynamic Program on Power-Split Powertrain Models

Utilizing DP on a power-split HEV is challenging because of the larger number of possible control decisions. Shown in Table 5.1 are the typical states and inputs in the power management control problems of several hybrid vehicles and the conventional vehicle (Lin, 2004; Kim, D., 2006; Kim, M., 2007). Here we assume the optimization objective is to analyze the control of the powertrain power flow at the system level. Notice that the gear control for automatic transmissions has discrete values with very limited choices (e.g., gear can be any integer from 1 to 6 for a typical transmission) and all other variables have continuous values (e.g., v can be any value from 0 to 140 mph for

a typical sedan without considering going backwards). By comparison, the power-split HEV has the biggest problem size in terms of control states and inputs.

Table 5.1: States and inputs in different types of vehicles (Assume the objective is to analyze the control of the powertrain power flow at the system level)

	States	Control Inputs
Power-split HEV	ω_e, v, SOC	$T_e, T_{MG1}, T_{MG2}, (Gear^*)$
Parallel HEV	v, SOC	$T_e, T_{MG}, Gear$
Series HEV	ω_e, v, SOC	T_e, T_{MG}
Fuel-cell Vehicle	v, SOC	I_{cell}
Conventional Vehicle	V	$T_e, Gear$

* The gear input on a power-split HEV is only necessary when the powertrain configuration has multiple operating modes.

Because the large state/input space requires excessive computation, problem simplification becomes a necessary art to compromise between the complexity of the system and the accuracy of the solutions. Figure 5.1 shows the state transition of the DDP problem on a power-split vehicle. The states are engine speed ω_e , vehicle speed v , and the battery SOC . The control inputs are MG1 torque T_{MG1} , engine command $Throttle$, and MG2 torque T_{MG2} . Here the driving mode, or gear input, is assumed to be determined by the vehicle speed v and the driving power demand P_d . Because the goal of the control is to follow a predefined driving cycle, it draws the knowledge of v and P_d . And because the power flow satisfies

$$P_d = P_e + P_{MG1} + P_{MG2} \quad (5.9)$$

P_d determines the control input T_{MG2} by

$$T_{MG2} = (P_d - T_e(throttle) \cdot \omega_e - T_{MG1} \cdot \omega_{MG1}(\omega_e, v)) / \omega_{MG2} \quad (5.10)$$

where T_e and ω_{MG2} are calculated from the states and input signals. As a result, given a driving cycle, state v can be treated as known and input T_{MG2} is dependent on other states and inputs, which reducing the state/input grid space dimension by two.

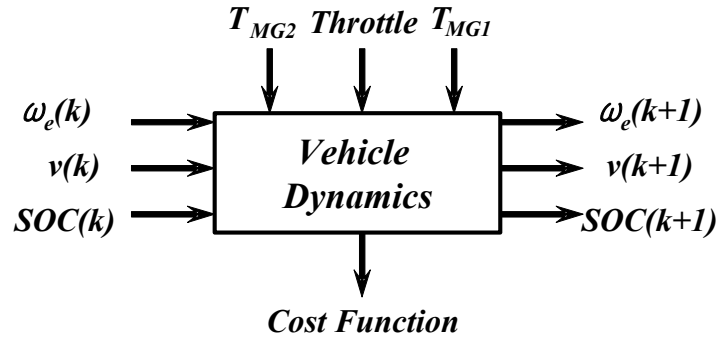


Figure 5.1: Formulation of the DP problem on a power-split system.

The rest of the states and inputs need to be discretized. The grid sizes of the state variables and the control signals are important because they are directly related to the simulation accuracy and computational cost. Small grid sizes lead to longer computation time but more accurate optimization results and larger grid sizes save computational cost but may obtain inaccurate results. Also, the state and input grids need to be coherent else a state grid may not be reached by the control. The selected grid points are shown in Table 5.2.

Table 5.2: The selected grid points in DDP.

States	
Engine Speed [rpm]	1000:50:3000
State of Charge	0.4:0.003:0.7

Control Inputs	
Engine Throttle	0:0.025:1
MG1 Torque [Nm]	-300:15:300

The cost function used in this DDP problem combines two objectives: to maximize the fuel economy and to keep the SOC sustained. Based on these, the cost function to be minimized is calculated as:

$$J = \alpha(SOC_N - SOC_f)^2 + \sum_{k=0}^{N-1} fuel_k \quad (5.11)$$

where the fuel consumed at each step and a terminal constraint on SOC are considered. SOC_f is the desired SOC at the final time, and α is a positive weighting factor. The optimization is subject to engine and electric machine constraints

$$\begin{aligned}
\omega_{e_min} &\leq \omega_{e_k} \leq \omega_{e_max} \\
\dot{\omega}_{e_min} &\leq \dot{\omega}_{e_k} \leq \dot{\omega}_{e_max} \\
\omega_{MG1_min} &\leq \omega_{MG1_k} \leq \omega_{MG1_max} \\
T_{MG1_min} &\leq T_{MG1_k} \leq T_{MG1_max} \\
\omega_{MG2_min} &\leq \omega_{MG2_k} \leq \omega_{MG2_max} \\
T_{MG2_min} &\leq T_{MG2_k} \leq T_{MG2_max}
\end{aligned} \quad (5.12)$$

A large penalty is given for the control which violates these constraints, or drives the states outside of these constraints. As mentioned before, the battery is assumed to have enough voltage to supply to the MGs.

Figure 5.2 shows a set of results from a sample DDP problem. This problem utilizes a FTP75 driving cycle for the first powertrain candidate (PT1), one of the two surviving configurations from the last chapter. Plot (a) shows that the obtained vehicle

speed tracks the reference driving cycle speed closely, while the battery is controlled to sustain the charge close to the targeted SOC at 0.55 (plot (b)). The powertrain control signals for the power sources are shown in plots (c) and (d) for engine and MG1, respectively.

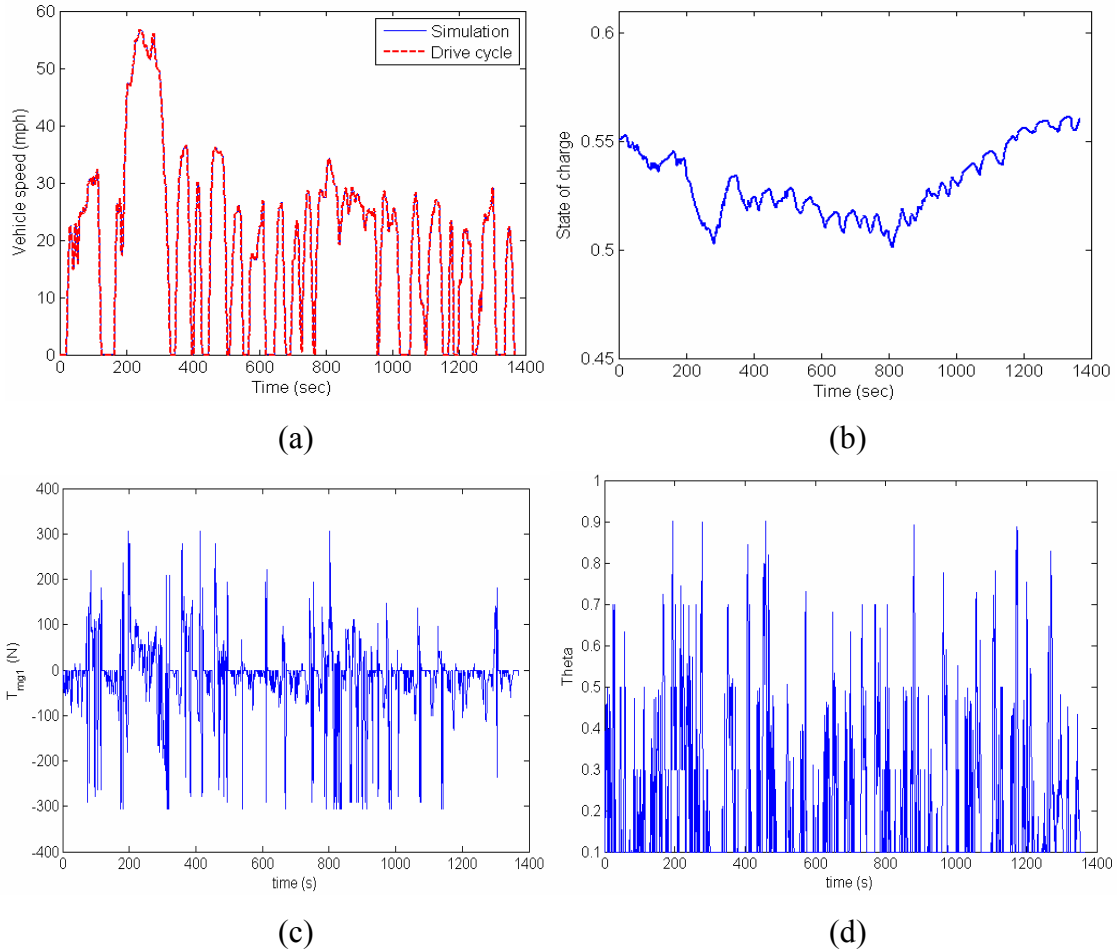


Figure 5.2: Example vehicle control performance results by DDP.

5.1.3. Numerical Accelerator Technology

Because the DDP search is exhaustive, it is computationally intensive. In this study, several techniques were applied to reduce the computation load. These techniques are not universal and may not be directly applicable to other hybrid vehicle design

problems. However, it is worthwhile to document these techniques as they play a crucial role in implementing the DDP codes. Without these tricks, DDP problem could be too slow to be solved on PCs using standard software package such as Matlab, which is increasingly the choice for many engineers.

Firstly, the inequality constraints sometimes can be checked based on the initial conditions before running the simulation. Cases failed to satisfy the constraints are penalized and the simulations can be skipped. For example, because the PG system has known kinematic relationships, MG1 initial speed can be calculated given the initial vehicle speed and engine speed. If the result speed violates the constraint, a large penalty is assigned and the simulation can be skipped. By doing this, about 10% of the computation can be avoided.

Secondly, SIMULINK allows us to load the simulation once and run a group of cases together. Within the time of running a single simulation, the results of a group of simulations can be obtained. To create the group initial conditions, the states and inputs need to be vectorized. For instance, if the simulation model is loaded with a SOC vector [0.4:0.003:0.7], an engine throttle vector [0:0.025:1], and specified scalar value of other states and inputs, SIMULINK actually takes in a matrix of cases, and all scenarios specified by the matrix can be simulated in one function call. Table 5.3 shows the comparison of computation time requirements between the vectorized inputs approach and the traditional approach. Simulation with vectorization technique reduces the computation time by a factor of about 300.

Table 5.3: Vectorization approach effect on simulation time.

Simulation Cases	Simulation Approach	Simulation Time (sec)
One engine speed SOC grids [0.4:0.003:0.7] Throttle grids [0:0.025:1] One MG1 torque	One case at a time Simulation	153.6
	Vectorized Simulation	0.5

Thirdly, to further accelerate simulations, the SIMULINK model can be converted into a script (.m) file. When all the simulations for calculating transition table are made in an m-file, it further reduces the computation time by a factor of 10. With the help of all these techniques, the transition table computation for the FTP75 driving cycle which took days previously was generated in about three hours on a desktop PC.

5.2. Configuration Optimization

Deterministic dynamic programming (DDP) explores the full potential of each design candidates. By comparing these benchmark (best execution) performances, the configuration that has the best performance and satisfies all of the design constraints can be identified. Recall in the design screening process described in Chapter 4, we only considered the effect of different configuration designs with the MG sizing and planetary gear gains assumed to have constant values. In this section, parametric variations on the MG sizing and the planetary gear gains are explored on the surviving configuration candidates. For each powertrain configuration with parametric variation, DDP solution is obtained to benchmark the vehicle performance.

Obviously, to search through optimal design parameters, one could use systematic methods such as Sequential Quadratic Programming (SQP) and search through the

parameter space iteratively. This approach requires a wrapper program to integrate the SIMULINK file with the DDP optimization together with the SQP code. In addition, because of the iterative nature of the SQP search, the overall process will be extremely computation intensive. In this dissertation, we will demonstrate the basic concept using a brute-force search approach. For the electric machine sizing, the MGs are given values ranging from 10 to 50 kW with the summation of the two limited at 60 kW. For the planetary gear dimension, the ratio between ring gear radius and sun gear radius

$$K_i = \frac{R_i}{S_i} \quad (5.13)$$

is searched within a feasible design range, from 1.6 to 2.4. With each variation, the vehicle performance is benchmarked with the optimal control achieved by DDP. These results are then compared to conclude the optimal design parameters.

The complete DDP results are shown as tables in Appendix C. Fuel economy alone is used for the comparison. In each simulation, the effect of mismatched SOC, the change between its initial and final values, is compensated for by conducting several runs with different initial values of SOC. Figure 5.3 shows that the fuel consumption (without SOC compensation) changes monotonically and almost linearly with the change in SOC between its initial and final values (Figure 5.4). The fuel efficiency with zero SOC variation can then be calculated by interpolation.

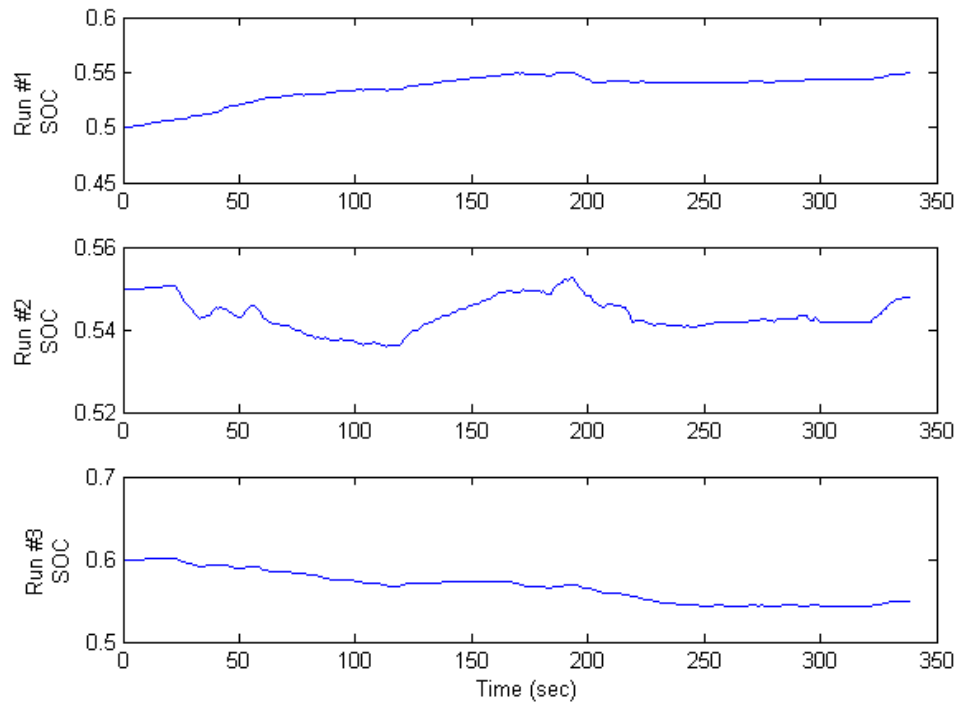


Figure 5.3: SOC under the same driving-cycle with different initial values.

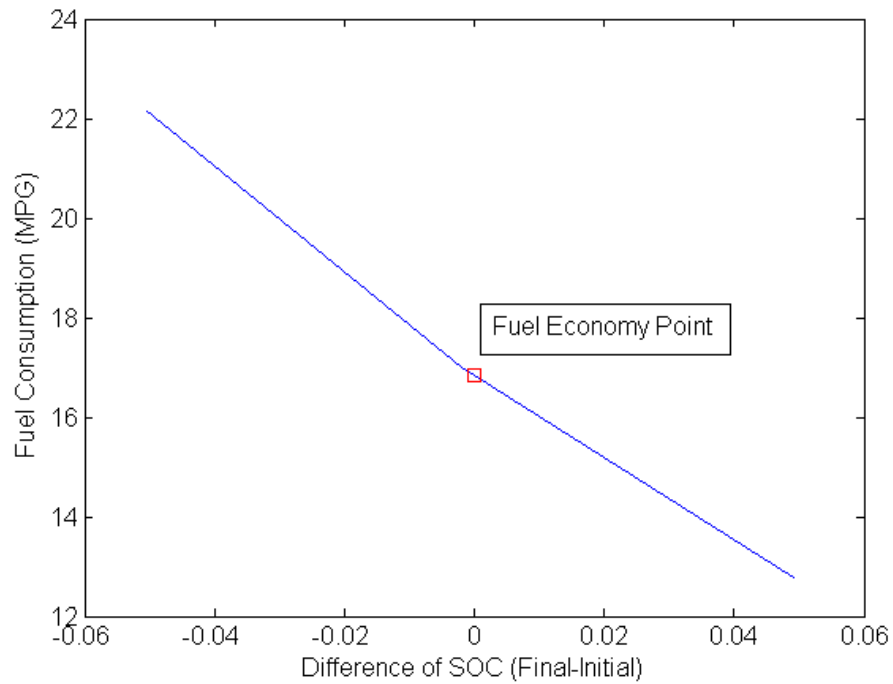


Figure 5.4: Relationship between fuel consumption and change in battery SOC.

In the result tables in Appendix C, N/A means that the corresponding configuration can not satisfy the driving demand with some of the constraints violated in the simulation. Note when varying the electric machine sizing, if any one of the MG is relatively small (i.e., 10 kW), the powertrain fails to satisfy the driving demand. This is because of the power circulation in the power-split vehicle. The engine input power is circulated after it is split. The split power in the electrical path goes through both MGs to reach to the final wheel. Figure 5.5 shows the circulated electric power under a launching portion of the driving cycle. Both of the MGs should be sized above this value to generate or motor the power.

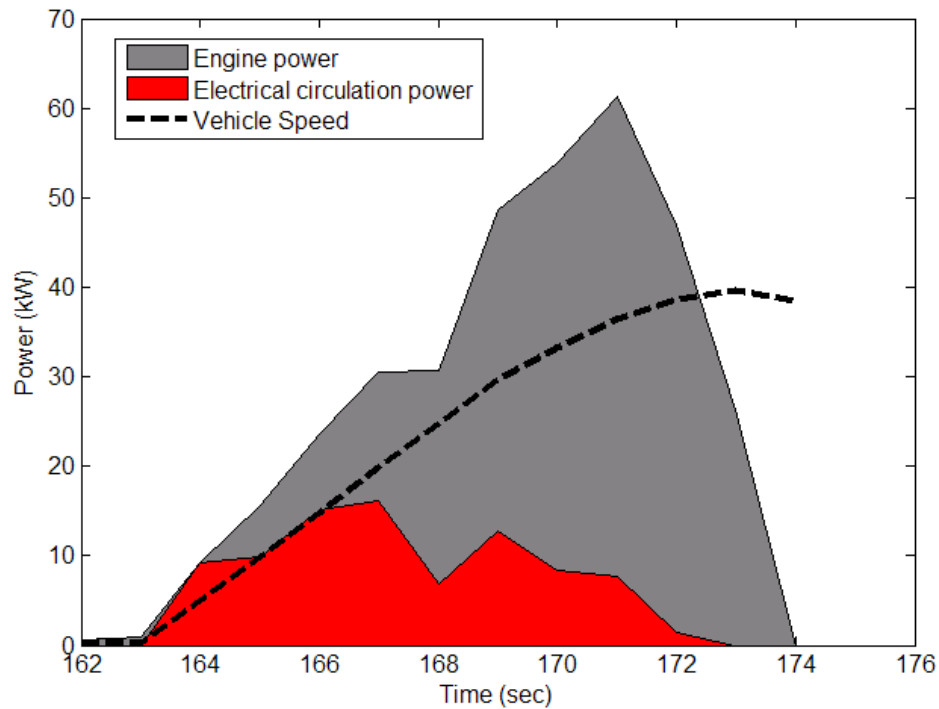


Figure 5.5: Electric power circulation under a launching maneuver (PT2, MG1=20kW and MG2=40kW).

The effect of varying the PG parameters can be studied by using a contour plot. Figure 5.6 shows the result of PT2. It appears that the fuel efficiency increases as K_2

increases for this powertrain configuration. To understand the reason, the results from one design ($K_1=1.6$ and $K_2=2.2$) with higher fuel efficiency (18.43 mpg) and one design ($K_1=1.6$ and $K_2=1.6$) with lower fuel efficiency (17.57 mpg) are compared. The difference mainly lies in the performance of the electric machines. Figure 5.7 shows the MG2 operating points of both cases in the power efficiency map. As marked, the lower-efficiency case has more points (triangles) in regions with poor electric efficiency. This can also be observed in Figure 5.8. When the vehicle is launching and requires large amount of power (e.g., between 20 sec and 75 sec, and between 170 sec and 200 sec), the MG2 is driven at lower speeds (Figure 5.8a) with high torques (Figure 5.8b) for the lower fuel efficiency case, which is not efficient. The simulation results also show that in both cases, the vehicles are following the driving cycle (Figure 5.9a) and the batteries are controlled to have the same final values (Figure 5.9b). This guarantees the electric powers supplied from the batteries over the entire driving cycle are the same for both cases. Then the lower power efficiency of MG2 results in the lower fuel efficiency since more power is lost in the electrical path.

To explain why K_2 has such effect on the MG2 operation, let's look at the configuration of PT2. In the launching mode of PT2 (as shown in Figure 5.10), because the ring gear of PG2 is grounded, increasing K_2 will increase the speed ratio of MG2 over the vehicle output shaft. This means, for the same vehicle speed, a larger K_2 results in a higher MG2 speed. When the vehicle speed is low and the MG2 torque is high, the configuration with larger K_2 pushes the MG2 operating point to avoid the low power efficiency region and achieves better fuel efficiency.

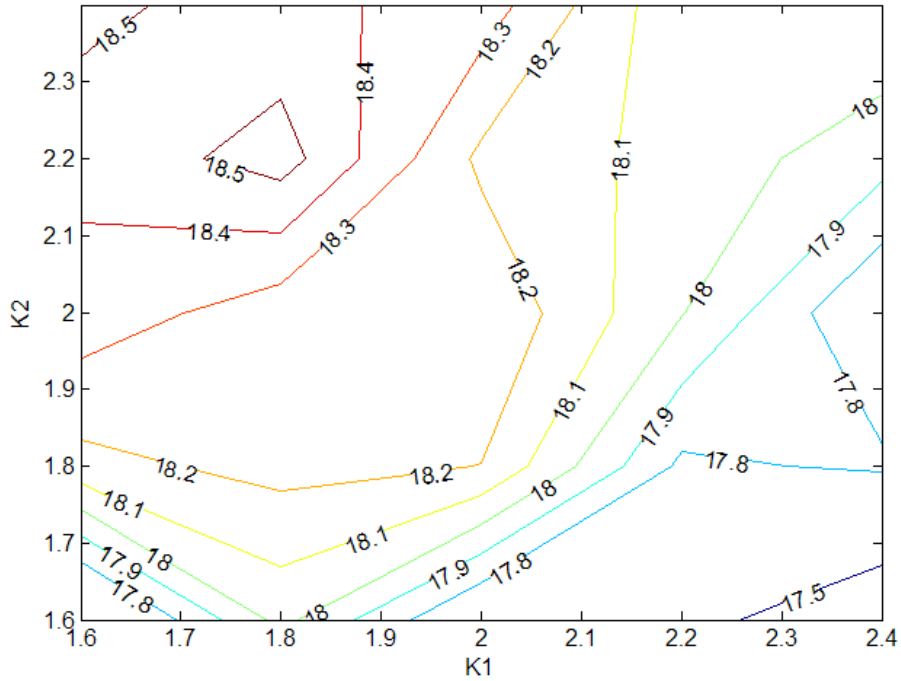


Figure 5.6: Fuel economy contour plot for DDP results with different gear sizing (PT2, MG1=20kW and MG2=40kW).

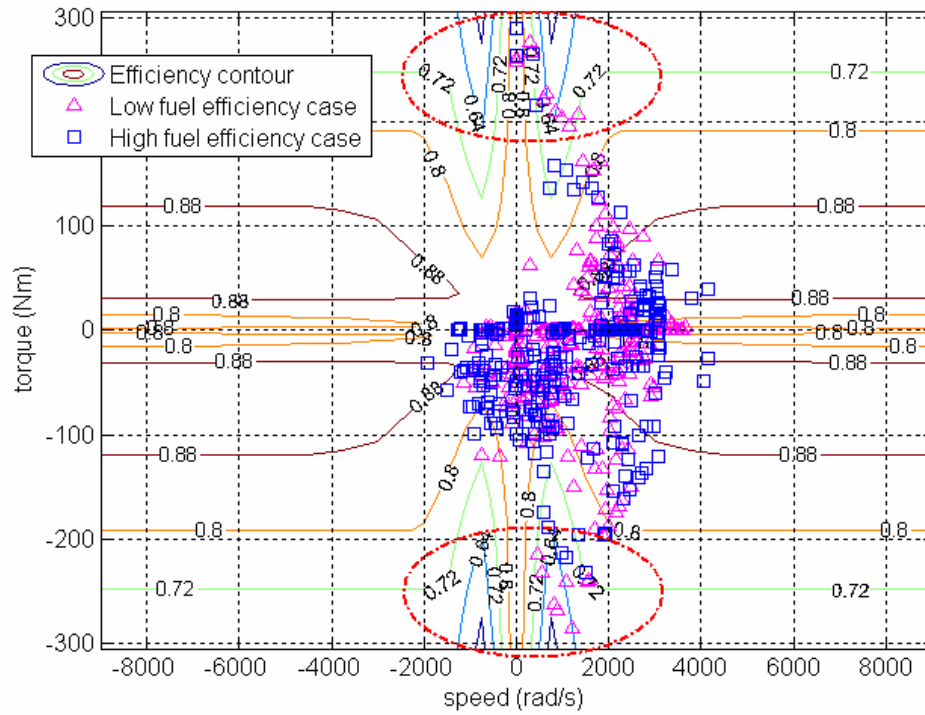


Figure 5.7: MG2 efficiencies of two different design cases (High fuel efficiency case: $K_1=1.6$ and $K_2=2.2$, and low fuel efficiency case: $K_1=1.6$ and $K_2=1.6$).

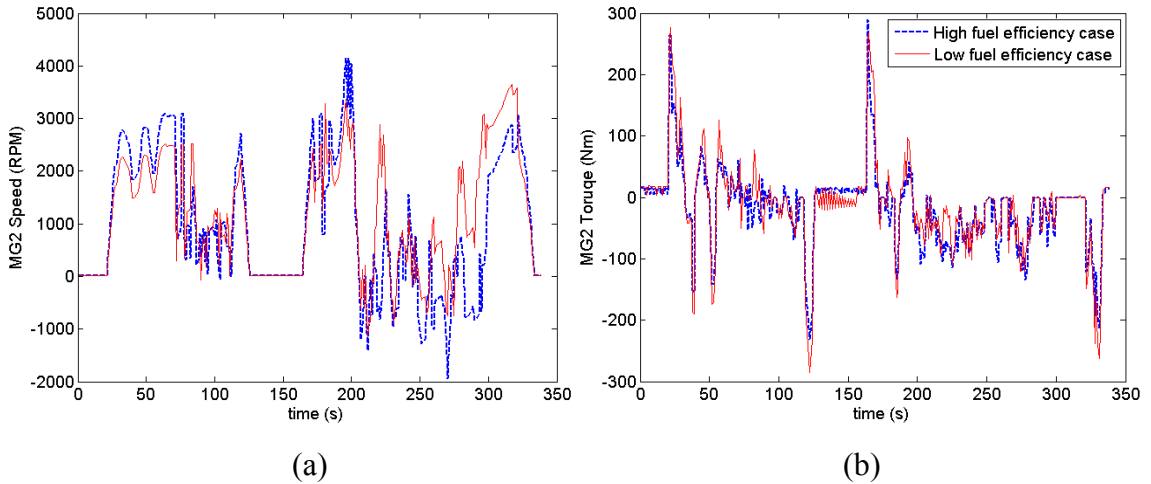


Figure 5.8: MG2 speeds and torques of two different design cases (High fuel efficiency case: $K_1=1.6$ and $K_2=2.2$, and low fuel efficiency case: $K_1=1.6$ and $K_2=1.6$).

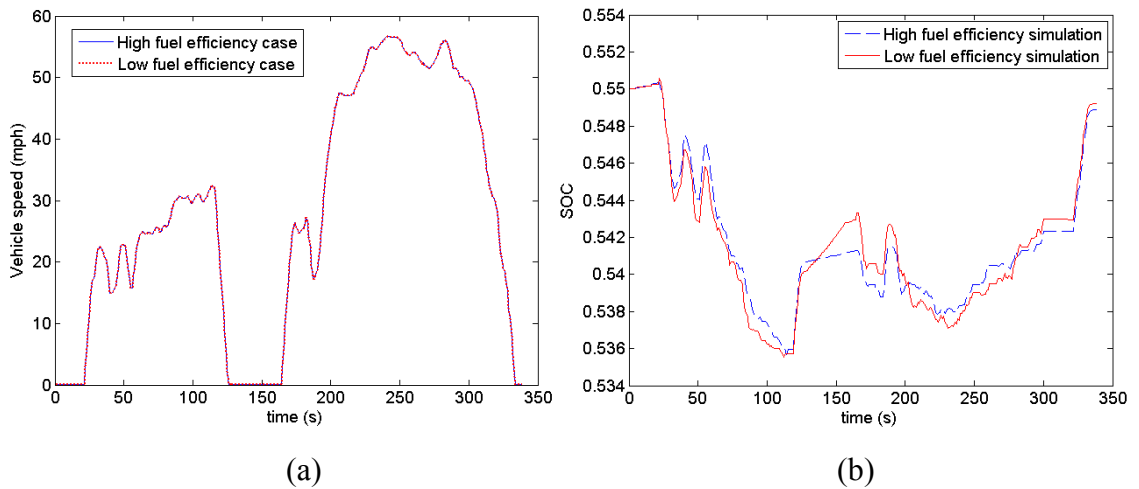


Figure 5.9: Vehicle speeds and battery SOC of two different design cases (High fuel efficiency case: $K_1=1.6$ and $K_2=2.2$, and low fuel efficiency case: $K_1=1.6$ and $K_2=1.6$).

From the result tables in Appendix C, the peak fuel economy value of each powertrain configuration represents the potential of each design. We now can compare the best potential for every design candidates. As shown in Figure 5.11 (result from the conventional vehicle is also shown for comparison), PT2 with MG1=20 kW, MG2=40 kW, $K_1=1.6$ and $K_2=2.4$ has the best fuel economy and this configuration is concluded as the design with the highest potential. It should be noted that the difference between PT2

and PT1 is small. This implies that while PT2 may have better results in this case study, PT1 also have high potential if the design and control are well executed.

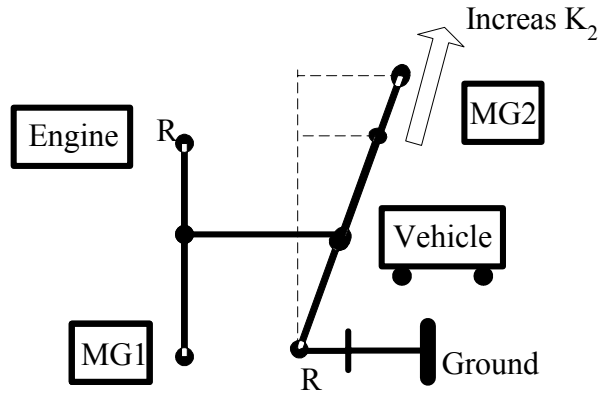


Figure 5.10: In the PT2 configuration, increasing K_2 results in higher speed of MG2 at the same vehicle speed.

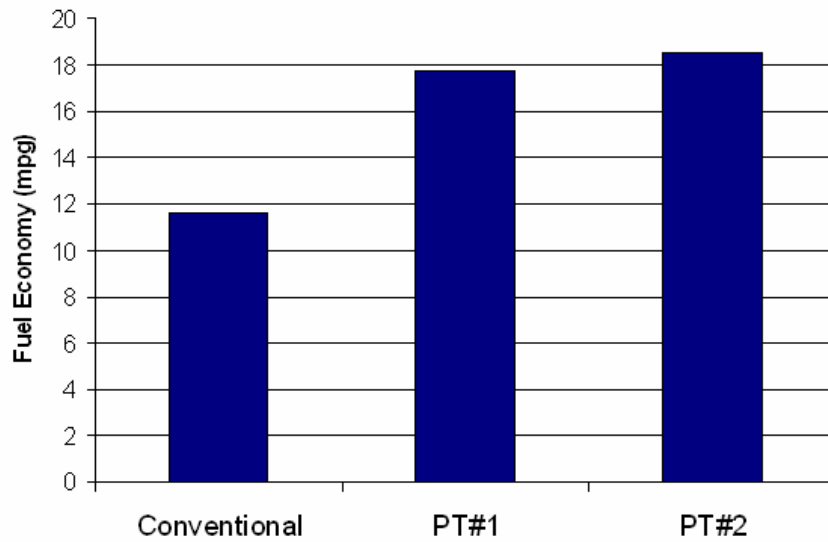


Figure 5.11: Potential fuel economy comparison between different configurations.

CHAPTER 6

IMPLEMENTABLE OPTIMAL CONTROL DESIGN OF THE POWER-SPLIT HYBRID VEHICLES

In Chapter 5, the configuration with the best performance benchmarked by DDP is selected. The problem of DDP is that it requires a priori knowledge of the future driving conditions. Because a priori knowledge is not precisely known in daily driving, the control strategy developed from DDP is not implementable. Two implementable power management control algorithms are studied in this chapter. In both algorithms, the split between the engine power and the battery power is determined by the optimal control strategies and the engine operation is then optimized by controlling the two electric machines.

The first algorithm is based on the stochastic dynamic programming (SDP) technique. This approach assumes that there is an underlying Markov process to represent the power demand from the driver. Instead of being optimized over a given driving cycle like DDP, the power management strategy is optimized in general driving conditions with known power demand transition probabilities. Similar approaches to automotive powertrain control problems can be found in (Kolmanovsky et al, 2002; Lin et al, 2003). In this chapter, this SDP approach is modified and applied to power-split HEVs. The control law derived from SDP can be directly used in real-time implementation because it has the form of (nonlinear) full state-feedback.

Both DDP and SDP require extensive search during the optimization process which causes excessive computations. As the powertrain system becomes more complicated in a power-split hybrid vehicle, these design processes become time consuming. As an alternative solution with much reduced computational cost, equivalent consumption minimization strategy (ECMS), an instantaneous minimization method is also studied. Ideally, we want to solve the following optimization problem

$$\min\left(\int E(t)dt\right) \quad (6.1)$$

where the fuel consumption $E(t)$ is minimized over the entire driving schedule. In an instantaneous optimization, this global criterion is replaced by a local estimation cost $\tilde{E}(t)$ and the power distribution is determined by

$$\int\left(\min\left(\tilde{E}(t)\right)\right)dt \quad (6.2)$$

Obviously the global minimization problem and the instantaneous minimization problem are not equivalent. However, the instantaneous minimization strategy can be easily implemented. The ECMS was originally proposed by Paganelli et al. (2000) for parallel hybrid vehicle applications. This algorithm is modified to apply to the power-split HEVs.

6.1. Power-Split and Engine Optimization

Regardless of the configuration design selected, the power-split powertrain decouples the engine speed from the vehicle speed with the electric continuously variable transmission. Therefore, the engine can operate efficiently under a wide variety of driving conditions. To fully realize the benefits of a power-split hybrid, the engine cooperates with the two electric machines. These two electric machines can be viewed as a speeder

and a torquer. The speeder is controlled to manipulate the speed of the engine, and the torquer helps to satisfy the torque requirement. For instance in the design of THS, the MG1 plays the role of the speeder, and the MG2 is the torquer (Hermance, 1999). Some designs have three or more electric machines, but they still serve as these two types. There can be two torquers working together (front wheel and rear wheel) to assist the torque while one speeder to control the engine speed.

A divide-and-conquer approach is used to decouple the control synthesis of a power-split HEV into two steps, system optimization and engine optimization (Figure 6.1). The system optimization specifies the engine power demand. Then the engine optimization controls the engine operation. The engine optimal controller selects a pre-calculated optimal engine speed based on the engine power command given by the system optimal controller. This desired speed is then achieved by manipulating the speeder electric machines following the speed relationship imposed by the lever diagram. Depending on the torque capacity and speed range of the controlled electric machine, the desired engine speed may not be achievable, or even if it is, may be achievable after a transient. The power surplus or deficit (difference between desired power and engine power) is then supplied by the other electric machine. This design procedure was explained in (Kimura et al., 1999) and (Ai et al., 2004).

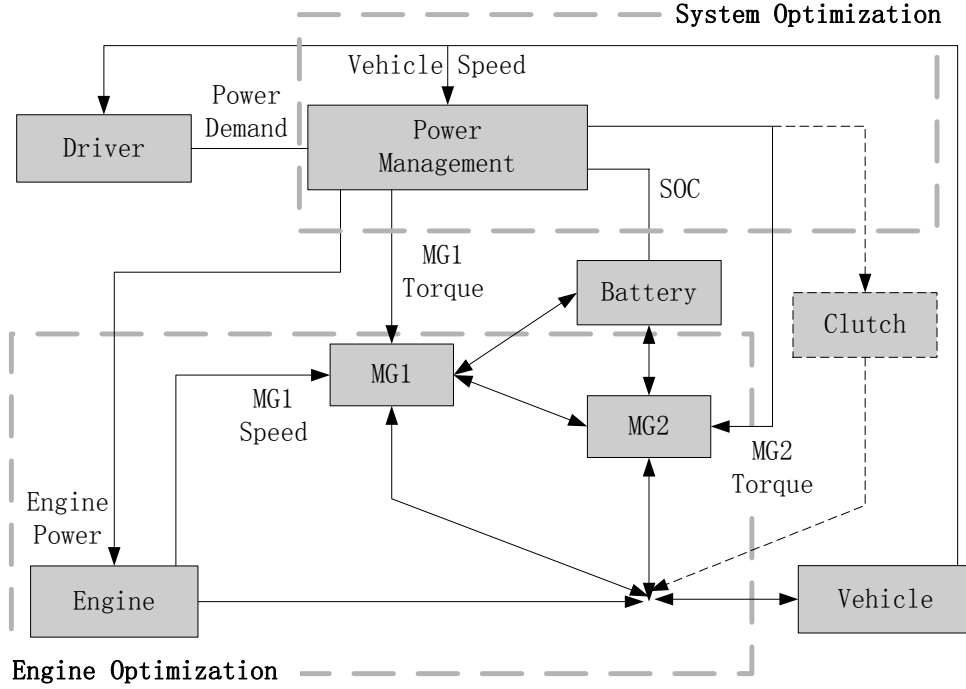


Figure 6.1: Two-step control of the power-split powertrain showing system optimization and engine optimization.

The speeder MG generates torque so that its speed converges to a reference point calculated from the engine command speed and the vehicle speed. To track this reference speed, a feed-forward plus feed-back controller is designed (Figure 6.2). The feed-forward control signal is determined as the torque needed to balance the split engine torque at steady state. As explained in section 2.2.1, the torque-split ratio at steady state in a planetary gear train is fixed and can be calculated from the configuration design. Use the selected PT2 as an example, because the engine and MG1 connect to the ring gear and sun gear of PG1, respectively. The engine torque split from ring to sun gear is

$$T_{sun} = \frac{S_1}{R_1} T_e \quad (6.3)$$

which is the feed-forward torque signal to MG1 at the sun gear. A PI controller is then designed to eliminate the error between the real engine speed ω_e and the command engine speed $\omega_{e_command}$. Overall, the MG1 control signal is

$$T_{MG1} = -\frac{S_1}{R_1} T_e + \left[p_p (\omega_{e_command} - \omega_e) + p_i \int (\omega_{e_command} - \omega_e) dt \right] \quad (6.4)$$

where p_p and p_i are feedback control gains.

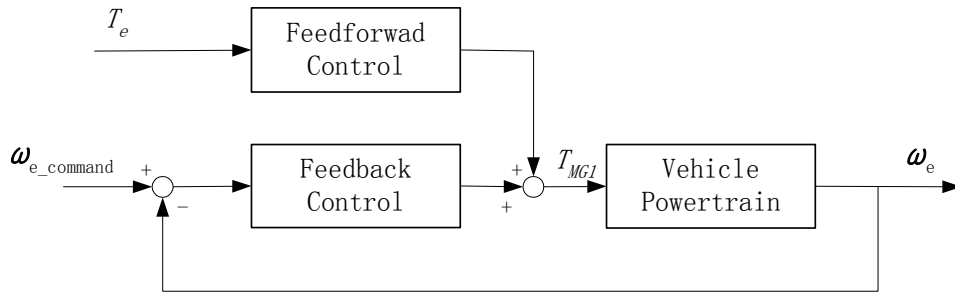


Figure 6.2: Feed-forward and feed-back controller for the MG1 torque control.

The engine optimization process explained above is engine-centric. It maximizes engine efficiency for each required engine power level. However, the system optimization, the process of choosing a proper engine power level to optimize the overall vehicle efficiency, has not been explained. This control decision should be comprehensive and should fulfill the driving demand, maintain proper battery SOC, and observe component constraints such as rotational speed and torque limit of the electric machines. Moreover, it is desirable that the power management decision leads to certain optimality such as maximizing the fuel economy. The system optimization control strategies developed by SDP and ECMS are presented in the following sections.

6.2. SDP for Power-Split Hybrid Vehicles

In deterministic dynamic programming (DDP), given a state and a decision, both the immediate cost and next state are known. If either of these is known only as a probability function, then it becomes a stochastic dynamic program (Howard, 1960; Bellman and Kalaba, 1965; Bertsekas, 1976; Ross, 1983). The SDP methodology is widely used in many control applications (Tatano et al., 1992; Bertsekas, 1995). Lin et al. (2004a) proposed a SDP control approach for a parallel hybrid vehicle. As shown in Figure 6.3, this approach extracts an optimal control policy from a Markov chain driver model, based on the power demand $P_d(k)$ statistics of multiple driving cycles. The problem is formulated with two deterministic states $v(k)$ and $SOC(k)$, and one input $P_e(k)$. To reduce the computational cost, the gear input is assumed as a mapped signal from vehicle speed. Vehicle driving torques $T_e(k)$ and $T_m(k)$ can then be calculated.

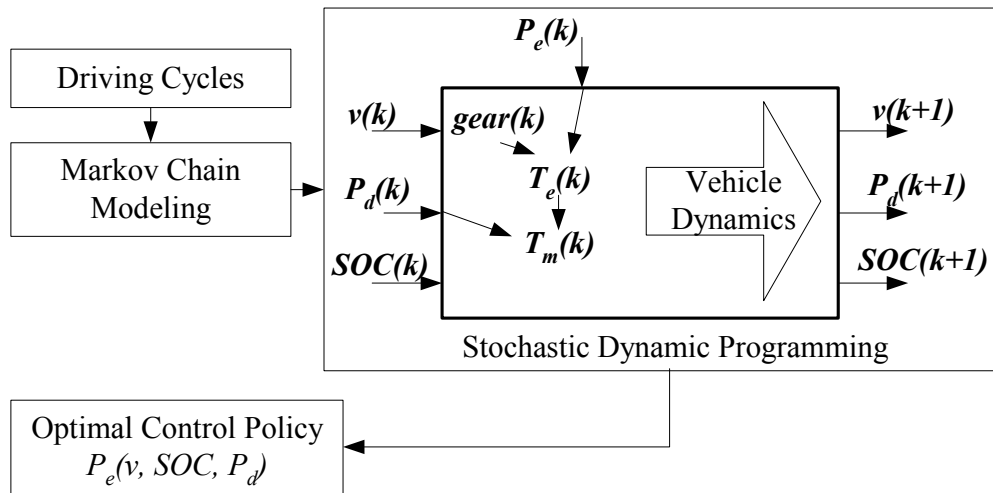


Figure 6.3: The stochastic dynamic programming design process on a parallel hybrid vehicle.

This formulation is applied to the power-split hybrid vehicle as shown in Figure 6.4. The vehicle speed $v(k)$ and battery $SOC(k)$ are kept as the two deterministic states.

The engine speed $\omega_e(k)$ is mapped to the engine power input $P_e(k)$ by assuming that the engine operates on the pre-determined curve. The engine torque $T_e(k)$ can then be calculated given engine power input. To further simplify the dynamic model and reduce the computational cost, MG1 torque $T_{MG1}(k)$ is assumed to be controlled to keep the engine speed. Because the speed of both electric machines can be calculated based on the kinematic relationship of the powertrain configuration, the MG2 torque $T_{MG2}(k)$ is then calculated to satisfy the power demand $P_d(k)$.

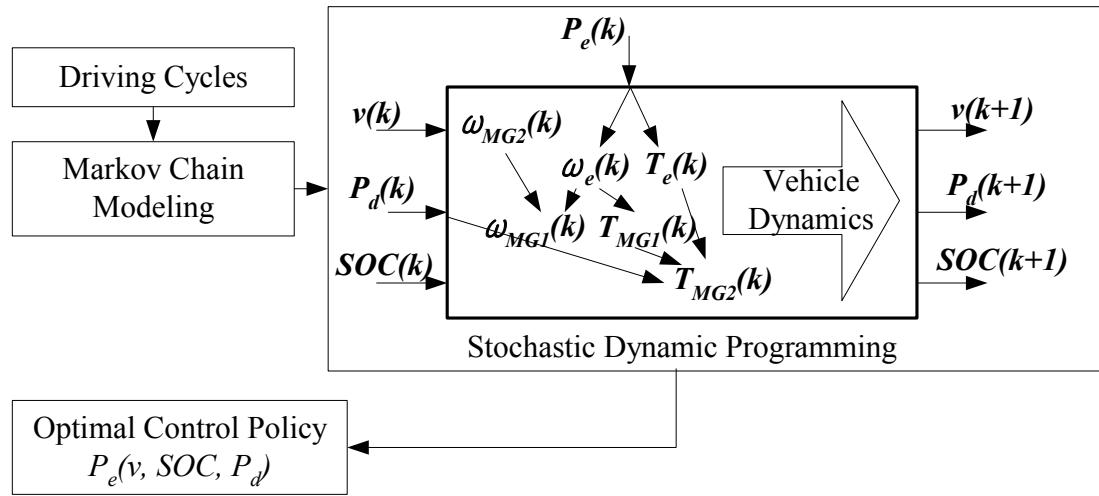


Figure 6.4: The stochastic dynamic programming design process on a power-split hybrid vehicle.

Determining proper statistical characteristics of driving power demand P_d is not a science and depends on engineering judgment and available information (e.g., updated traffic and road condition ahead). In this study, real-time traffic information is assumed to be unavailable. A stationary Markov chain model is generated as follows. Four standard driving cycles, WVUCITY, WVUSUB, WVUINTER, and UDDSHDV from ADVISOR 2002, were selected to represent mixed city, suburban, and highway driving conditions. From these driving cycles and vehicle parameters, the driving power P_d can be calculated

as a function of vehicle speed v . The observed pair (P_d, v) is further mapped onto a sequence of quantized states (P_d', v') . The transition probability could then be estimated by the maximum likelihood estimator, which counts the observation data as:

$$\hat{p}_{il,j} = m_{il,j} / m_{il} \quad \text{if } m_{il} \neq 0 \quad (6.5)$$

where $m_{il,j}$ is the number of times the transition from P_d^i to P_d^j occurred at vehicle speed state v^j , and $m_{il} = \sum_{j=1}^n m_{il,j}$ is the total event counts that P_d^i has occurred at speed v^j .

However, it is possible that the event count m_{il} is zero because of inadequate richness of the driving cycles. The probabilities of these cases are estimated by the information from the points around them. To do so, the initial probability map needs to be smoothed while

keeping the total probabilities $\sum_{j=1}^n \hat{p}_{il,j} = 1$. Figure 6.5 shows an example probability map under a given speed.

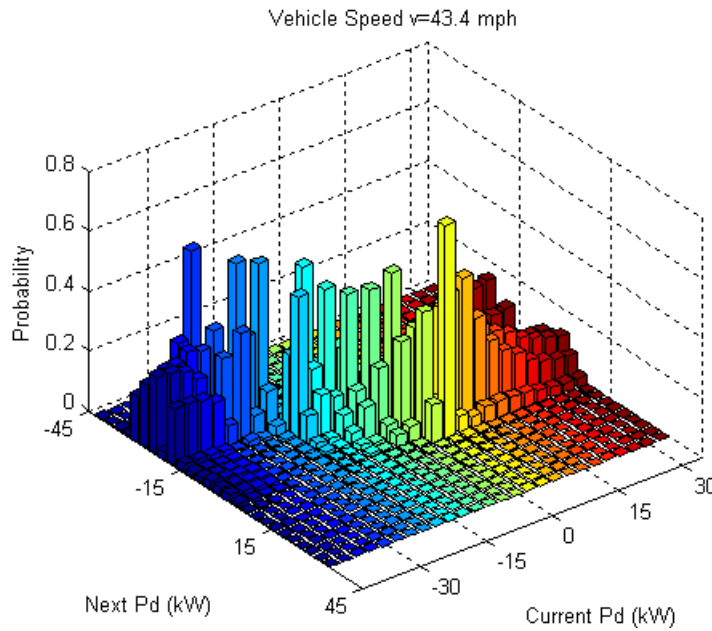


Figure 6.5: Example of power demand probability map.

Based on this stochastic Markov chain model, we formulated an infinite horizon SDP. The optimal control policy is extracted by minimizing the cost function J_π , the expected cost under control law π , over an infinite horizon:

$$J_\pi(x) = g(x, u) + \gamma \sum_{x'} p_{xx'} J_\pi(x') \quad (6.6)$$

where

$$g(x, u) = fuel_k + \alpha \Delta_{SOC}^2$$

$$\Delta_{SOC} = \begin{cases} SOC_k - SOC_d & SOC_k < SOC_d \\ 0 & SOC_k \geq SOC_d \end{cases}$$

The fuel consumption at each time step $fuel_k$ is to be minimized and battery SOC_k is penalized when it is below the desired value SOC_d . $0 < \gamma < 1$ is the discount factor. $J_\pi(x)$ indicates the resulting expected cost when the system starts at a given state and follows the policy π thereafter. u is the control signal obtained from the control policy π . x and x' are the current states and the next states. $p_{xx'}$ is the transition probability between these two states. The optimization problem is subject to a set of inequality constraints arising from component speed and torque characteristics of the power-split powertrain

$$\begin{aligned} \omega_{e_min} &\leq \omega_e \leq \omega_{e_max} \\ \dot{\omega}_{e_min} &\leq \dot{\omega}_e \leq \dot{\omega}_{e_max} \\ \omega_{MG1_min} &\leq \omega_{MG1} \leq \omega_{MG1_max} \\ T_{MG1_min} &\leq T_{MG1} \leq T_{MG1_max} \\ \omega_{MG2_min} &\leq \omega_{MG2} \leq \omega_{MG2_max} \\ T_{MG2_min} &\leq T_{MG2} \leq T_{MG2_max} \end{aligned} \quad (6.7)$$

These inequality constraints are implemented by assigning large penalty to control decisions that violate these constraints.

The SDP problem is solved through a policy iteration algorithm, which consists of a policy evaluation step and a policy improvement step (Howard, 1960). This algorithm is solved iteratively until the cost function J_π converges. In the policy evaluation step, given a desired power P_d , starting with an initial policy π , we calculate the corresponding cost function $J_\pi(x)$. Then a new policy is determined through the equation:

$$\pi(P_d) = \arg \min \left[g(x, u) + \gamma \sum_{x'} P_{xx'} J_\pi(x') \right] \quad (6.8)$$

After the new policy is obtained, we go back to the policy evaluation step to update the cost function by using the new policy. This process is repeated until J_π converges within a selected tolerance level. The control policy generated is time-invariant and causal and has the form of nonlinear full-state feedback laws (an example map is shown in Figure 6.6).

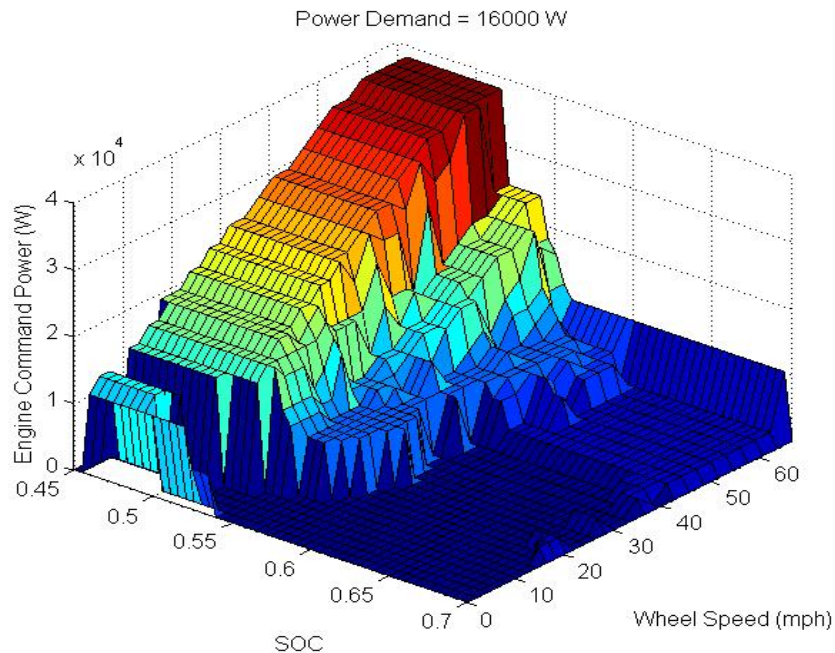


Figure 6.6: Example of optimized engine power map from SDP.

Similar to DDP, there is a significant trade-off between computation efficiency and accuracy. Besides applying the same numerical acceleration techniques explained in section 5.1.3, varying the state/input grid sizes greatly affects the optimization results. The optimization process in SDP is more computationally intensive than DDP because of the policy iteration algorithm. Fine grids will cause the computer to run out of memory. Rough grids may result in a control policy that is not accurate enough (An engine-in-the-loop study on the map accuracy effect is shown in Appendix D). One way to compensate such effect is to apply refined grids on the common driving conditions and rough grids on the rare cases. From the generated driving power and vehicle speed shown in Figure 6.7. Cases with relatively low vehicle speed and power happen more often than cases with relatively high vehicle speed and power. Therefore, to save computational cost, rough grids can be used when the power demand is high or the vehicle speed is high, while keeping fine grids for the rest of the cases.

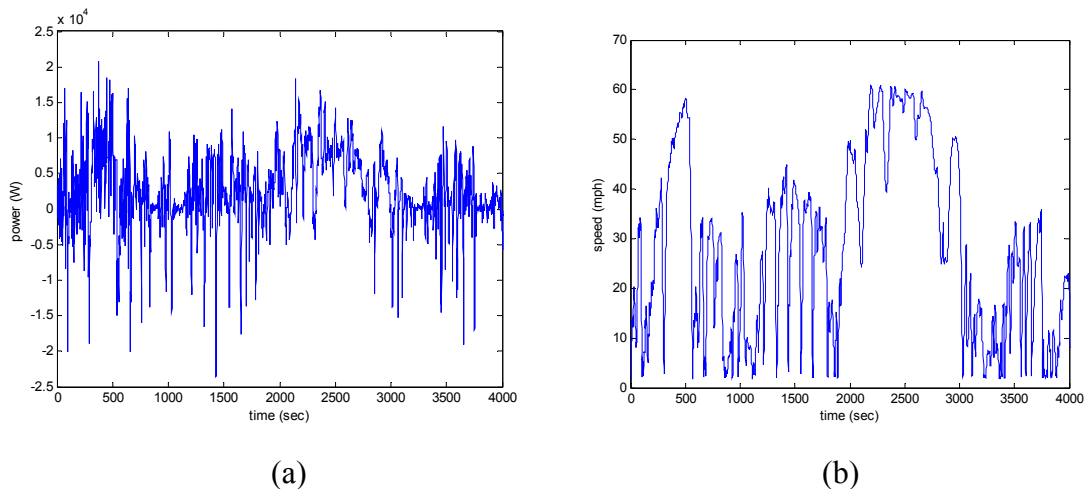


Figure 6.7: Calculated driving power (a) and vehicle speed (b) in the Markov chain model.

6.3. ECMS for Power-Split Hybrid Vehicles

The equivalent consumption minimization strategy (ECMS) is an instantaneous optimization algorithm introduced by Paganali et al. (2001). This ECMS is based on the idea that for charge-sustaining hybrid vehicles, the instantaneous (charging/discharging) usage of a reversible energy storage device will decrease/increase the future fuel use of the irreversible energy storage device. However, the conversion factor from electric energy to equivalent fuel use cannot be determined exactly because the future driving schedule is unknown. To compensate for this uncertainty effect, an average factor tuned over a certain driving cycle is used. In early designs, this approach assumed that every variation in the SOC would be compensated in the future by the engine running at the current operating point or an average point (Paganelli and Delprat et al., 2002; Paganelli and Guezennec et al., 2002). Sciarretta et al. (2004) presented a new solution based on a coherent definition of system self-sustainability. The driving power demand P_d is assumed to be always fulfilled by the engine power P_e and the electric machine power P_{elec} :

$$P_d = P_e + P_{elec} \quad (6.9)$$

When we are solving a power management problem for a hybrid vehicle, with the goal of minimizing fuel consumption, it is necessary to assign a cost for the electric machine power. Otherwise the optimization problem is not well posed. Given the fact that the battery SOC needs to be maintained at a proper level, P_{elec} is not “free” and can be assigned an equivalent fuel consumption cost:

$$\dot{m}_{f_total} = \dot{m}_{f_eng} + \dot{m}_{f_elec} \quad (6.10)$$

where \dot{m}_{f_eng} represents the fuel consumption of engine and \dot{m}_{f_elec} represents the equivalent fuel consumption of the electric machines, which can be calculated from:

$$\dot{m}_{f_elec} = \overline{FC} \cdot P_{elec} / \overline{\eta_{trans}} \quad (6.11)$$

where \overline{FC} is the estimated engine fuel consumption conversion factor. The average efficiency of battery, inverter, and motor/generator are considered by

$$\overline{\eta_{trans}} = \overline{\eta_{batt}} \cdot \overline{\eta_i} \cdot \overline{\eta_{MG}}.$$

Using (6.10), an approximated equivalent fuel consumption is obtained. The benefit of using this single conversion factor is that the fuel consumption can be estimated regardless of the speed and torque of the engine and the motor/generator. The drawback is that its accuracy is questionable when the driving cycle changes. Another major problem of (6.10) is that it does not include the battery SOC and electric machine into consideration. To achieve SOC regulation, a weighting factor $f(soc)$ was suggested in (6.12) by Paganali et al. (2002). As shown in Figure 6.8, $f(soc)$ sets the target SOC at around 0.6 and weighs the SOC away from this target value such that the equilibrium SOC is attractive.

$$\dot{m}_{f_total} = \dot{m}_{f_eng} + f(soc) \cdot \dot{m}_{f_elec} \quad (6.12)$$

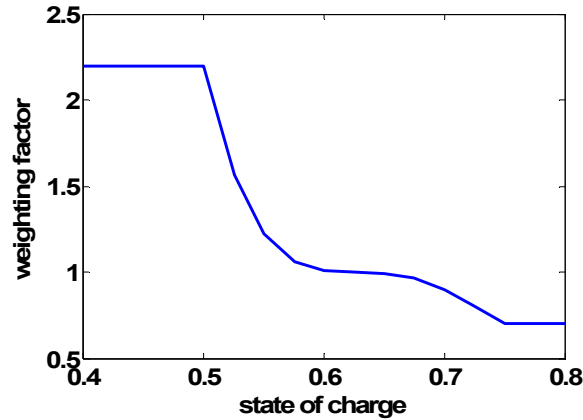


Figure 6.8: SOC weighting factor $f(soc)$ for the ECMS algorithm (Paganali et al. 2002).

The original ECMS algorithm does not consider kinematic constraints imposed by the electric machines. Kinematic constraints are more important in split hybrids because of the CVT nature of the power-split device. For example, by using parameters for the THS system, if the desired engine power is 20 kW , then the optimal engine speed is $\omega_{e_d} = 2333\text{ rpm}$ to achieve optimal efficiency. Due to the MG1 speed limit of 6500 rpm , the vehicle speed must be higher than 12.6 mph for the optimal engine speed to be realizable (Figure 6.9). At higher engine power demand, the optimal engine speed can be even higher, and the unreachable set imposed by the kinematic constraint grows even larger.

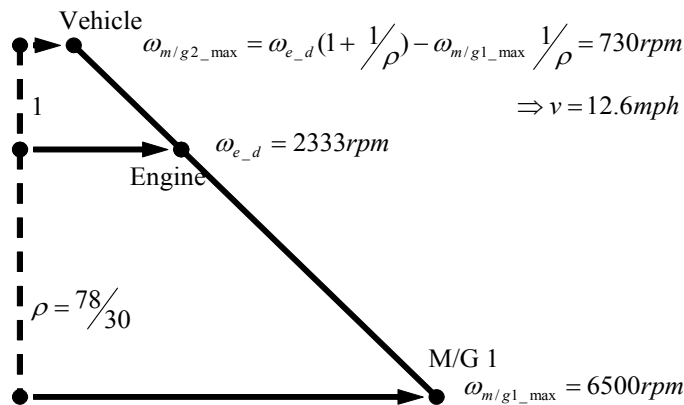


Figure 6.9: Speed constraint calculation in THS.

Because of the kinematic constraint, the feasible engine power is a function of power demand P_d and vehicle speed v (Liu and Peng, 2006). In other words, equation (6.10) is modified to:

$$\dot{m}_{f_equi} = \dot{m}_{f_eng}(v, P_d) + f(soc) \cdot \dot{m}_{f_batt} \quad (6.13)$$

With this equivalent consumption cost function, given a power demand P_d , the optimal engine power can be searched among all feasible values to achieve minimal weighted equivalent fuel consumption. Figure 6.10 shows the searching process for the condition with $P_d=30$ kW, $SOC=0.6$, and $v=16$ mph. The fourth plot shows the combined equivalent fuel consumption without considering the kinematic constraints. However, with the kinematic constraints, the engine can not operate in the shadowed region shown in the fifth plot, the optimal solution is hence on the boundary of the feasible region. Repeat this process for all states, the calculated optimal engine power map is determined offline for each vehicle speed, one example map is shown in Figure 6.11.

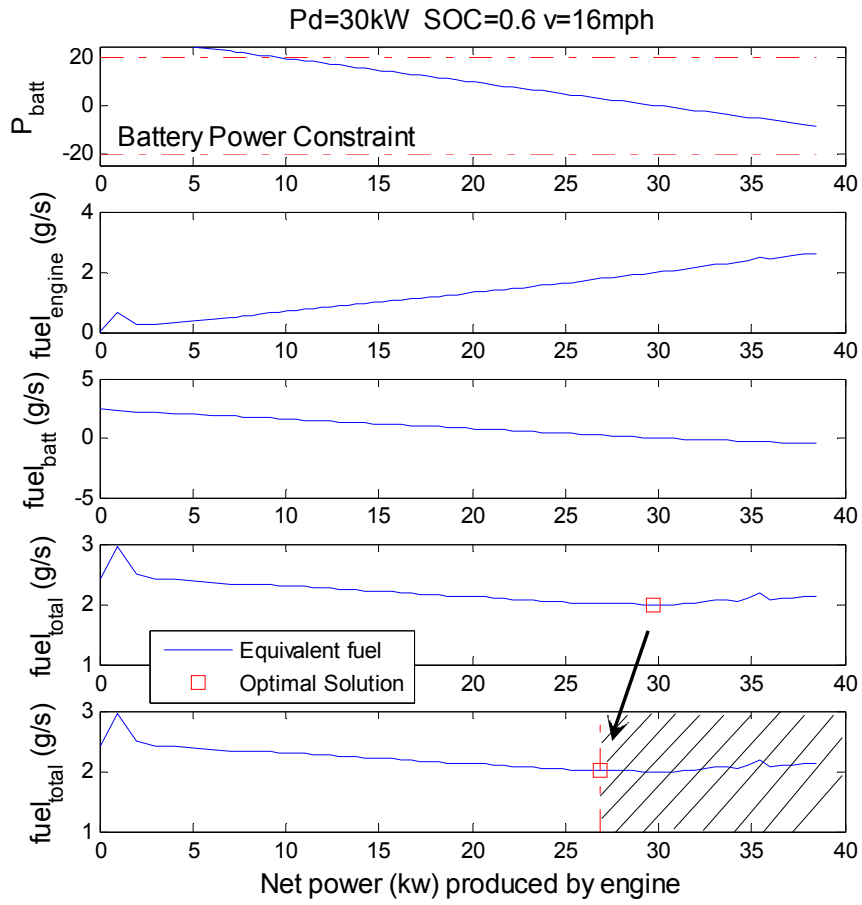


Figure 6.10: Optimal solution searching process for the ECMS algorithm.

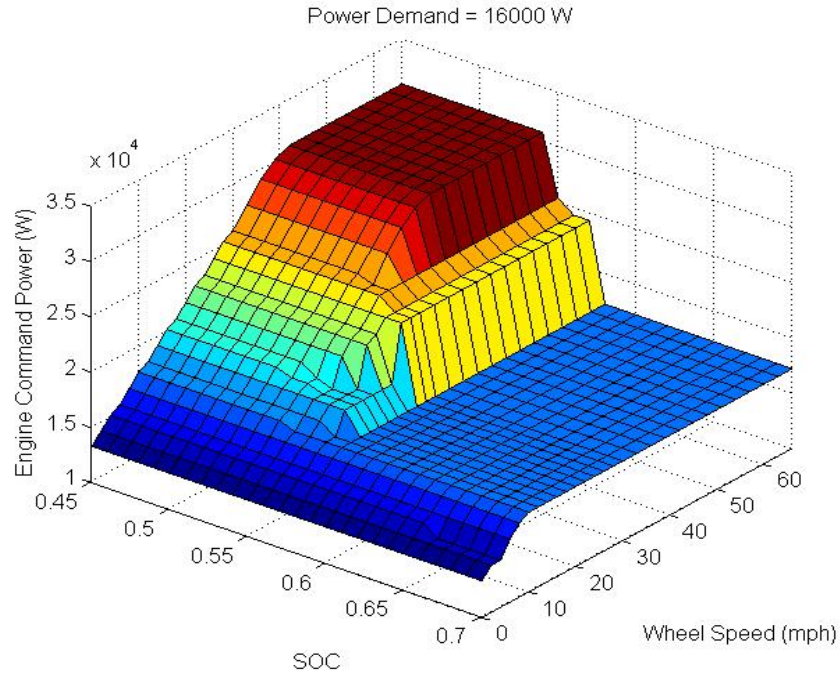


Figure 6.11: Example optimized engine power map from ECMS.

6.4. Result and Discussion

Simulations of the same vehicle model with SDP and ECMS controllers are conducted under various driving cycles to evaluate the control performances. The SOC-corrected fuel economy results of the three control algorithms are presented in Table 6.1. The results using the rule-based control algorithm (explained in section 2.4) are also reported for comparison. Both the SDP and ECMS algorithms show significant fuel economy improvement and both are close to the optimal results produced by DDP. Results seem to validate that the SDP approach and the ECMS approach are near-optimal and are good candidates for practical implementation.

Table 6.1: Fuel economy comparison between different control algorithms.

Vehicle	Driving Cycle	Rule-Based Control (mpg)	SDP Control (mpg)	ECMS Control (mpg)	DDP Benchmark (mpg)
THS Configuration Prius	Highway	57	65	64	67
	City	54	57	56	57
PT2 Selected Configuration HMMWV	Highway	17	20	20	21
	City	15	18	16.5	18.5

High overall fuel efficiency is only possible with excellent engine efficiency. To examine the instantaneous engine performance, the engine operating points for both SDP and ECMS approaches are shown in the engine brake specific fuel consumption (BSFC) maps in Figure 6.12. The total point densities are highlighted in different colors. The contours of equi-BSFC lines show the relative fuel efficiency of the operating points. In addition, the most efficient points for given engine power is shown by the red dashed line. Close examination of this figure confirms the engine operates very close to the theoretical optimal points, probably through utilization of the electric machines.

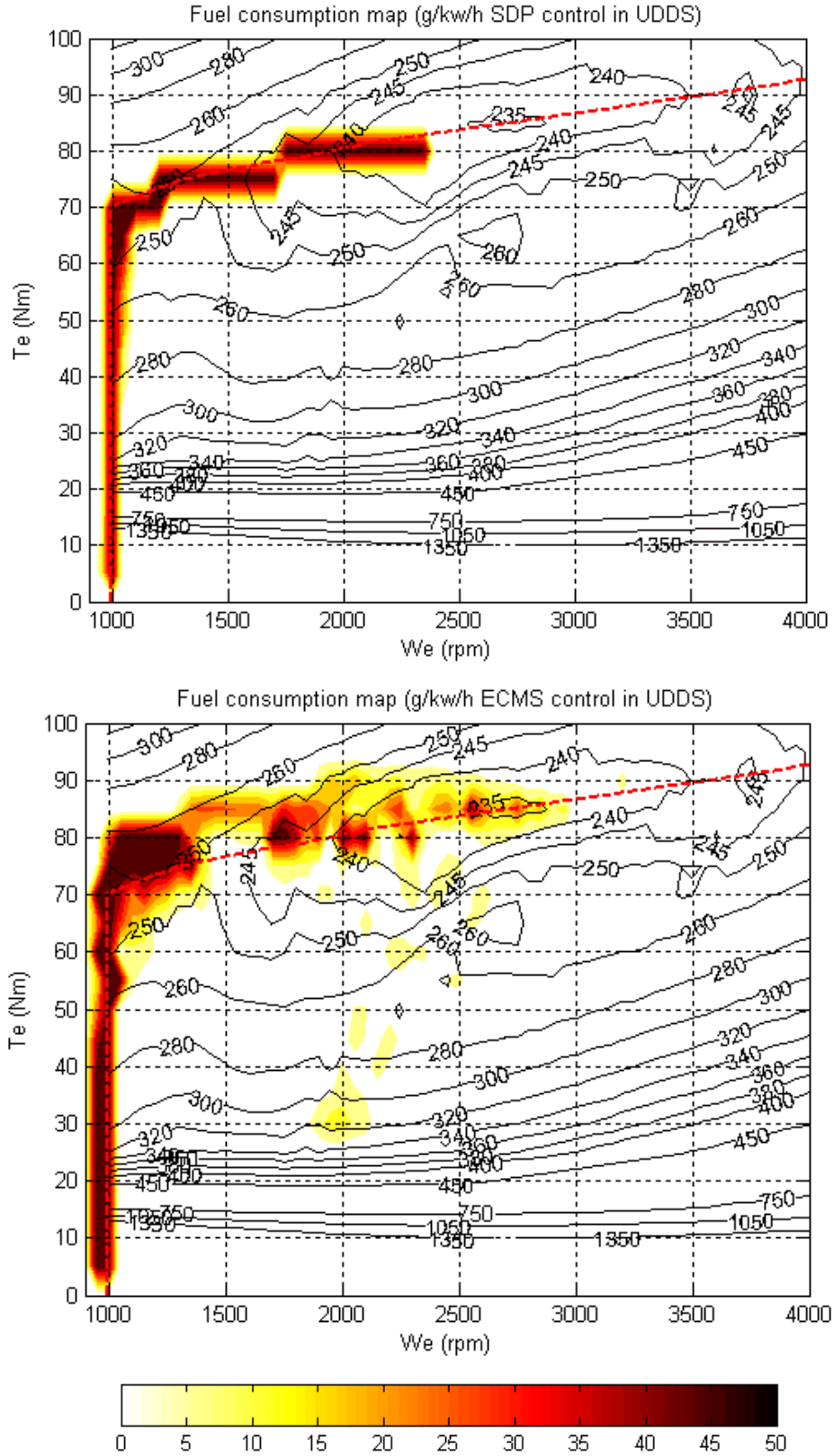


Figure 6.12: The engine operating point densities for both SDP and ECMS approaches in FTP75 cycle. (Sampling: 1Hz).

Despite of the similarities, the distributions of the engine operating points shown in Figure 6.12 also have noticeable differences. The engine power traces, commanded by DDP, SDP, and ECMS algorithms during a vehicle launch are plotted in Figure 6.13. It can be seen that the engine power commanded by the ECMS oscillates continuously. This is partly due to the fact the best engine efficiency is obtained with relatively high engine power (as shown in Figure 6.12). When the power demand is low, the instantaneous optimization algorithm tends to move the engine toward a more efficient point, which generates more power than demanded. The extra power delivered is balanced by the electrical path and the excessive energy is stored in the battery. This saved energy is then used to assist engine operation, allowing the engine to generate less power than required by the vehicle load. This results in the wide-varying engine power, which is also responsible for the scattered engine power generation shown in Figure 6.12. The engine power generated by the SDP algorithm, in comparison, is a lot smoother. Since the SDP strategy is obtained based on infinite-horizon optimization, the future is taken into consideration, albeit in a stochastic way. Due to the longer optimization horizon, the SDP results do not react to instantaneous condition excessively.

The DDP power flow presented in Figure 6.13 is used to evaluate the power decisions made by the two control strategies. It shows an attempt similar to ECMS during the vehicle launch when the vehicle speed is low, but is much smoother for the rest of the sample cycle. The SDP approach produces smoother power compared with ECMS, which is desirable from the drivability viewpoint. The fuel consumptions of these two algorithms, however, are similar. Based on our experience, SDP would be a better

algorithm to use, because the smooth operation is desirable for transient emission performance.

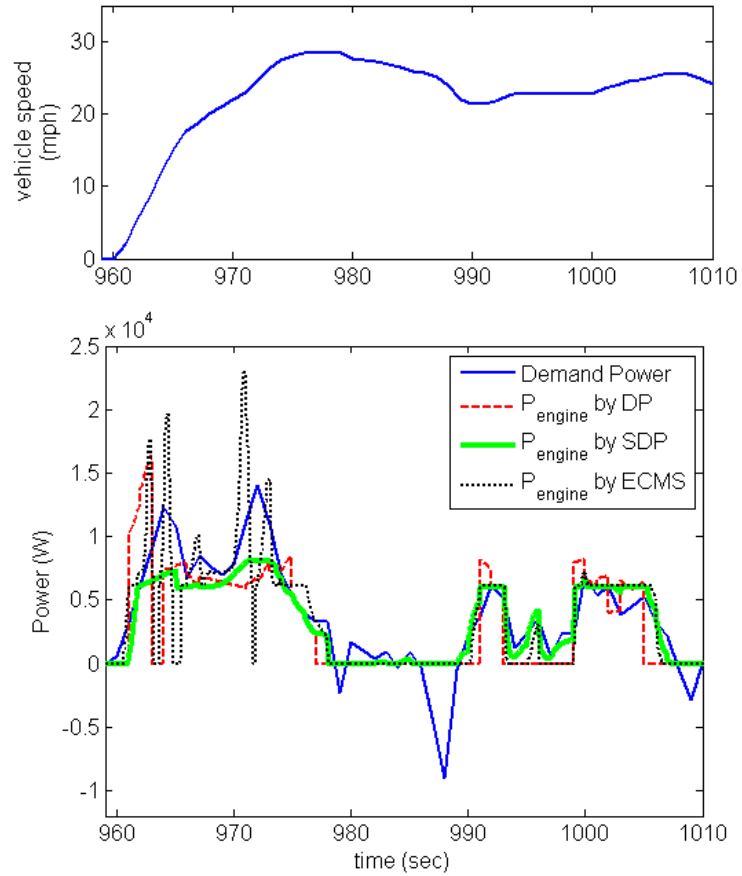


Figure 6.13: Engine power by DDP, SDP and ECMS algorithms during a vehicle launch.

CHAPTER 7

CONCLUSION AND FUTURE WORK

7.1. Conclusion

In this dissertation, the design and control analysis of power-split HEV powertrains was presented. The main objective was to establish a systematic approach for combining optimal design (configuration and component selection) and optimal control (full exploration of the potential of the components) in power-split hybrid vehicle applications to improve system efficiency and to reduce fuel consumption.

An integrated, dynamic simulation model was developed for power-split hybrid electric powertrain systems in Chapter 2. This simulation tool enables us to analyze the interaction between sub-systems and evaluate vehicle performance using measures such as fuel economy and drivability. It is also suitable for studying component-sizing and vehicle-performance limitations. Based on this simulation tool, a universal model format is proposed in Chapter 3. It presents different designs of power-split powertrains regardless of the various connections of engine-to-gear, motor-to-gear, or clutch-to-gear. With such a format, a technique to quickly and automatically generate dynamic models for the split-type hybrid powertrain was developed. This technique automates the process from powertrain design to dynamic model and makes it possible to explore and evaluate many different configurations.

With the help of the automated dynamic models, possible configuration designs can be systematically explored. A design screening process was suggested in Chapter 4 based on various design requirements including feasibility, drivability, power source component sizing, transmission efficiency, and possible mode shifting. This process was applied to design a 2-PG dual-mode power-split powertrain system in a case study. 1152 possible design candidates were automatically generated and analyzed. With severe size limitations on the electric machines, only 2 of them were concluded as proper design candidates that satisfy all design objectives.

In Chapter 5, a control design procedure based on deterministic dynamic programming (DDP) was employed to find the optimal operation of the power-split system and achieve the performance benchmarks for different configuration candidates. These benchmarks were applied to compare and evaluate different designs, which then led to the optimal solution. This approach provides design engineers with fast, quantitative analysis and further understanding of the power-split hybrid powertrain systems.

With the DDP suggesting the potential performance benchmark of the selected powertrain configuration, two implementable control strategies were developed to approach this performance benchmark in Chapter 6. The first design was based on the stochastic dynamic programming (SDP), which solved the power management problem on an infinite horizon. The driver power demand was modeled stochastically, which reflected the fact that the optimization was not for any specified driving cycle but rather for general driving conditions with known power demand probabilities. The second control design was developed from the equivalent consumption minimization strategy

(ECMS), which was based on an instantaneous optimization concept. The configuration of the power-split system enforced more constraints to the control strategy. Although both of these two optimal control designs show close agreement with the DDP fuel economy results, SDP is a preferred algorithm because its smoother operation is more desirable than ECMS.

The modeling, design, and control optimization procedure presented in this dissertation provides a powerful tool for vehicle engineers to make critical choices such as powertrain configuration, component sizing, and power management control design of the split-type hybrid vehicles.

7.2. Future Work

Some potential future directions that merit further study are listed as follows:

- As demonstrated in Chapter 4, a 2-PG power-split powertrain has 1152 possible configurations. This number increases dramatically when searching 3-PG possible solutions. Moreover, a 3-PG powertrain configuration can have more than two operating modes, which include input-split mode, compound-split mode, and fixed gear mode(s) (Grewe et al., 2007). The searching and screening process can be extended to investigate 3-PG powertrain systems. In the 3 steps proposed in Chapter 4, the methods of justifying a feasible configuration, considering drivability requirement, and analyzing transmission efficiency can still be applied. The method of checking shifting mode(s) needs to be modified to cover more possibilities.
- Although the power-split hybrid powertrains discussed in this dissertation are assumed to have only 2 degrees of freedom (DOF), it is not necessary that all the possible configurations constructed by planetary gear sets are limited to have 2 DOF. As

described in section 3.1, a single PG has 2 DOF. The combination of several PGs can form a powertrain system with 3 or more DOF. The node that represents the extra freedom must be controlled by extra electric machine(s). Otherwise the operation of the system becomes uncertain. The automated modeling process introduced in this dissertation needs to be modified to cover the cases with more than 2 DOF. The screening process becomes more complex since more design possibilities need to be considered.

- The control strategies discussed in this dissertation can be modified to investigate hybrid vehicle powertrain systems with extended control design objectives. Emission, as an example, is another important measure for hybrid vehicle control. To add the emission constraints in the control, in DDP or SDP, the cost function can be changed to have weighted emission associated terms. The compromise between fuel consumption and emission needs to be achieved by tuning the weighting factors. In ECMS, equivalent fuel consumption cost regarding the emission can be estimated to penalize the engine usage. The simulation model to study emission has higher order than the simulation model used in this study. The excessive search in DDP and SDP may cause computational problem. Approximating DP results by using linear programming could reduce the problem size and may provide a practical solution (Schweitzer and Seidmann, 1985).

APPENDICES

APPENDIX A
NOMENCLATURE

ADVISOR	Advanced Vehicle Simulator
AHS	Allison Hybrid System
BSFC	Brake Specific Fuel Consumption
CAFE	Corporate Average Fuel Economy
CL	Clutch
CPG	Compound Planetary Gear
CVT	Continuously Variable Transmission
DC	Direct Current
DOE	Department of Energy
DOF	Degree of Freedom
DDP	Deterministic Dynamic Programming
DP	Dynamic Programming
ECMS	Equivalent Consumption Minimization Strategy
ECVT	Electric Continuously Variable Transmission
EPA	Environment Protection Agency
HEV	Hybrid Electric Vehicle
HMMWV	High Mobility Multipurpose Wheeled Vehicle
ICE	Internal Combustion Engine
MG	Motor/Generator
MP	Mechanical Point
NHTSA	National Highway Traffic Safety Administration
PG	Planetary Gear
PM	Particulate Matter
PT	Powertrain

PSAT	PNGV System Analysis Toolkit
PNGV	Partnership for a New Generation Vehicles
SDP	Stochastic Dynamic Programming
SOC	State of Charge
SQP	Sequential Quadratic Programming
THS	Toyota Hybrid System

APPENDIX B

POWER-SPLIT SYSTEM EFFICIENCY ANALYSIS

The efficiency of the ECVT transmission, which is heavily influenced by the planetary gear (PG) systems maneuvered by the controlled electric machines, plays an important role of the overall efficiency of a power-split hybrid vehicle. The efficiency of ECVT is a combination of electrical path efficiency and mechanical path efficiency because of its hybrid nature. Because the efficiency through the electrical path is typically less than that of the mechanical path, the power-split ratio between these two affects the overall efficiency. The following analysis offers design guidance regarding this issue.

The lever diagram is again used to represent the PG system. For an ECVT, the lever can be drawn with point 0 at the output shaft and point 1 at the input shaft. Then the length of the lever, which may be positive or negative, determines the kinematic relationship of the electric machine to the input and output shafts. In this analysis, parameters α and β will represent the lever lengths of the MG1 and MG2 shaft (Conlon, 2005), as shown in Figure B.1. Note that a lever length of one represents a motor that is connected directly to the input power path, and a zero represents a motor that is directly connected to the output power path. In addition, on each node, there is a speed gain K_i that represents the extra speed ratio between the power sources or vehicle and the power-split lever. The additional gain can result from a PG meant to provide additional torque

multiplication or a series of linked spur gears. For most of the cases, these gains are equal to one because of direct connections.

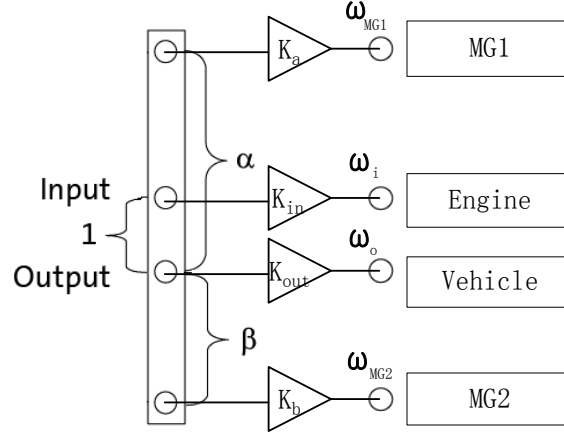


Figure B.1: General power-split ECVT lever diagram.

With this convention, lever kinematics in equation (2.1) becomes

$$\frac{\omega_{MG1}}{K_a} + (\alpha - 1) \frac{\omega_o}{K_{out}} = \alpha \frac{\omega_i}{K_{in}} \quad (\text{B.1})$$

Now if define $R_{ia} = \frac{K_{in}}{K_a}$ $R_{ib} = \frac{K_{in}}{K_b}$ $R_{oa} = \frac{K_a}{K_{out}}$ $R_{ob} = \frac{K_b}{K_{out}}$, (B.1) can be expressed as

$$\omega_{MG1} = \frac{\alpha}{R_{ia}} \omega_i + (1 - \alpha) R_{oa} \omega_o \quad (\text{B.2})$$

Similarly for the other node that is connected to the electric machine,

$$\omega_{MG2} = \frac{\beta}{R_{ib}} \omega_i + (1 - \beta) R_{ob} \omega_o \quad (\text{B.3})$$

Because of the power conservation, if we only consider the power from the engine at the input node, the torque equation derived in (2.7) at the steady state can be rewritten as

$$\begin{aligned}
T_i &= -\frac{\alpha}{R_{ia}} T_{MG1} - \frac{\beta}{R_{ib}} T_{MG2} \\
T_o &= (1-\alpha)R_{oa} T_{MG1} + (1-\beta)R_{ob} T_{MG2}
\end{aligned} \tag{B.4}$$

These speed and torque relations (B.2)-(B.4) will be used to study the efficiency of the input-split and the compound-split systems. The output-split case is not discussed because of its limited usage for ground vehicles (Conlon, 2005).

B.1. Input-Split System

The input-split system is defined as the case when one of the electric machines is connected to the output shaft. In this case, the engine power is split into two paths, one of which goes directly to the final drive through the electrical path, the other part is generated as electricity by one of the MGs and power the other MG to assist the driving torque. It can be seen that an input-split is characterized by a set of parameters where either α or β is zero.

To compare the performance of different configurations, it is useful to use normalized input and output torques and speeds, where a value of one is equal to the engine torque or engine speed. Assume $\beta=0$ and substitute it into (B.2)-(B.4), the normalized electric machine speeds, torques, and powers can then be plotted against the transmission gear ratio (relative to mechanical point). Here the mechanical point (MP) is defined as the input/output speed ratio where the MG1 speed is zero.

Figure B.2 and Figure B.3 show MG1 and MG2 torque, speed, and power plotted vs. relative transmission ratio, for various values of α (note: $\beta=0$). It can be seen that the input-split configuration has only one MP. The MP is always at the same transmission ratio (point 1 in the figures). If the system is kept operating close to the MP, increased

engine speed pushes the output speed beyond a useful range. While the input-split is capable of infinite ratio spread similar to a CVT, the ratio, at which the engine can be run at full speed (toward the right hand side of each figure) and power, will be limited by MG1 speed, MG2 torque, or the electric power circulated through them. A usable ratio range can be defined as a ratio range from the mechanical point up to the point at which the input split can no longer operate at full input speed and torque. This ratio range typically is up to 4 times of the MP (As highlighted by the dash-dot line in Figure B.2 and Figure B.3), where at the expense of a high fraction of power through the electrical path (75%), high MG1 speed (2-3 times input speed for typical values of α), and high MG2 torque. Notice as electric power increases, the overall ECVT efficiency drops. The operating range close to the MP has the highest efficiency values since most of the power flow through the mechanical path.

Take THS as an example for the single-mode input-split system. Given that the sun gear has 30 teeth and the ring gear has 78 teeth (Hermance, 1999), its α value can be calculated as

$$\alpha = \frac{30+78}{30} = 3.6 \quad (\text{B.5})$$

The performances of its speed and torque are close to the case of $\alpha=4$ in Figure B.2 and Figure B.3. This system has stringent constraints on both electric machines when the input/output speed ratio is high, i.e., when the vehicle is launched with high power demand (to the right in Figure B.2 and Figure B.3). The speed of MG1 and the torque of MG2 become very high as input/output ratio increases. As a result, THS requires a large torque launching motor (MG2) and a high speed range operating generator (MG1).

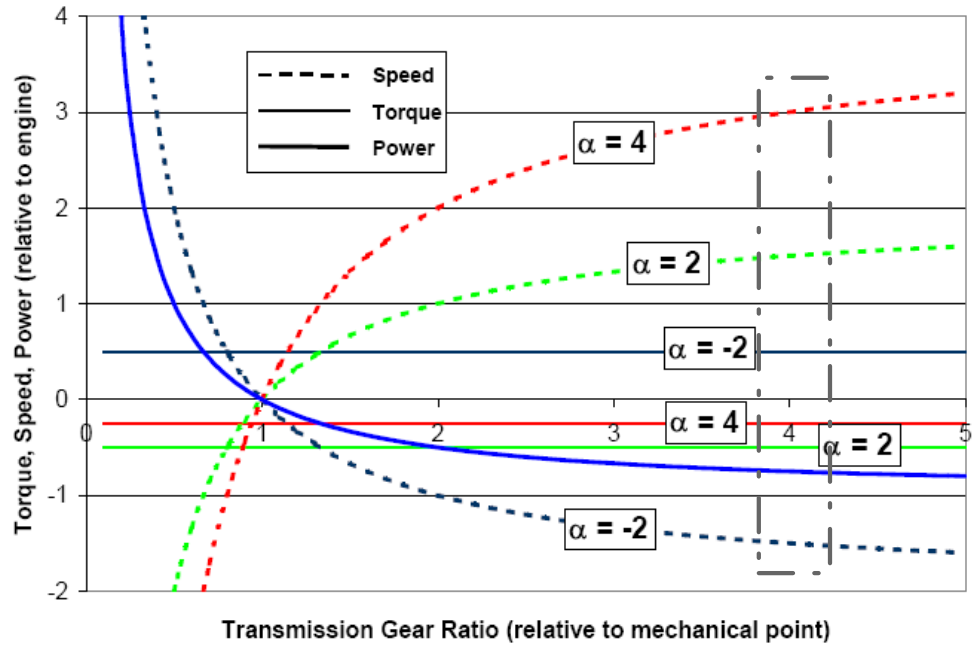


Figure B.2: Relative speed, torque, and power of the MG1 in input-split system.

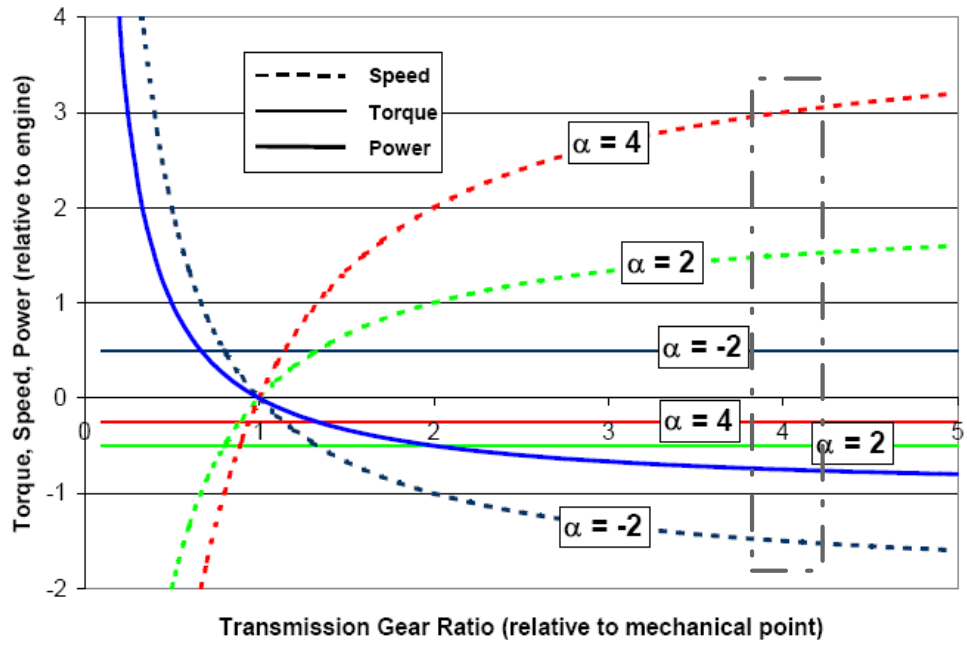


Figure B.3: Relative speed, torque, and power of the MG2 in input-split system.

B.2. Compound-Split System

The compound-split system is defined as the case when both electric machines are not connected directly with the input or output node. In this system, the engine power splits into two paths similar to an input-split system, but then these two different power flows combine through another split ratio, typically realized through another planetary gear set. Based on this definition, in a compound-split system, both α and β are not equal to zero or one.

Figure B.4 and Figure B.5 show the relative speed, torque, and power of both MGs of the compound-split system with various typical α and β values. It can be seen that there are two MPs in a compound-split system. Note that in the region between the two MPs, the electric power flow peaks at a low fraction of the engine power, which is beneficial for the overall ECVT efficiency. However, the sharp increase in power outside of this region limits the operation to near the mechanical points. It is also reflected in both figures that within the operating region between the two MPs, the speed and torque of the electric machines do not vary significantly. As a result, the compound-split system can be used as a supplemental system that provides an operating region between the two MPs that have high efficiency.

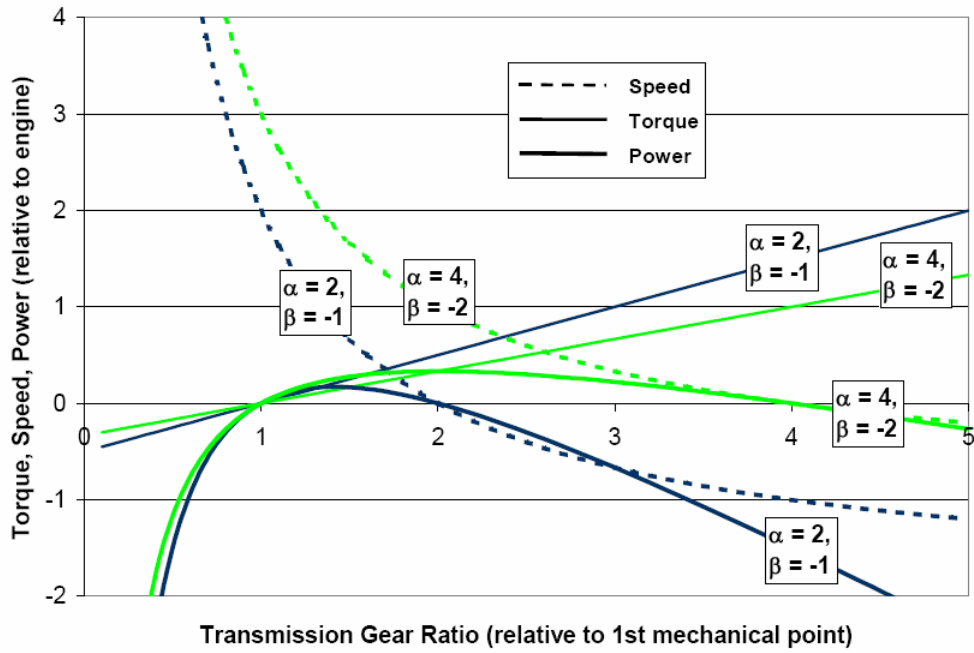


Figure B.4: Relative speed, torque, and power of the MG1 in compound-split system.

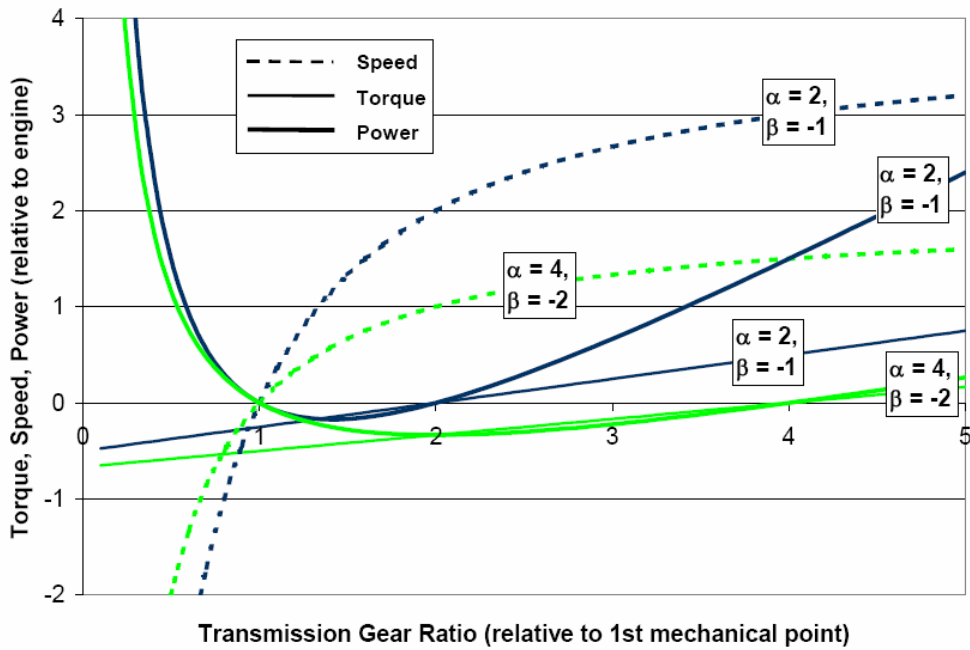


Figure B.5: Relative speed, torque, and power of the MG2 in compound-split system.

B.3. Dual-Mode System

The selection of transmission ratio for a practical vehicle needs to consider a wide range of operating conditions. When the vehicle is full-power launching, the vehicle speed is very low and the engine speed is normally high due to the high power request. When the vehicle is cruising on a highway, the vehicle speed is high but the engine speed is relatively low due to the low power request. As a result, the MP design of the power-split ECVT needs to consider the efficiency of both.

The input-split system and compound-split system both have critical limitations regarding operating the vehicle efficiently. For an input-split system, the choice of the ratio for the single mechanical point is a compromise between transmission efficiency and electric machine capacity. If the MP is chosen for an input/output ratio suitable for full-power vehicle launching with high engine speeds, it hurts the highway fuel economy due to the high portion of electric circulation power during cruising. If the MP is chosen for an input/output ratio suitable for vehicle cruising with low engine speed, it requires large electric machine with very high peak power when launching the vehicle (Explained in THS example in section B.1). For a compound-split system, although it has two MPs that can be placed for both launching and cruising driving scenarios, its usage for launching is very limited because of the sharp efficiency drop outside of the region between the two MPs. In other words, the compound-split system can not handle the cases with very high ratio between input and output speeds (i.e., when the vehicle speed is low and engine speed is high).

The need for the highest efficiency for both high power launching and highway cruising, along with moderate size, weight, and cost for the electric machines, lead to the combination of the input-split and compound-split systems. At low vehicle speeds or for

high acceleration rates, an input-split mode is utilized with a mechanical point with high input/output ratio. The compound gear set splits the input power, and the second planetary gear set provides additional torque multiplication. Since one electric machine is connected to the output shaft, or final drive, directly, the electric launching without engine input can also be achieved. At higher vehicle speeds or lighter loads, the system can operate in a compound-split mode with the MP range covering the whole cruising speed region. The transition between the two modes occurs synchronously at a set gear ratio (refer to the explanation in Section 2.3.2). This combination of an input and compound-split also reduces electric machine maximum speeds.

APPENDIX C

DESIGN EVALUATION RESULTS

Table C.1: DDP results for different gear dimensions and MG sizing on PT1.

Fuel Economy (mpg)	$K_1=1.6$	1.8	2.0	2.2	2.4
MG1 is 10 kW and MG2 is 50 kW					
$K_2=1.6$	15.63	N/A	N/A	N/A	N/A
1.8	15.82	N/A	N/A	N/A	N/A
2.0	16.00	N/A	N/A	N/A	N/A
2.2	N/A	N/A	N/A	N/A	N/A
2.4	N/A	N/A	N/A	N/A	N/A
MG1 is 20 kW and MG2 is 40 kW					
$K_2=1.6$	17.40	16.82	16.38	15.99	N/A
1.8	17.74	16.86	14.59	15.81	15.70
2.0	17.53	17.07	N/A	N/A	N/A
2.2	17.26	16.99	15.48	N/A	N/A
2.4	16.71	16.03	N/A	N/A	N/A
MG1 is 30 kW and MG2 is 30 kW					
$K_2=1.6$	17.34	17.18	16.88	15.85	16.34
1.8	17.47	17.32	16.31	15.88	16.26

2.0	17.43	17.30	16.12	15.95	15.76
2.2	17.52	16.41	15.85	15.56	14.67
2.4	17.26	16.51	14.05	N/A	N/A
MG1 is 40 kW and MG2 is 20 kW					
$K_2=1.6$	16.98	16.85	16.04	15.75	16.17
1.8	17.06	16.69	16.60	16.10	15.79
2.0	17.03	16.29	16.06	16.92	14.83
2.2	16.99	16.20	15.94	15.24	N/A
2.4	16.76	15.93	15.64	N/A	N/A
MG1 is 50 kW and MG2 is 10 kW					
$K_2=1.6$	N/A	N/A	N/A	N/A	N/A
1.8	N/A	N/A	N/A	N/A	N/A
2.0	16.28	15.83	15.56	N/A	N/A
2.2	16.10	N/A	N/A	N/A	N/A
2.4	N/A	N/A	N/A	N/A	N/A

N/A: This configuration variation can not satisfy the driving demand with some of the constraints violated.

Table C.2: DDP results for different gear dimensions and MG sizing on PT2.

Fuel Economy (mpg)	$K_1=1.6$	1.8	2.0	2.2	2.4
MG1 is 10 kW and MG2 is 50 kW					
$K_2=1.6$	15.62	15.16	N/A	N/A	N/A
1.8	15.58	15.68	15.47	15.59	15.13
2.0	16.39	15.75	15.86	16.17	15.70
2.2	16.41	16.29	15.82	16.11	16.05

2.4	17.22	15.90	15.73	16.03	15.93
MG1 is 20 kW and MG2 is 40 kW					
$K_2=1.6$	17.58	18.03	17.67	17.57	17.33
1.8	18.17	18.23	18.20	17.78	17.82
2.0	18.36	18.25	18.29	18.01	17.69
2.2	18.43	18.54	18.18	18.06	17.93
2.4	18.53	18.43	18.35	18.02	18.09
MG1 is 30 kW and MG2 is 30 kW					
$K_2=1.6$	17.46	17.73	17.64	17.48	17.23
1.8	17.86	17.87	17.71	17.64	17.55
2.0	17.96	18.15	17.82	17.75	17.46
2.2	18.16	18.13	17.89	17.85	17.62
2.4	18.08	18.15	17.91	17.81	17.33
MG1 is 40 kW and MG2 is 20 kW					
$K_2=1.6$	16.31	17.12	16.83	16.12	N/A
1.8	16.44	17.20	17.07	16.13	N/A
2.0	16.73	17.58	17.27	16.29	N/A
2.2	16.82	17.58	17.30	16.50	N/A
2.4	16.79	17.76	17.42	16.46	N/A
MG1 is 50 kW and MG2 is 10 kW					
$K_2=1.6$	N/A	N/A	N/A	N/A	N/A
1.8	N/A	N/A	N/A	N/A	N/A
2.0	N/A	N/A	N/A	N/A	N/A
2.2	N/A	N/A	N/A	N/A	N/A
2.4	N/A	N/A	N/A	N/A	N/A

N/A: This configuration variation can not satisfy the driving demand with some of the constraints violated.

APPENDIX D

ENGINE-IN-THE-LOOP STUDY ON MAP ACCURACY EFFECT OF SDP

A parallel hybrid-electric configuration with a post-transmission motor location is modeled for an engine-in-the-loop (EIL) study. The virtual simulation and real engine are coupled in a dynamometer test cell through a Matlab/SIMULINK interface. Using the virtual driveline/vehicle simulation enables rapid prototyping of hybrid systems and optimization of the control systems. Using the complete engine system in physical hardware captures the effect of uncertainties in actuator response on engine dynamic behavior and brings transient emissions and visual signature into the controller design.

The integration of the virtual components with the hardware in the test cell to create an engine-in-the-loop system is represented schematically in Figure D.1. An advanced test cell, featuring a state-of-the art medium duty diesel engine and a highly dynamic AC dynamometer with the accompanying control system, has been set up specifically for investigations of clean diesel technologies in combination with advanced propulsion systems (Filipi et al., 2006). The dynamometer and test cell hardware vendor (AVL North America) provided the necessary hardware and software for interfacing models in SIMULINK with the dynamometer and engine controller. This opened up the possibility of realizing the full benefit of the synergy between advanced modeling and experimental efforts. The engine module has been literally removed from the simulation model, and the input/output links were connected to the interface instead. Simulated

forward-looking driveline and vehicle dynamics models make it possible to integrate a virtual driver into the system with the vehicle driving schedule as the only input to the EIL models. In case of the hybrid propulsion, the power management module receives the command from the driver, makes a decision about the power distribution between the two sources (engine and electric motor/generator) and sends the appropriate signals to the real engine and a virtual electric motor.

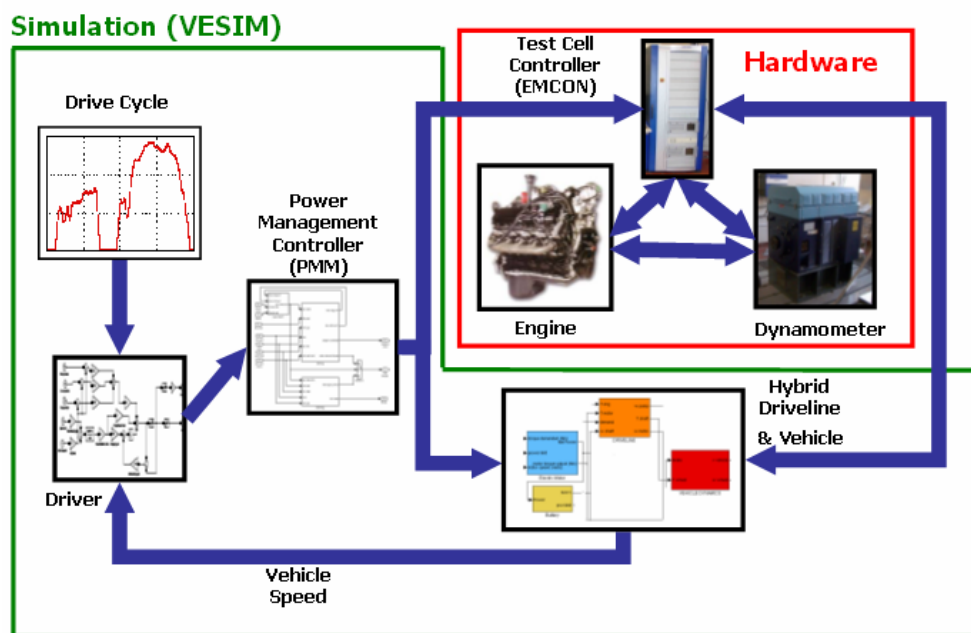


Figure D.1: Engine-in-the-loop setup for studies of the parallel hybrid electric propulsion.

An FTP75 driving cycle is chosen as the vehicle reference speed for simulation and EIL studies. Figure D.2 shows the initial segment of the driving cycle and confirms that the vehicle is able to follow the cycle precisely during both virtual and experimental runs. The power demand signals from the cyber driver, together with the battery SOC and vehicle speed, feed to the power management control designed by the SDP to determine power commands to the engine and the motor. The engine is then controlled to fulfil this

power request, and the EIL experiment allows replacing the engine model with the real diesel engine hardware in the test cell.

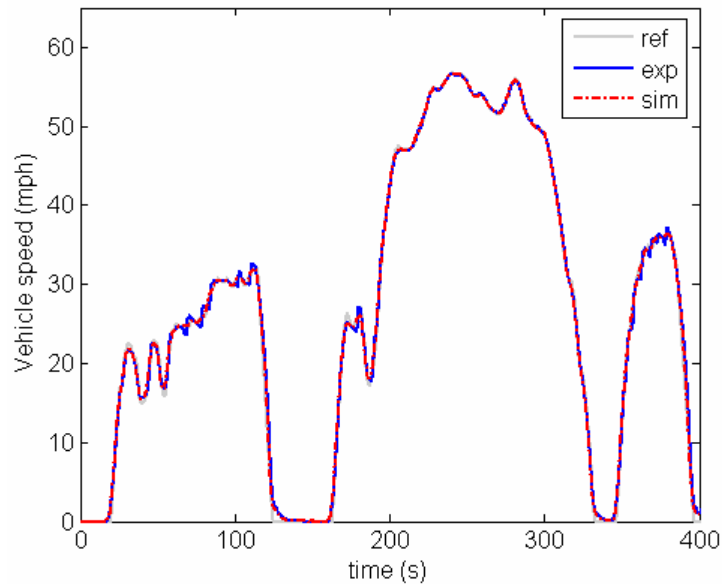


Figure D.2: The beginning part of the FTP75 reference driving schedule compared with simulation and experiment results.

A control policy is generated through the SDP method based on the simulation model. The simulation results indicated very tangible benefits in fuel economy, with relatively regular behavior of the cyber driver. However, when the same control policy was tested through the EIL experiment, the engine frequently switched between *on* and *off* states. Figure D.3 compares simulated and measured engine speed and torque histories obtained with the initial control design. The experimental engine speed/load transients obtained in the EIL setup differ markedly from the predictions. Experimentally measured traces display much higher amplitudes of transient spikes. The differences are most prominent in case of engine torque, as Figure D.3b shows measured high frequency fluctuation during periods of smooth operation of the virtual engine. The reason for such differences was found only after a close examination of the cyber drive behavior. If we

focus on the engine control from 39 to 47 seconds, during which a sudden engine power request is demanded (see Figure D.4a), the simulation result shows a corresponding throttle command increase at around 42 seconds. The simulated engine is able to fulfill the request and the throttle command displays a smooth profile throughout the rest of the interval. In contrast, the response of the real engine, equipped with real actuators, lags slightly; the cyber driver senses the torque deficiency and presses on the pedal harder eventually reaching 100%. The high-rate of increasing the engine command is due to the sharp slopes in control maps, as shown in Figure D.5a. Therefore, the cause of instabilities has ultimately been traced back to rough estimated state grids used in the controller design process, resulting in a rough control feedback map.

A more sophisticated controller is designed using refined state grids, and Figure D.5 shows the comparison between the old and the new. The state-feedback map generated with the refined SDP control (Figure D.5b) is much smoother than the original design (Figure D.5a). When this new supervisory controller is implemented in the EIL setups' virtual system, the sharp fluctuations of engine command disappear and experimental trace starts to follow the simulated trace very closely, as shown in Figure D.4b. As a result, the engine speeds and torques measured with a refined controller are closer to the simulation results (see Figure D.6b).

Overall, comparison of the engine performance in Figure D.3 and Figure D.6 (original vs. refined controller), shows much better agreement between the simulated and measured quantities with the refined, more accurate controller, and a remarkable reduction of measured transient torque spikes. Interestingly, the simulation results (solid

lines) for both control designs are very similar, and only after the controller is tested in the loop with real hardware its true dynamics become apparent.

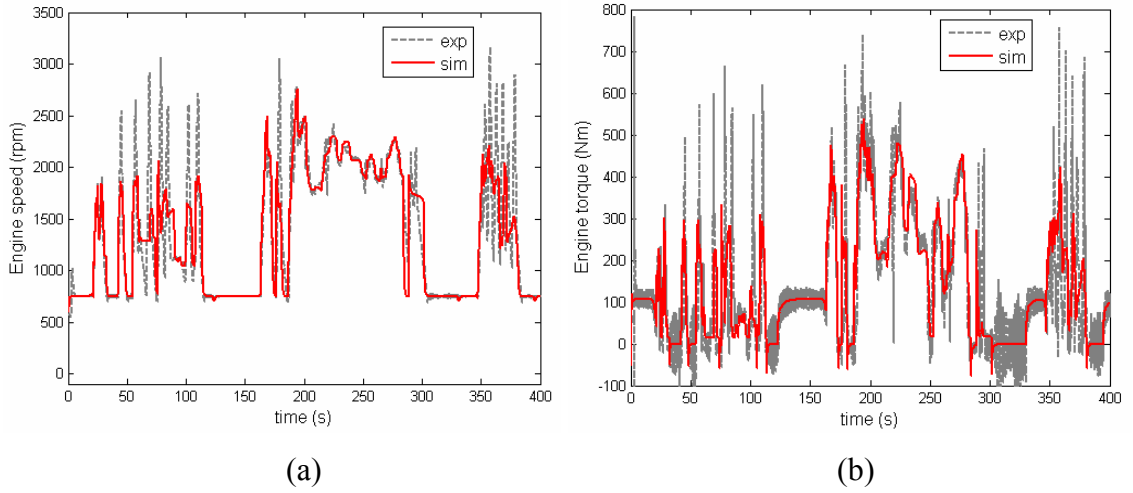


Figure D.3: Comparison of engine throttle commands between (a) the initial control design and (b) the refined control design (right).

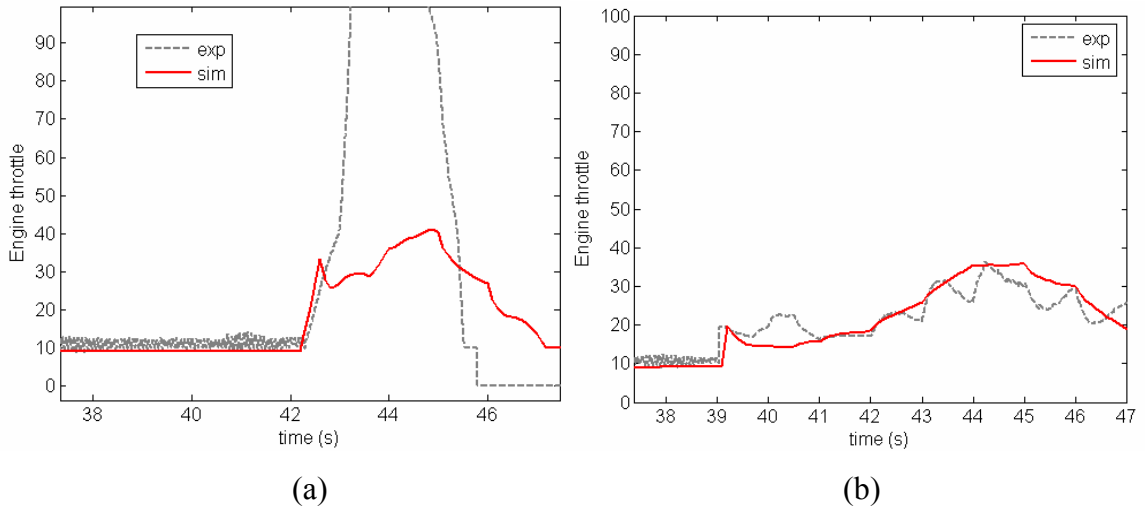


Figure D.4: Comparison of (a) engine speed and (b) engine torque results between simulation and experiment with an initial control design.

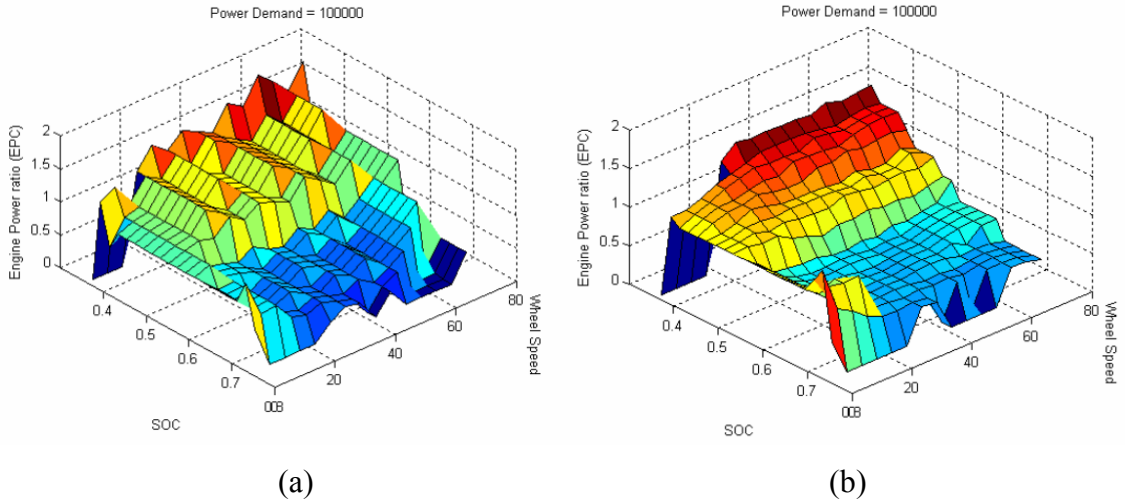


Figure D.5: Comparison of control maps between (a) the initial control design and (b) the refined control design (right).

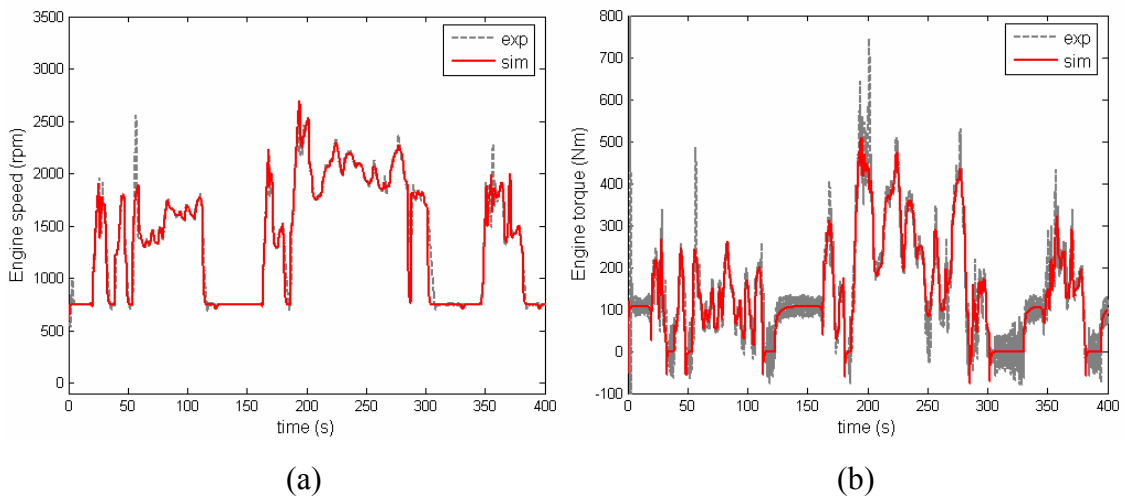


Figure D.6: Comparison of (a) engine speed and (b) engine torque results between simulation and experiment with a more accurate and smoother control design.

As the engine performance in the test cell differs with the two controllers, so do the fuel economy and emissions. As indicated in the description of our experimental methodology, fast particulate size and mass analyzer enables insight into transient emissions. Figure D.7 shows the soot concentration in the exhaust during a representative interval in a driving cycle. Sharp spikes and subsequent periods of prolonged elevated levels of soot are often above the visibility limit of 75 mg/m³. The visibility limit is

estimated by converting the typical Bosch smoke number of 2 to particulate mass using an empirical formula (Hagena et al. 2006). When integrated over the whole cycle the transient increases translate into large total emission of soot, larger than what was obtained for the conventional (non-hybrid) vehicle configuration (Figure D.8). Therefore, the EIL capability proved to be critical in uncovering the emission challenge of the strategy optimized solely based on the simulation runs and a fuel economy target. The refined SDP leads to much more moderate transients and keeps the soot concentration below the visibility limit throughout the cycle. The final assessment is enabled with the cumulative results given in Figure D.8, summarizing the fuel economy and soot emission of a conventional baseline vehicle and versions of the HEV platform with the initial SDP and the refined SDP. Although the fuel economy improves with either SDP controller, the frequent rapid transients with the initial SDP come with a price, and fuel economy is improved further with the refined strategy, up to 26%. Smoother engine operation with the SDP eliminates the soot emission penalty seen with the original control strategy, and reduces the total below the values obtained for the conventional vehicle. In summary, using the SDP methodology for controller design and the EIL capability for validation and refinement unlocks the full potential of the HEV concept as a fuel efficient and clean propulsion option. Note the numbers do not necessarily represent the ultimate potential of this configuration, and further improvement might be possible with downsizing of the engine.

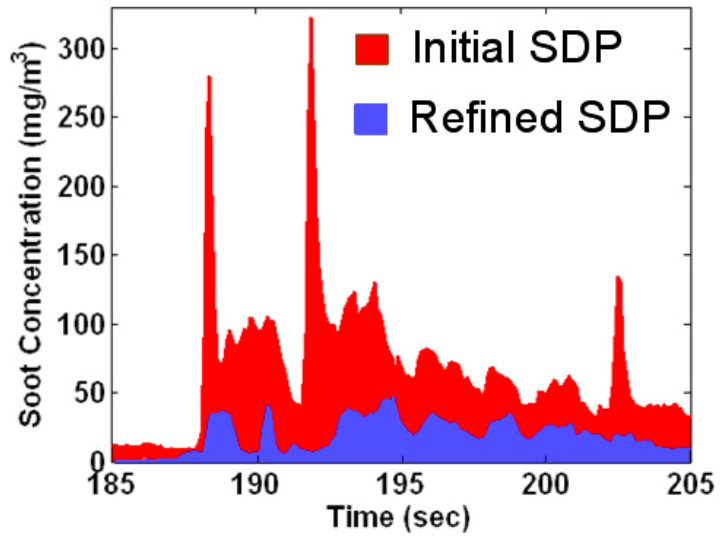


Figure D.7: Comparison of transient soot concentration profiles during a 185s-205 sec interval of the FTP75 driving schedule. Refined SDP power management strategy (light blue) eliminates the transient spikes of soot emission seen with the initial strategy (dark red).

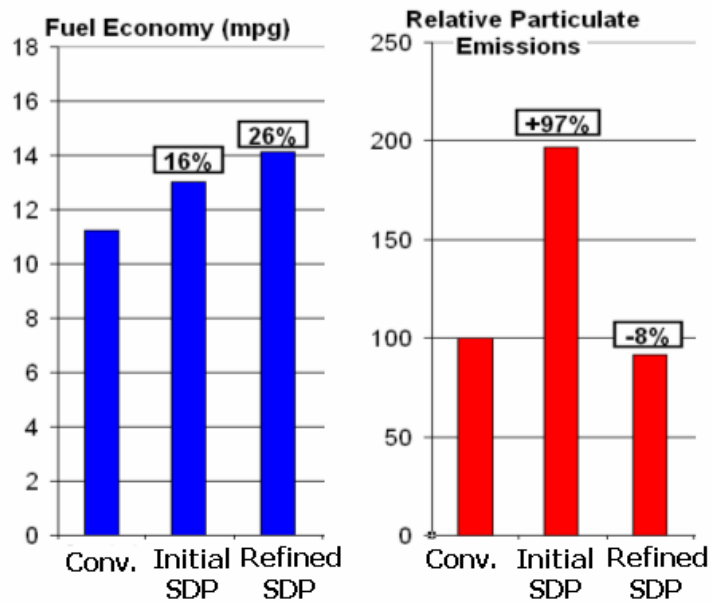


Figure D.8: Final fuel economy and soot emission comparison between the conventional vehicle and different control designs.

BIBLIOGRAPHY

BIBLIOGRAPHY

- Abe, S., Sasaki, S., Matsui, H., Kubo, K., (1997), "Development of Hybrid System for Mass Productive Passenger Car," *JSAE Proc.* 9739543, pp. 21-24.
- Achtenova, G. and Svoboda, J., (2003), "Computer-Aided Calculation of Planetary Gear Sets," *SAE Paper*, 2003-01-0129.
- Ai, X. and Mohr, T., (2004), "An Electro-Mechanical Infinitely Variable Speed Transmission," *SAE Paper* 2004-01-0354.
- Ai, X. and Anderson, S., (2005), "An Electro-Mechanical Infinitely Variable Transmission Hybrid Electric Vehicles," *SAE Paper* 2005-01-0281.
- Assanis, D., Filipi, Z., Gravante, S., Grohnke, D., Gui, X., Louca, L. S., Rideout, G. D., Stein, J., Wang, Y., (2000), "Validation and Use of SIMULINK Integrated, High Fidelity, Engine-in-Vehicle Simulation of the International Class VI Truck," *SAE Paper*, 2000-01-0288.
- Beachley, N. H., Frank, A. A., (1980), "Control Considerations for a Flywheel Hybrid Automobile with a Mechanical Continuously Variable Transmission," *1980 Technology Symposium*, co-sponsored by DOE, ASME and LLNL, Scottsdale, AZ, October, 1980.
- Bellman, R.E., (1957) *Dynamic Programming*, Princeton University Press, New Jersey.
- Bellman, R.E. and Kalaba, R., (1965), *Dynamic Programming and Modern Control Theory*, Academic Press, New York, 112pp.
- Benford, H., Leising, M., (1981), "The Lever Analogy: a New Tool in Transmission Analysis," *SAE Paper* 810102.
- Bertsekas, D.P., (1976), *Dynamic Programming and Stochastic Control*, Academic Press, New York.
- Bertsekas, D.P., (1995), *Dynamic Programming and Optimal Control*, Athena Scientific.
- Besel, G., Hou, E., (1980), "Flywheel Energy Accumulators for City Buses – Steel and Composite Design," *1980 Technology Symposium*, co-sponsored by DOE, ASME and LLNL, Scottsdale, AZ, October, 1980.
- Brahma, A., Guezennec, Y., and Rizzoni, G., (2000), "Optimal Energy Management in Series Hybrid Electric Vehicles," *Proceedings of the American Control Conference*, Chicago, Illinois, Jun. 2000

- Castillo, J. M., (2002), "The Analytical Expression of the Efficiency of Planetary Gear Trains," *Mech. Mach. Theory*, Vol. 37, pp. 197–214.
- Conlon, B., (2005), "Comparative Analysis of Single and Combined Hybrid Electrically Variable Transmission Operating Modes," *SAE Paper* 2005-01-1162.
- Cooper, L. and Cooper, M.W., (1981), *Introduction to Dynamic Programming*, Pergamon Press.
- Cornell, E. P., Turnbull, E. P., Barlow, T. M., (1980), "Evaluation of a Hybrid Flywheel-Battery Propulsion System for Electric Vehicles," *1980 Technology Symposium*, co-sponsored by DOE, ASME and LLNL, Scottsdale, AZ, October, 1980.
- Cuenca, R.M., Gaines, L.L., and Vyas, A.D., (1999), "Evaluation of Electric Vehicle Production and Operating Costs," Argonne National Laboratory.
- Delprat, S., Guerra, T.M., Paganelli, G., Lauber, J., and Delhom, M., (2001), "Control Strategies Optimization for an Hybrid Parallel Powertrain," *Proc. of America Control Conference*, Arlington, VA.
- Delprat, S., Lauber, J., Guerra, T.M., Rimaux, J., (2004), "Control of a Parallel Hybrid Powertrain: Optimal Control," *IEEE Transactions on Vehicular Technology Conference*, Vol. 53, No. 3, pp. 872-881.
- Department of Energy, (2007), "World Crude Oil Price," Accessed at http://tonto.eia.doe.gov/dnav/pet/pet_pri_wco_k_w.htm, Jan. 31, 2007.
- DieselNet, (2007), "Emission Standards," Accessed at <http://www.dieselnet.com/standards/us/light.html>. Jan. 31, 2007.
- Duoba, M., Ng, H., and Larsen, R., (2000), "In-Situ Mapping and Analysis of the Toyota Prius HEV Engine," *SAE Paper* 2000-01-3096.
- Duoba, M., Ng, H., and Larsen, R., (2001), "Characterization and Comparison of Two Hybrid Electric Vehicles (HEVs) – Honda Insight and Toyota Prius," *SAE Paper* 2001-01-1335.
- Energy and Environmental Analysis, Inc., (2005), *Automotive Technology Cost and Benefit Estimates*, Arlington, Virginia, March.
- Energy Information Administration, (1996), *Annual Energy Review*, Report DOE/EIA-0384.
- Energy Information Administration, (2002), *Emissions of Greenhouse Gases in the United States 2002*, Report DOE/EIA-0573.

- Environmental Protection Agency, (2007), "Mobile Source Emissions Milestones," Accessed at <http://www.epa.gov/otaq/invtory/overview/solutions/milestones.htm>, Jan. 31, 2007.
- Evans, D. G., Polom, M. E., Poulos, S. G., Maanen, K., Zarger, T. H., (2003), "Powertrain Architecture and Controls Integration for GM's Hybrid Full-Size Pickup Truck," *SAE Paper* 2003-01-0085.
- Farrall, S. D. and Jones, R. P., (1993), "Energy Management in an Automotive Electric/Heat Engine Hybrid Powertrain Using Fuzzy Decision Making," *Proceedings of the 1993 International Symposium on Intelligent Control*, Chicago, IL.
- Filipi, Z., Loucas, L., Daran, B., Lin, C-C., Yildir, U., Wu, B., Kokkolaras, M., Assanis, D., Peng, H., Papalambros, P., Stein, J., Szkubiel, D., Chapp, R., (2004), "Combined Optimization of Design and Power Management of the Hydraulic Hybrid Propulsion System for the 6x6 Medium Truck", *International Journal of Heavy Vehicle Systems*, Vol. 11, Nos. 3/4, 2004, pp. 371-401
- Filipi, Z., Fathy, H., Hagen, J., Knafl, A., Ahlawat, R., Liu, J., Jung, D., Assanis, D., Peng, H., Stein, J., (2006) "Engine-in-the-Loop Testing for Evaluating Hybrid Propulsion Concepts and Transient Emissions - HMMWV Case Study," *SAE Paper*, 2006-01-0443; *SAE Transactions, Journal of Commercial Vehicles*, 2006.
- Freudenstein, F. and Yang, A. T., (1972), "Kinematics and Statics of a Coupled Epicyclic Spur-Gear Train," *Mechanism and Machine Theory*, Vol. 7, pp. 263-275.
- Fueleconomy.gov, (2007), "More Hybrids Coming Soon," Accessed at http://www.fueleconomy.gov/feg/hybrid_news.shtml, Jan. 31, 2007.
- Gelb, G. H., Richardson, N.A., Wang, T. C., Berman, B., (1971), "An Electromechanical Transmission for Hybrid Vehicle Power Trains – Design and Dynamometer Testing," *SAE Paper* 710235.
- Gluss, B., (1972), *An Elementary Introduction to Dynamic Programming: A State Equation Approach*, Allyn and Bacon, INC.
- Grewe, T.M., Conlon, B.M., Holmes, A.G., (2007), "Defining the General Motors 2-Mode Hybrid Transmission," *SAE Paper* 2007-01-0273.
- Guezennec, Y., Choi, T., Paganelli, G., Rizzoni, G., (2003), "Supervisory Control of Fuel Cell Vehicles and its Link to Overall System Efficiency and Low-Level Control Requirements," *American Control Conference*, Vol. 3, pp. 2055-2061.
- Guzzella, L. and Amstutz, A., (1999), "CAE Tools for Quasi-Static Modeling and Optimization of Hybrid Powertrains," *IEEE Transaction on Vehicular Technology*, Vol. 48, No. 6, pp. 1762-1769.

- Haapala, K., Thul, A., Andrasko, S., Muehlfield, C., Bloss, B., Nesbitt, R., and Beard, J. E., (2002), "Design and Development of the 2001 Michigan Tech FutureTruck, a Power-Split Hybrid Electric Vehicle," *SAE Paper* 2002-01-1212.
- Hagena, J.R., Filipi, Z.S., Assanis, D.N., (2006), "Transient Diesel Emissions: Analysis of Engine Operation During a Tip-In", *SAE Paper* 2006-01-1151.
- Harada, O., Yamaguchi, K., Shibata, Y., (2000), "Power output apparatus and method of controlling the same," *US Patent* 6,067,801, issued May. 30, 2000.
- Harmon, K. B., (1998), "The History of Allison Automatic Transmissions For On-Highway Trucks and Buses," *SAE Paper* 982791.
- Hermance, D., (1999), "Toyota Hybrid System," *1999 SAE TOPTec Conference*, Albany, NY, May 1999.
- Hermance, D. and Abe, S., (2006), "Hybrid Vehicles Lessons Learned and Future Prospects," *SAE Paper* 2006-21-0027.
- Holmes, A. G. and Schmidt, M. R., (2002), "Hybrid Electric Powertrain Including a Two-Mode Electrically Variable Transmission" *U.S. Patent* 6,478,705 B1, issued Nov. 12, 2002.
- Holmes, A. G., Klemen, D., Schmidt, M. R., (2003), "Electrically Variable Transmission with Selective Input Split, Compound Split, Neutral and Reverse Modes," *US Patent* 6,527,658 B2, issued Mar. 4, 2003.
- Howard, R. A. (1960), *Dynamic programming and Markov process*, MIT Press, Cambridge, Mass.
- Hsieh, H. I. and Tsai, L.W., (1996), "Kinematic Analysis of Epicyclic-Type Transmission Mechanisms Using the Concept of Fundamental Kinematic Entities," *ASME J. Mech. Des.*, 118, pp. 294–299.
- Hsieh, H. I. and Tsai, L.W., (1998), "The Selection of a Most Efficient Clutching Sequence Associated With Automatic Transmission Mechanisms," *ASME J. Mech. Des.*, 120, pp. 514–519.
- Jalil, N., Kheir, N. A., and Salman, M., (1997), "A Rule-Based Energy Management Strategy for a Series Hybrid Vehicle," *Proceedings of the American Control Conference*, Albuquerque, New Mexico, Jun. 1997.
- Jeon, S. I., Jo, S. T., Park, Y. I., Lee, J. M., (2002), "Multi-Mode Driving Control of a Parallel Hybrid Electric Vehicle Using Driving Pattern Recognition," *ASME Journal of Dynamic Systems, Measurement, and Control*, Vol. 124, No. 1, pp. 141-149.

- Kaharaman, A., Ligata, H., Kienzle, K., Zini, D.M., (2004), "A Kinematics and Power Flow Analysis Methodology for Automatic Transmission Planetary Gear Trains," *Journal of Mechanical Design*, Vol. 126, Issue 6, pp. 1071-1081.
- Kamichi, K., Okasaka, K., Tomatsuri, M., Matsubara, T., Kaya, Y., Asada, H., (2006), "Hybrid System Development for a High-Performance Rear Drive Vehicle," *SAE Paper 2006-01-1338*.
- Kawahashi, A., (2004), "A New-Generation Hybrid Electric Vehicle and Its Implications on Power Electronics," *CPES2004, Power Electronics Seminar & Industry Review*, VPI, Blacksburg, VA, 18-20 April 2004.
- Kim, C., NamGoong, E., and Lee, S., (1999), "Fuel Economy Optimization for Parallel Hybrid Vehicles with CVT," *SAE Paper 1999-01-1148*.
- Kim D., (2006), "Math-Model Based Gear-Shift Control Strategy for Advanced Vehicle Powertrain Systems," *Dissertation*, University of Michigan.
- Kim, M. and Peng, H., (2006), "Combined Control/Plant Optimization of Fuel Cell Hybrid Vehicles," *Proc. of the American Control Conference*, Minneapolis, MN.
- Kim, M., (2007), "Modeling, Control, and Design Optimization of a Fuel Cell Hybrid Vehicle," *Dissertation*, University of Michigan.
- Kimura, A., Abe, T., Sasaki, S., (1999), "Drive force control of a parallel-series hybrid system," *JSAE Review* Vol. 20, pp. 337-341.
- Kimura, A., Ando, I., Itagaki, K., (2005), "Development of Hybrid System for SUV," *SAE Paper 2005-01-0273*.
- Kirk, D.E., (1970), *Optimal Control Theory: An Introduction*, Prentice-Hall.
- Klages, B., Woermann, R.J., and Theuerkauf, H. J., (1997), "An Improved Real-Time Model of a Planetary Gear Train," *SAE Paper 970970*.
- Koide, T., Matsui, H., Nada, M., (1999), "Hybrid Vehicle Drive System Having Two Motor/Generator Units and Engine Starting Means," *US Patent 5,934,395*, Issued Aug. 1999.
- Kolmanovsky, I., Siverguina, I., and Lygoe, B., (2002), "Optimization of Powertrain Operation Policy for Feasibility Assessment and Calibration: Stochastic Dynamic Programming Approach," *American Control Conference*, Anchorage, Alaska.
- Lee, H.D. and Sul, S.K., (1998), "Fuzzy-Logic-Based Torque Control Strategy for Parallel-Type Hybrid Electric Vehicle," *IEEE Transactions on Industrial Electronics*, Vol. 45, No. 4, pp. 625-632.
- Lewis, F.L. and Syrmos, V.L., (1995), *Optimal Control*, New York: Wiley.

- Lin, C., Filipi, Z., Wang, Y., Louca, L., Peng, H., Assanis, D., Stein, J., (2001), "Integrated, Feed-forward Hybrid Electric Vehicle Simulation in SIMULINK and its Use for Power Management Studies," *SAE Paper*, 2001-01-1334.
- Lin, C., Peng, H., Grizzle, J. W., Liu, J., and Busdiecker, M., (2003a), "Control System Development for an Advanced-Technology Medium-Duty Hybrid Electric Truck," *SAE Paper* 2003-01-3369.
- Lin, C., Peng, H., Grizzle, J. W., Kang, J., (2003b), "Power Management Strategy for a Parallel Hybrid Electric Truck," *IEEE Transactions on Control Systems Technology*, vol. 11, pp. 839-849.
- Lin, C., Peng, H., Grizzle, J. W., (2004a), "A Stochastic Control Strategy for Hybrid Electric Vehicles," *Proceeding of the American Control Conference*, Boston, Massachusetts.
- Lin, C., (2004b), "Modeling and Control Strategy Development for Hybrid Vehicles," *Dissertation*, University of Michigan.
- Liu, J., Peng, H., Filipi, Z., (2005), "Modeling and Control Analysis of Toyota Hybrid System," *International Conference on Advanced Intelligent Mechatronics*, Monterey, CA. Jul. 24-28, 2005.
- Liu, J., Peng, H., (2006), "Control Optimization for a Power-Split Hybrid Vehicle", *Proceeding of the American Control Conference*, Minnesota, MN.
- Liu, J., Hagen, J., Peng, H., Filipi, Z., (2007), "Engine-in-the-Loop Study of the Stochastic Dynamic Programming Control for a Hybrid Electric HMMWV", *Int. Journal of Heavy Vehicle Systems*, Accepted in 2007.
- Livezey, W. G., (1969), "Input-Split-Power, Output-Split-Power, Compound-Split-Power, Power Train," *US Patent* 3,470,769, issued Nov. 1969.
- Markel, T., Brooker, A., Hendricks, T., Johnson, V., Kelly, K., Kramer, B., O'keefe, M., Sprik, S., and Wipke, K., (2002), "ADVISOR: a Systems Analysis Tool for Advanced Vehicle Modeling," *Journal of Power Source*, Vol. 110, pp. 255-266.
- McCausland, I., (1969), *Introduction to Optimal Control*, Wiley.
- Mianzo, L., Peng, H., (2000), "Modeling and control of a variable valve timing engine," *American Control Conference*, Vol. 1, No. 6, pp. 554-558.
- Michelena, N., Louca, L., Kokkolaras, M., Lin, C., Jugn, D., Filipi, Z., Assanis, D., Papalambros, P., Peng, H., Stein, J., Feury, M., (2001), "Design of an Advanced Heavy Tratical Truck: A Target Cascading Case Strudy," *SAE Paper* 2001-01-2793.

- Miller, J. M. and Everett, M. (2005), "An assessment of ultra-capacitors as the power cache in Toyota THS-II, GM-Allision AHS-2 and Ford FHS hybrid propulsion systems," *Applied Power Electronics Conference and Exposition*, Vol. 1, pp. 481 - 490.
- Miller, J. M., (2006), "Hybrid Electric Vehicle Propulsion System Architectures of the e-CVT Type," *IEEE Transactions on Power Electronics*, Vol. 21, No. 3, pp 756-767.
- Musardo, C., Rizzoni, G., and Staccia, B., (2005), "A-ECMS: An Adaptive Algorithm for Hybrid Electric Vehicle Energy Management," *Proc. of IEEE Conference on Decision and Control*, Seville, Spain.
- Muta, K., Yamazaki, M., and Tokieda, J., (2004), "Development of New-Generation Hybrid System THS II – Drastic Improvement of Power Performance and Fuel Economy," *SAE Paper 2004-01-0064*.
- Nagasaka, A., Nada, M., Hamada, H., Hiramatsu, S., Kikuchi, Y., (1998), "Development of the Hybrid/Battery ECU for the Toyota Hybrid System," *SAE Paper 981122*.
- National Highway Traffic Safety Administration, (2007), "Light Truck Fleet Average Characteristics," Accessed at <http://www.nhtsa.gov/cars/rules/CAFE/LightTruckFleet.htm>, Jan. 31, 2007.
- National Renewable Energy Laboratory, (2005), "Advanced Vehicle Simulator (ADVISOR) ," <http://www.ctts.nrel.gov/analysis/advisor.html>, 2005.
- Nedungadi, A., Dardalis, D., (1999), "A Parallel Hybrid Drivetrain," *SAE Paper 1999-01-2928*.
- Ng, H., Anderson, J., Duoba, M., and Larsen, R., (2001), "Engine Start Characteristics of Two Hybrid Electric Vehicles (HEVs) – Honda Insight and Toyota Prius," *SAE Paper 2001-01-2492*.
- Ogawa, H., Matsuki, M., and Eguchi, T., (2003), "Development of a Power Train for the Hybrid Automobile – The Civic Hybrid," *SAE Paper 2003-01-0083*.
- Paganelli, G. Guerra, T.M., Delprat, S. Santin, J.J., Delhom, M., Combes, E., (2000), "Simulation and Assessment of Power Control Strategies for a Parallel Hybrid Car," *J. Automobile Engineering, also in Proc. Of the Institution of Mechanical Engineers IMechE, SAE International*, 214, pp. 705-718.
- Paganelli, G., Ercole, G., Brahma, A., Guezennec, Y., Rizzoni, G., (2001), "General Supervisory Control Policy for the Energy Optimization of Charge-Sustaining Hybrid Electric Vehicles," *JSAE Review*, Vol. 22, No. 4, pp. 511-518.

- Paganelli, G., Tateno, M., Brahma, A., Rizzoni, G., and Guezenec, Y., (2001), "Control Development for a Hybrid-Electric Sport-Utility Vehicle: Strategy, Implementation and Field Test Results," *Proceedings of the American Control Conference*, Arlington, VA.
- Paganelli, G., Delprat, S., Guerra, T.M., Rimaux, J., Santin, J.J., (2002), "Equivalent Consumption Minimization Strategy for Parallel Hybrid Powertrains," *Vehicular Technology Conference*, Vol. 4, pp. 2076-2081.
- Paganelli, G., Guezenec, Y., Rizzoni, G., (2002), "Optimizing Control Strategy for Hybrid Fuel Cell Vehicle," *SAE Paper 2002-01-0102*.
- Paschen, J. M., Johnson, C., (2003), "Shared Technology/Shared Cost, the Evaluation of the Allison EP-50 Electric Drive for Military and Commercial Vehicles," *SAE Paper 2003-01-0271*.
- Pennestri, E., and Freudenstein, F., (1993a), "A Systematic Approach to Power Flow and Static-Force Analysis in Epicyclic Spur-Gear Trains," *ASME J. Mech. Des.*, 115, pp. 639–644.
- Pennestri, E., and Freudenstein, F., (1993b), "The Mechanical Efficiency of Epicyclic Gear Trains," *ASME J. Mech. Des.*, 115, pp. 645–651.
- Piccolo, A., Ippolito, L., Galdi, V., Vaccaro, A., (2001), "Optimization of Energy Flow Management in Hybrid Electric Vehicles via Genetic Algorithms," *Proc. of 2001 IEEE/ASME International Conference on Advanced Intelligent Mechatronics*, Como, Italy.
- Pisu, P., Rizzoni, G., Musardo, C., and Staccia, B., (2004), "A Comparative Study of Supervisory Control Strategies for Hybrid Electric Vehicles," *Proc. of International Mechanical Engineering Congress and Exposition*, Anaheim, CA.
- Raghavan, M., Bucknor, N.K., Hendrickson, J.D., (2007), "Electrically Variable Transmission Having Three Interconnected Planetary Gear Sets, Two Clutches and Two brakes," *US Patent 7,179,187 B2*, Issued Feb. 2007.
- Rahman, Z., Butler, K., and Ehsani, M., (2000), "A Comparison Study Between Two Parallel hybrid Control Concepts," *SAE Paper 2000-01-0994*.
- Ravigneaux, P., (1953), "Epicyclic Change-Speed Gear," *US Patent 2,631,476*, Issued Mar. 1953.
- Reilly, D. J., Andersen, R. P., Casparian, R. J., and Dugdale, P. H., (1991), "Saturn DOHC and SOHC Four Cylinder Engines," *SAE paper 910676*.
- Rizoulis, D., Burl, J., and Beard, J., (2001), "Control Strategies for a Series-Parallel Hybrid Electric Vehicle," *SAE Paper 2001-01-1354*.

- Rizzoni, G., Guzzella, L., Baumann, B., (1999), "Unified Modeling of Hybrid Electric Vehicle Drivetrains," *IEEE/ASME Transactions on Mechatronics*, Vol. 4, No. 3, pp. 246-257.
- Roos, F., and Spiegelberg, C., (2004), "Relations between size and gear ratio in spur and planetary gear trains," Technical Report, Department of Machine Design, Royal Institute of Technology, KTH.
- Ross, S. M., (1983), *Introduction to Stochastic Dynamic Programming: Probability and Mathematical*, Academic Press, Inc.
- Rousseau, A., Pagerit, S., Monnet, G., Feng, A., (2001a), "The New PNGV System Analysis Toolkit PSAT V4.1 – Evolution and Improvement," *SAE Paper 2001-01-2536*.
- Rousseau, A., Sharer, P., and Pasquier, M., (2001b), "Validation Process of a HEV System Analysis Model: PSAT," *SAE Paper 2001-01-0953*.
- Sasaki, S., (1998), "Toyota's Newly Developed Hybrid Powertrain," *Proceedings of the 1998 IEEE 10th International Symposium on Power Semiconductor Devices & IC's*, Kyoto, Japan, 3-6 June, 1998.
- Sciarretta, A., Back, M., and Guzzella, L., (2004), "Optimal Control of Parallel Hybrid Electric Vehicles," *IEEE Transactions on Control System Technology*, Vol. 12, No. 3, pp. 352-363.
- Schmidt, M. R., (1996a), "Two-Mode, Compound-Split Electro-Mechanical Vehicular Transmission," *US Patent 5,558,589*, Issued Sep. 1996.
- Schmidt, M. R., (1996b), "Two-Mode, Split Power, Electro-Mechanical Transmission," *US Patent 5,577,973*, Issued Nov. 1996.
- Schmidt, M. R., (1996c), "Two-Mode, Input-Split, Parallel, Hybrid Transmission," *US Patent 5,558,588*, Issued Sep. 1996.
- Schmidt, M. R., (1999), "Two-Mode, Compound-Split Power, Electro-Mechanical Vehicular Transmission," *US Patent 5,931,757*, Issued Aug. 1999.
- Schmidt, M. R., Klemen, D., Holmes, A. G., (2006), "Two-Mode Compound-Split Electrically Variable Transmission," *US Patent 7,022,038*, Issued Apr. 2006.
- Schouten, N., Salman, M., Kheir, N., (2002), "Fuzzy Logic Control for Parallel Hybrid Vehicles," *IEEE Transactions on Control Systems Technology*, Vol. 10, No. 3, pp. 460-468.
- Schweitzer, P. and Seidmann, A., (1985), "Generalized Polynomial Approximations in Markovian Decision Processes," *Journal of Mathematical Analysis and Applications*, 110:568–582, 1985.

- Setlur, P., Wagner, J. R., Dawson, D. M., and Samuels, B., (2003), "Nonlinear Control of a Continuously Variable Transmission (CVT)," *IEEE Transactions on Control Systems Technology*, Vol. 11, No. 1, pp. 101-108.
- Tatano, H., Okada, N., and Kawai, H., (1992), "Optimal Operation Model of a Single Reservoir with Drought Duration Explicitly Concerned," *Journal Stochastic Environmental Research and Risk Assessment*, Vol. 6, No. 2, pp. 123-134.
- Tate, E., Grizzle, J.W., and Peng, H., (2006), "Shortest Path Stochastic Control for Hybrid Electric Vehicles," *PhD dissertation*, University of Michigan, Ann Arbor, MI.
- Toyota Motor Corporation (2007), "Toyota Hybrid System Technology," Accessed at <http://www.toyota.co.jp/en/tech/environment/ths2/index.html> on Jan. 31, 2007.
- Transportation Energy Data Book: Edition 25, (2006), Oak Ridge National Laboratory, http://cta.ornl.gov/cta/publications_search_results.cfm.
- Wang W., (2002), "Revisions on the Model of Toyota Prius in ADVISOR 3.1," *SAE Paper 2002-01-0993*.
- Waltermann, P., (1996), "Modeling and Control of the Longitudinal and Lateral Dynamics of a Series Hybrid Vehicle," *Proceedings of the 1996 IEEE International Conference on Control Applications*, Dearborn, MI. Sep. 15-18, 1996.
- Wipke, K., Cuddy, M., Burch, S., (1999), "ADVISOR 2.1: a User-friendly advanced Powertrain Simulation Using a Combined Backward/Forward Approach," *IEEE Transaction on Vehicular Technology*, Vol. 48, No. 6, pp. 1751-1761.
- Wipke, K., Markel, T., Nelson, D., (2001), "Optimizing Energy Management Strategy and Degree of Hybridization for a Hydrogen Fuel Cell SUV," *Proceedings of 18th International Electric Vehicle Symposium (EVS 18)*, Berlin.
- Wohl, R., Long, T., Mucino, V., Smith, J. E., (1993), "A Model for a Planetary-CVT Mechanism: Analysis and Synthesis," *Society of Automotive Engineers*, Paper No. 93065, SAE Congress and Exposition, Detroit, MI., March 1-5, 1993.
- Won, J. S., Langari, R., and Ehsani, M., (2005), "An Energy Management and Charge Sustraining Strategy for a Parallel Hybrid Vehicle With CVT," *IEEE Transactions on Control System Technology*, Vol. 13, No. 2, pp. 313-320.
- Wu, B., Lin, C.C., Filipi, Z., Peng H., Assanis, D., (2004), "Optimal Power Management for a Hydraulic Hybrid Delivery Truck", *Journal of Vehicle System Dynamics*, Vol. 42, Nos. 1-2, pp. 23-40.

Zhang, D., Chen, J., Tsieh, T., Rancourt, J., Schmidt, M.R., (2001), "Dynamic Modeling and Simulation of Two-Mode Electric Variable Transmission," *Proc. of IMechE*, Vol 215, pp. 1217-1223.

Zhang, H., Zhu, Y., Tian, G., Chen, Q., and Chen, Y., (2004), "Optimal Energy Management Strategy for Hybrid Electric Vehicles," *SAE Paper* 2004-01-0576.